Electronic Supplementary Material (ESI) for Dalton Transactions.

Supplementary Information

Access to metastable $[GeH_2]_n$ materials via a molecular "bottom-up" approach

Jocelyn Sinclair,[a] William Medroa del Pino,[a] Kwami Aku-Dominguez,[a] Yohei Minami,[b] Anagha Kiran,[a] Michael J. Ferguson,[a] Makoto Yasuda[b] and Eric Rivard*,[a]

[a] Department of Chemistry, University of Alberta, 11227 Saskatchewan Dr., Edmonton, Alberta, Canada T6G 2G2. E-mail: erivard@ualberta.ca

[b] Department of Applied Chemistry, Osaka University, 2-1 Yamadaoka, Suita, Osaka 565-0971, Japan.

Table of Contents

1. Experimental Procedures

General

All reactions were performed using standard Schlenk techniques under an atmosphere of nitrogen or in a nitrogen-filled glove box (Innovative Technology, Inc.). Solvents were dried using a Grubbs-type solvent purification system manufactured by Innovative Technology, Inc., and stored under an atmosphere of nitrogen prior to use. Cl_2Ge•dioxane, methyl iodide, potassium *tert*-butoxide, *tert*-butanol, catecholborane (HBcat), Me_2•SMe_2, diisobutylaluminum hydride (DIBAL-H), 2,3-dimethyl-1,3-butadiene and 1-methylimidazole were purchased from Sigma-Aldrich and used as received. 4,4,5,5-Tetramethyl-1,2-dioxaborolane (HBpin) was purchased from Oakwood Chemicals and used as received. 4-Dimethylaminobenzaldehyde was purchased from BDH Chemicals and recrystallized from absolute ethanol prior to use. 4,4′-Difluorobiphenyl was obtained from K&K Laboratories and recrystallized from toluene before use. $ImMe_2$•$GeCl_2$ ($ImMe_2$ = $(HCNMe)_2C$:),[S1] $Ge(OMes^*)_2$ (Mes* = 2,4,6-$^tBu_3C_6H_2$),[S2] and 1,2-$^iPr_2P(C_6H_4)BCy_2$ (Cy = cyclohexyl), **PB**,[S3] were prepared according to literature procedures. ^1H, $^{11}B/^{11}B\{^1H\}$, $^{13}C\{^1H\}$, and $^{19}F\{^1H\}$ NMR spectra were recorded on a Varian Inova 400 or 500 MHz spectrometer and referenced externally to Me_4Si (^1H, $^{13}C\{^1H\}$), F_3B•OEt_2 ($^{11}B/^{11}B\{^1H\}$) and $CFCl_3$ ($^{19}F\{^1H\}$). Crystals of appropriate quality for single crystal X-ray diffraction studies were removed from the mother liquor and immediately covered with a thin layer of hydrocarbon oil (Paratone-N) in a sealed vial for transport to the instrument. A suitable crystal was then selected, attached to a glass fiber, and mounted under a stream of nitrogen onto the instrument. All data were collected using a Bruker APEX II CCD detector/D8 diffractometer using Cu Kα radiation. The data were corrected for absorption through Gaussian integration from indexing of the crystal faces. Structures were solved and refinements were completed using direct methods (SHELXT-2014 and SHELXL-2018/3).[S4] Elemental analyses were performed by the Analytical and Instrumentation Laboratory at the University of Alberta. Melting points were obtained in sealed glass capillaries under nitrogen using a MelTemp melting point apparatus and are uncorrected.

Diffusion-ordered spectroscopy (DOSY) experiments

Diffusion-ordered spectroscopy (DOSY) experiments were performed on a 600 MHz Varian/Agilent instrument equipped with a Z-gradient HCN indirect detection probe capable of outputting 72 G/cm of gradient strength. All measurements were carried out non-spinning and at a calibrated temperature of 27.0 °C using the Oneshot45 pulse sequence.[S5,S6] For all DOSY experiments, a spectral window of 7.2 kHz was used with a 3 s acquisition time and a 3 s relaxation delay with 4 scans for each gradient increment. Pulse widths and gradient strengths were optimized for each sample. A diffusion delay of 50 ms was used. Fifteen gradient strengths from 2 to 59.5 G/cm were used for the benzene solutions. The spectra were Fourier transformed and baseline corrected prior to discrete processing. Data were fit to a double exponential decay and corrected for non-uniform pulsed field gradients.[S7] The diffusion dimension was zero filled to 1024 data points and the directly detected dimension was zero filled to 256K data points prior to final DOSY processing. All data were acquired and processed using OpenVNMRJ 2.1A.

Characterization of solid materials

Diffuse reflectance analysis was performed employing a Cary 5000 UV-Vis-NIR spectrophotometer equipped with a DRA-CA-50M diffuse reflectance accessory, a double out-of-plane Littrow monochromator, and a R928 PMT detector. Glass plates were sealed with candelilla

wax, a low melting point and low oxygen permeability wax, purchased from amazon.ca (Supplier: "Health & Beauty").

Powder XRD patterns were collected on a Rigaku Ultima IV powder diffractometer equipped with a Co Kα radiation source ($K_{\alpha1}$ = 1.78900 Å, $K_{\alpha2}$ = 1.79283 Å) operating at 40 kV and 40 mA. A D/Tex Ultra detector was used, with an iron filter to eliminate the K_β radiation at 1.62083 Å. Samples were placed on zero-background holders. Diffraction data were collected in continuous scan mode between 5 and 90° in 2θ with a step size of 0.0200°.

Scanning electron microscopy (SEM) images were obtained using a Zeiss Sigma 300 VP-FESEM instrument equipped with a secondary electron detector and a Bruker energy-dispersive X-ray (EDX) spectroscopy system operating at 5 or 10 kV. Samples were mounted on aluminum stubs with carbon tape.

Raman spectroscopy was performed using a Renishaw's inVia Raman Spectrometer (632 nm or 785 nm, 0.6 mW, 3 × 10 s collection).

Mass spectrometry (EI-MS) was performed by the Mass Spectrometry Facility at the University of Alberta.

X-ray photoelectron spectroscopy (XPS) was conducted on a PHI VersaProbe III at the nanoFAB facility at the University of Alberta operating in energy spectrum mode at 23.17 W. Samples were mounted to the sample holder with double sided tape and transferred into a portable inert atmosphere antechamber for delivery from the N_2 glovebox into the XPS instrument. The base and operating chamber pressure were maintained at 10^{-7} Pa. A monochromatic Al Kα source (1486.6 eV) was used to irradiate the samples, and the spectra were obtained with an electron take-off angle of 45°. Survey spectra were collected using an elliptical spot with major and minor axis lengths of 2 and 1 mm, respectively, and 280 eV pass energy with a step of 0.1 eV. CasaXPS software (VAMAS) was used to interpret high-resolution spectra. All spectra were internally calibrated to the C 1s emission (284.8 eV).

A flame test was used to determine a threshold for detectible boron content by eye (burns green). Stock solids were created by the grinding of silica gel (no color by flame test) with boric acid, with known boron mass contents. The solids were burned on a spatula in a propane flame, and the results filmed to check for detectible green in the flame. The lowest threshold for detectable green in the flame was at 0.085 mass % boron. Please see the Supplementary Powerpoint file for videos of some standards and the sample **2c**.

Compound synthesis and reactivity studies

K[Ge(O^{t}Bu)$_3$]: To Cl_2Ge•dioxane (0.510 g, 2.20 mmol) in 20 mL of THF was added K[O^{t}Bu] (0.785 g, 7.00 mmol). The reaction mixture was stirred at room temperature for 2 hrs and then the mixture was filtered. Removal of the volatiles from the filtrate *in vacuo* afforded K[Ge(O^{t}Bu)$_3$] (0.692 g, 95 %) as a white solid. Crystals of suitable quality for single crystal X-ray diffraction were obtained by cooling a saturated toluene solution of K[Ge(O^{t}Bu)$_3$] to -35 °C for 3 days. ^{1}H NMR (C_6D_6, 700 MHz): δ 1.39 (s, 27H). ^{13}C{^{1}H} NMR (C_6D_6, 700 MHz): δ 69.9 (C(CH$_3$)$_3$), 34.7 (C(CH$_3$)$_3$). Anal. Calc. for $KC_{12}H_{27}GeO_3$: C, 43.53; H, 8.22 %. Found: C, 43.33; H, 7.98 %.

[Ge(O^{t}Bu)$_2$] (1): To a solution of K[Ge(O^{t}Bu)$_3$] (0.331 g, 1.00 mmol) in 2 mL of benzene was added Cl_2Ge•dioxane (0.116 g, 0.500 mmol). The reaction mixture was stirred at room temperature for 1 h and then the mixture was filtered through a pad of Celite. The volatiles were removed from the filtrate *in vacuo* to give [Ge(O^{t}Bu)$_2$] (**1**) (0.312 g, 94 %) as a white solid. [Ge(O^{t}Bu)$_2$] (**1**) can be recrystallized from a saturated solution of pentane cooled to -35 °C for one week (crystal yield 54%). ^{1}H NMR (C_6D_6, 500 MHz): δ 1.48 (s, 18H, C(CH_3)$_3$). ^{13}C{^{1}H} NMR (C_6D_6, 500 MHz): The peak pattern in this NMR spectra indicates the possible presence of both monomer [δ 30.7 (C(*C*H$_3$)$_3$), 74.6 (*C*(CH$_3$)$_3$)] and dimer [^{t}BuOGe(μ-O^{t}Bu)$_2$GeO^{t}Bu]: bridging O^{t}Bu δ 34.4 (C(*C*H$_3$)$_3$), 77.4 (*C*(CH$_3$)$_3$); exocyclic O^{t}Bu δ 32.4 (C(*C*H$_3$)$_3$), 72.2 (*C*(CH$_3$)$_3$). Anal. Calc. for $C_9H_{18}GeO_2$: C, 43.90; H, 8.29 %. Found: C, 43.73; H, 8.23. Diffusion ordered NMR spectroscopy (DOSY) gave a diffusion constant (D) of 10.17(3) m^2 s^{-1}, equating to a solvodynamic radius of 3.38(1) Å with the literature C_6D_6 viscosity value of 0.6392 Pa•s.[S8]

Synthesis of [GeH$_{1.64}$(O^{t}Bu)$_{0.36}$]$_n$ (2a) from HBpin: In a nitrogen-filled glove box, 119.4 μL (0.822 mmol) of HBpin was added to a solution of [Ge(O^{t}Bu)$_2$] (**1**) (60.0 mg, 0.274 mmol) in 1 mL of benzene at room temperature. After 2 hrs of stirring, an insoluble yellow/orange solid formed. The precipitate was allowed to settle, and the mother liquor was decanted away. The remaining solid was washed with benzene (4 × 5 mL) and dried under vacuum to give **2a** as a bright yellow-orange solid (15 mg, 55 %; yield based on the formula [GeH$_{1.64}$(O^{t}Bu)$_{0.36}$]$_n$). The expected by-product, ^{t}BuOBpin, was identified by ^{1}H, ^{11}B and ^{13}C{^{1}H} NMR spectroscopy, see Figs. S6-S8.

Synthesis of [GeH$_{1.65}$(O^{t}Bu)$_{0.35}$]$_n$ (2b) from HBcat: In a nitrogen-filled glove box, 43 μL (0.40 mmol) of HBcat was added to a solution of [Ge(O^{t}Bu)$_2$] (**1**) (40.0 mg, 0.183 mmol) in benzene (1 mL) at room temperature. After the resulting mixture was stirred for 2 hrs, the precipitate was allowed to settle and the mother liquor decanted away. The remaining solid was washed with benzene (4 × 5 mL), dried under vacuum to give **2b** as a bright yellow solid (10 mg, 55 %, yield based on the formula [GeH$_{1.65}$(O^{t}Bu)$_{0.35}$]$_n$). The expected by-product, ^{t}BuOBcat, was identified by ^{1}H, ^{11}B and ^{13}C{^{1}H} NMR spectroscopy, see Figs S8-S10. IR (ATR): 3060 cm^{-1} (C-H, Ar), 2956 cm^{-1} (C-H), 2038 cm^{-1} (Ge-H), 1102 cm^{-1} (C-O), 833-776 cm^{-1} (H-Ge-H). Raman: 2047 cm^{-1} (Ge-H), 295 cm^{-1} (Ge-Ge). Anal. Calc. for [GeH$_{1.65}$(O^{t}Bu)$_{0.35}$]$_n$: C, 16.65; H, 4.78 %. Found: C, 16.42; H, 2.53 %. Molecular formula calculated based on carbon content.

Synthesis of [^{i}Bu$_2$AlO^{t}Bu]$_2$ from DIBAL-H and HO^{t}Bu: Using Schlenk techniques, 318 μL of a 1.0 M solution of DIBAL-H in hexanes (0.16 mmol of dimer [HAl^{i}Bu$_2$]$_2$) was added dropwise into a Teflon Schlenk flask containing a solution of HO^{t}Bu (23.6 mg, 0.318 mmol) in 1 mL of benzene, at room temperature. After the resulting mixture was stirred for 1 hr, the volatiles were removed under vacuum until a white solid remained (36 mg, 53%). The expected product, [^{i}Bu$_2$AlO^{t}Bu]$_2$, was identified by ^{1}H and ^{13}C{^{1}H} NMR spectroscopy. ^{1}H NMR (C_6D_6, 400 MHz): δ 0.26 (d, 8H, $^3J_{HH}$ = 6.9 Hz, (CH_2), 1.19 (d, 24H, $^3J_{HH}$ = 6.5 Hz, (CH(CH_3)$_2$), 1.29 (s, 18H, (OC(CH_3)$_3$), 2.02-2.09 (m, 4H, (CH(CH$_3$)$_2$). ^{13}C{^{1}H} NMR (C_6D_6, 400 MHz): δ 26.0 (*C*H$_2$), 26.3 (*C*H(CH$_3$)$_2$), 28.9 (CH(*C*H$_3$)$_2$), 31.8 (OC(*C*H$_3$)$_3$), 74.8 (O*C*(CH$_3$)$_3$). HR-MS (EI) ($C_{24}H_{54}Al_2O_2$): m/z calcd. for ($C_{20}H_{45}Al_2O_2$) 371.30505; found 371.30522 (Δppm = 0.4).

Attempted Synthesis of [GeH$_2$]$_n$ from DIBAL-H: In a nitrogen-filled glove box, 402 μL of a 1.0 M solution of DIBAL-H in hexanes (0.40 mmol of monomer HAl^{i}Bu$_2$) was added to a Teflon Schlenk flask containing [Ge(O^{t}Bu)$_2$] (**1**) (40 mg, 0.18 mmol) dissolved in 2 mL of pentane. The

reaction vessel was removed from the glovebox and heated to 70 °C (with stirring) for 2 hrs. The product was then isolated inside the glovebox. The slurry was allowed to settle, and the supernatant was decanted. The precipitate was washed with 5 mL of pentane, allowed to settle, and the supernatant decanted; this washing procedure was repeated four times to ensure the removal of all soluble materials. Finally, all volatiles were removed under vacuum until an orange-yellow powder remained (8.8 mg, 49%, yield based on the formula $[GeH_{1.65}(O^tBu)_{0.35}]_n$); elemental analysis was not consistent with the formation of $[GeH_2]_n$ as a high C content was detected. The DIBAL-derived side products isolated in the supernatant (volatiles removed by vacuum) were characterized by ^1H NMR and $^{13}C\{^1H\}$ NMR spectroscopy, see Figs. S14 and S15. IR (ATR) 2929-2873 cm^{-1} (C-H), 1990 cm^{-1} (Ge-H), 1070 cm^{-1} (C-O), 808-769 cm^{-1} (H-Ge-H). Raman: 1998 cm^{-1} (Ge-H), 291 cm^{-1} (Ge-Ge). Anal. Calc. for $[GeH_{1.65}(O^tBu)_{0.35}]_n$: C, 16.65; H, 4.78 %Found: C, 16.73; H, 4.14 %.

Synthesis of $[GeH_{1.92(}OtBu)_{0.08}]_n$ (2c) from excess HBpin at 70 °C: In a nitrogen-filled glove box, 529.6 µL (3.65 mmol) of HBpin was added to a solution of $[Ge(O^tBu)_2]$ (**1**) (80.0 mg, 0.365 mmol) in 2 mL of benzene at room temperature. The solution was brought of the glove box in a Teflon valve-sealed flask and stirred for 16 hrs at 70 °C, which afforded an yellow-orange insoluble solid. The precipitate was allowed to settle, and the mother liquor was decanted away. The remaining solid was washed with benzene (4 × 5 mL) and dried under vacuum to give **2c** as a bright yellow-orange solid (20 mg, 68 % yield based on $[GeH_{1.92}(O^tBu)_{0.08}]_n$). The expected by-product, ^{t}BuOBpin, was identified by ^1H, ^{11}B and $^{13}C\{^1H\}$ NMR, see Figs. S16-S18. IR (ATR): 2957 cm^{-1} (C-H), 2013 cm^{-1} (Ge-H), 1069 cm^{-1} (C-O), 772-809 cm^{-1} (H-Ge-H). Raman: 2021 cm^{-1} (Ge-H), 292 cm^{-1} (Ge-Ge). Anal. Calc. for $[GeH_{1.92}(O^tBu)_{0.08}]_n$: C, 4.78; H, 3.28 %. Found: C, 4.82; H, 1.96 %. Molecular formula calculated based on carbon content. No green color was observed in the burning of product **2c**, indicating that the boron incorporation in the solid was less than *ca*. 0.085 % by mass.

Synthesis of GeI_4 from $[GeH_{1.92}(O^tBu)_{0.08}]_n$ (2c) and I_2: In a nitrogen-filled glove box, a solution of I_2 (0.0948 g, 0.747 mmol) dissolved in 2 mL of C_6D_6 was added to a vial containing 0.020 g (0.25 mmol) of $[GeH_{1.92}(O^tBu)_{0.08}]_n$ (**2c**) at room temperature. The mixture was stirred for 1 hr resulting in the formation of a dark yellow solution and a dark-purple solid. The reaction mixture was filtered through Celite and the volatiles were removed from the filtrate to give GeI_4 (yellow solid, 0.126 g, 87 %). Bright orange crystals were grown by sublimation of the yellow solid at room temperature under dynamic vacuum (0.150 mtorr) for 3 hrs and identified by pXRD (see Fig. S43). Mp: 144-146 °C.[S9]

Attempted reaction between 2,3-dimethyl-1,3-butadiene and 2c: Under N_2, a solution of 2,3-dimethyl-1,3-butadiene (20.4 mg, 0.248 mmol) in 1 mL of C_6D_6 was added to **2c** (0.010 g, 0.12 mmol) at room temperature. After stirring the mixture at 60 °C for 16 hrs, analysis of the reaction mixture by ^1H and $^{13}C\{^1H\}$ NMR spectroscopy indicated that no reaction transpired.

Attempted reaction between 1,2-^{i}Pr$_2$P(C$_6$H$_4$)BCy$_2$ (PB) and 2c: Under N_2, a solution of **PB** (91.9 mg, 0.248 mmol) in 1 mL of C_6D_6 was added to **2c** (0.010 g, 0.12 mmol) at room temperature. After stirring the mixture at 60 °C for 16 h, analysis of the reaction mixture by ^{11}B and ^{31}P NMR spectroscopy showed that no reaction had transpired.

In-situ trapping of GeH_2 with 1,2-^{i}Pr$_2$P(C$_6$H$_4$)BCy$_2$ (PB): Under N_2, **PB** (0.074 g, 0.20 mmol) and $[Ge(O^tBu)_2]$ (**1**) (0.022 g, 0.10 mmol) were combined in a J-Young tube, *ca*. 0.6 mL of THF

and HBpin (0.20 mmol, 38.0 μL) were then added. The reaction progress was monitored by $^{31}P\{^{1}H\}$ and ^{11}B NMR spectroscopy, which showed the formation of the known germanium(II) dihydride complex **PB{GeH$_2$}**[S3] in about 30 % yield, along with unreacted **PB** (*ca.* 20 %)[S3] and another unknown product (*ca.* 50 % according to ^{31}P NMR spectroscopy, see Figs. S30 and S31). A duplicate reaction was conducted in the absence of HBpin, and $^{31}P\{^{1}H\}$ and ^{11}B NMR spectroscopy showed resonances for only the free **PB** species, indicating a lack of coordination between **PB** and [Ge(O^{t}Bu)$_2$] (**1**) under these conditions.

Preparation of ImMe$_2$•Ge(O^{t}Bu)$_2$ (3): To a vial containing ImMe$_2$•GeCl$_2$ (0.423 g, 1.77 mmol) and K[O^{t}Bu] (0.396 g, 3.53 mmol) was added 15 mL of benzene. The mixture was stirred for 18 h to give a turbid orange colored mixture. The resulting precipitate was allowed to settle and the supernatant was filtered through Celite to give a yellow filtrate. Removal of the volatiles from the filtrate via freeze-drying under vacuum gave ImMe$_2$•Ge(O^{t}Bu)$_2$ (**3**) as a yellow solid (0.421 g, 76 %). Crystals of suitable quality for single crystal X-ray crystallography were obtained by cooling a concentrated solution of **3** in toluene to -35 °C for 3 days. ^{1}H NMR (C_6D_6, 500 MHz): δ 1.62 (s, 18H, OC(C*H*$_3$)$_3$), 3.52 (s, 6H, NC*H*$_3$), 5.54 (s, 2H, N(C*H*)$_2$N), $^{13}C\{^{1}H\}$ NMR (C_6D_6, 700 MHz): δ 34.0 (OC(*C*H$_3$)$_3$), 35.8 (NCH$_3$), 70.2 (O*C*(CH$_3$)$_3$), 120.5 (N(*C*H)$_2$N). 175.9 (N*C*N). Mp: 83 °C (decomp.) Anal. Calc. for for $C_{13}H_{26}GeN_2O_2$: C, 49.57; H, 8.32; N, 8.89 % Found: C, 49.59; H, 8.33; N, 8.63 %.

Reaction of ImMe$_2$•Ge(O^{t}Bu)$_2$ (3) with HBpin: To a solution of ImMe$_2$•Ge(O^{t}Bu)$_2$ (0.136 g, 0.432 mmol) in 6 mL of benzene was added HBpin (0.563 mL, 4.32 mmol). The mixture changes rapidly from clear yellow to a yellow/orange slurry. The reaction is heated for 16 hrs at 70 °C. The precipitate was allowed to settle and the mother liquor was decanted away. The remaining precipitate was washed three times with benzene (3 × 3 mL) and then dried by vacuum to afford a Ge-H-rich highly air-sensitive orange-red powder (36 mg) that smokes immediately upon exposure to air. IR (ATR): 2972-2781 cm^{-1} (C-H), 1978 cm^{-1} (Ge-H), 1000-1200 cm^{-1} (N-C), 772-809 cm^{-1} (H-Ge-H). Anal. Calc. for [GeH$_2$]$_n$: H, 2.70 %. Found: C, 18.62; H, 3.94 %; N, 4.07 %. The elemental analysis indicates an approximate composition of (ImMe$_2$)$_3$Ge$_{21}$(O^{t}Bu)$_4$H$_{32}$ (C, 19.03; H, 4.38 %; N, 3.93 %.)

Thermolysis of 2c to form bulk germanium: A sample of 2c (100 mg) was transferred to a borosilicate glass boat inside an inert atmosphere glove box. Under flowing N2, the boat was transferred into the tube of a tube furnace (Lindberg 55035), which was pre-heated to 200 °C. The sample was held at 200 °C for two hours under static N_2, and then pushed to the end of the tube (outside the heating element) to cool to room temperature under flowing N_2. When cool, the samples were exposed to air and ground in a mortar and pestle to a fine powder for pXRD analysis. Furthermore, a sample of Ge, made from [Ge(O^{t}Bu)$_2$] and Me$_2$S•BH$_3$, was heated to 200 °C using the abovementioned procedure and analyzed by pXRD afterwards.

2. NMR Spectra

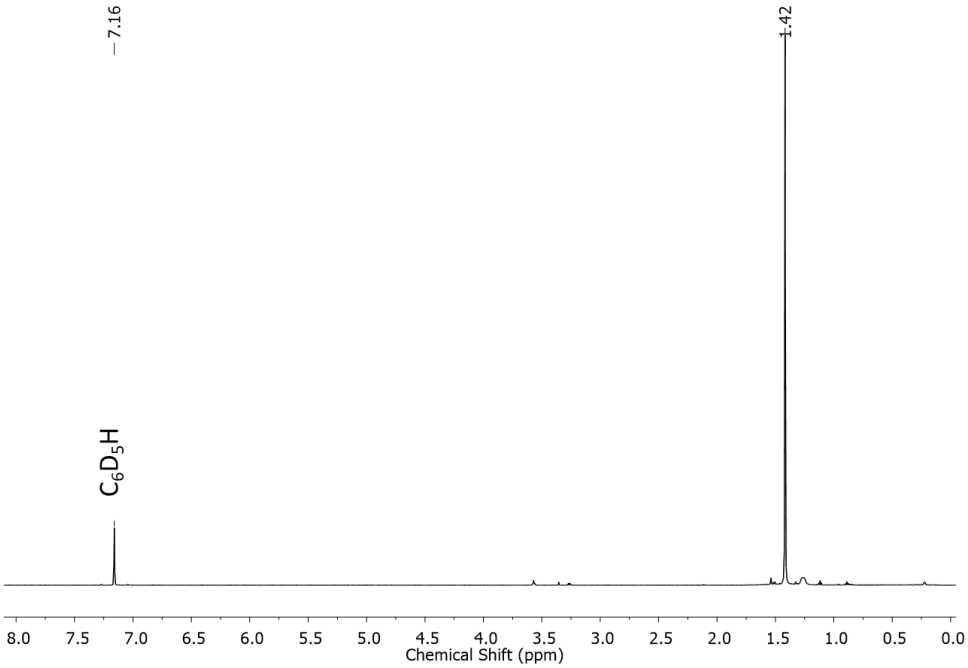

Fig. S1. ^{1}H NMR spectrum of $K[Ge(O^{t}Bu)_3]$ in C_6D_6.

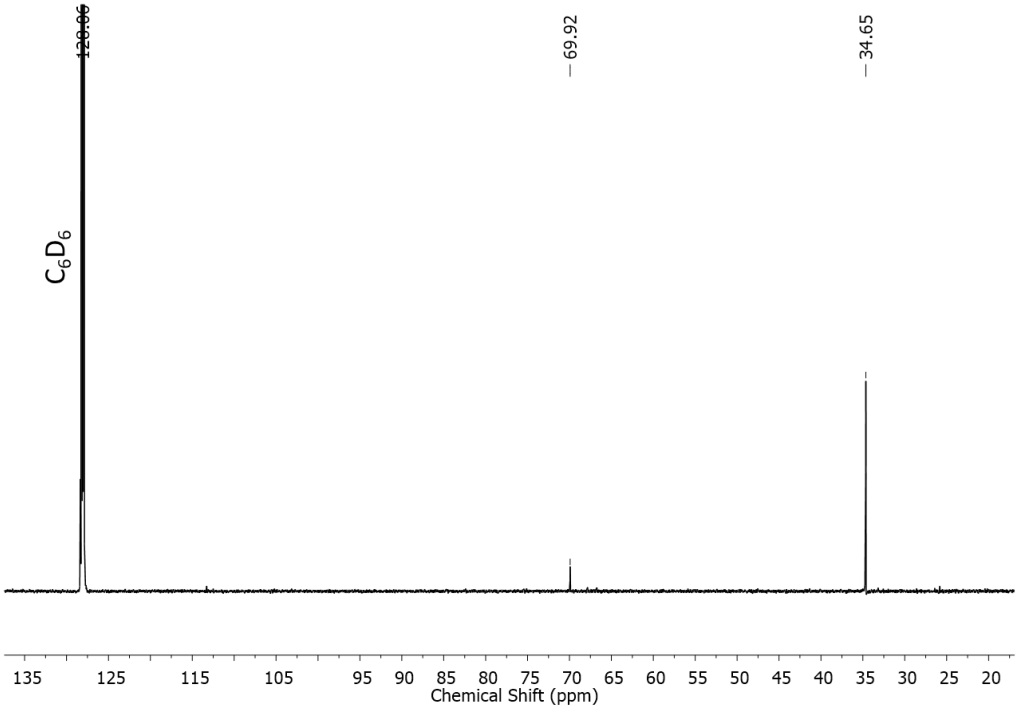

Fig. S2. $^{13}C\{^{1}H\}$ NMR spectrum of $K[Ge(O^{t}Bu)_3]$ in C_6D_6.

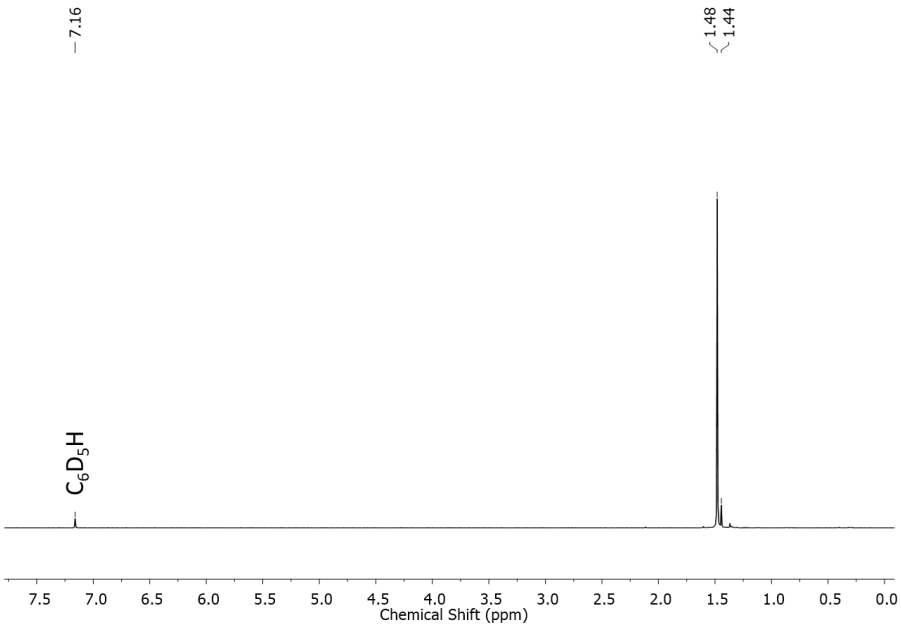

Fig. S3. ^{1}H NMR spectrum of [Ge(O^{t}Bu)$_2$] (**1**) in C_6D_6.

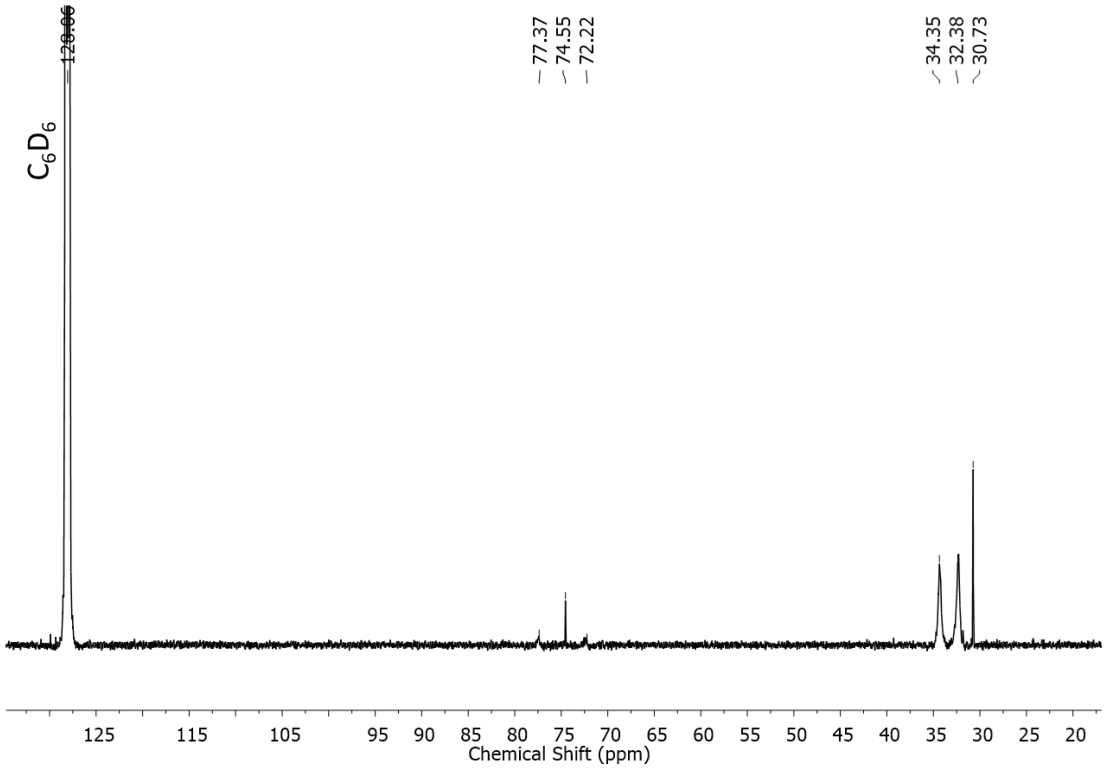

Fig. S4. $^{13}C\{^{1}H\}$ NMR spectrum of [Ge(O^{t}Bu)$_2$] (**1**) in C_6D_6. The peak pattern in this spectrum indicates the possible presence of both monomer [30.7 and 74.6 ppm] and dimer [bridging O^{t}Bu 34.4 and 77.4 ppm; exocyclic O^{t}Bu: 32.4 and 72.2 ppm].

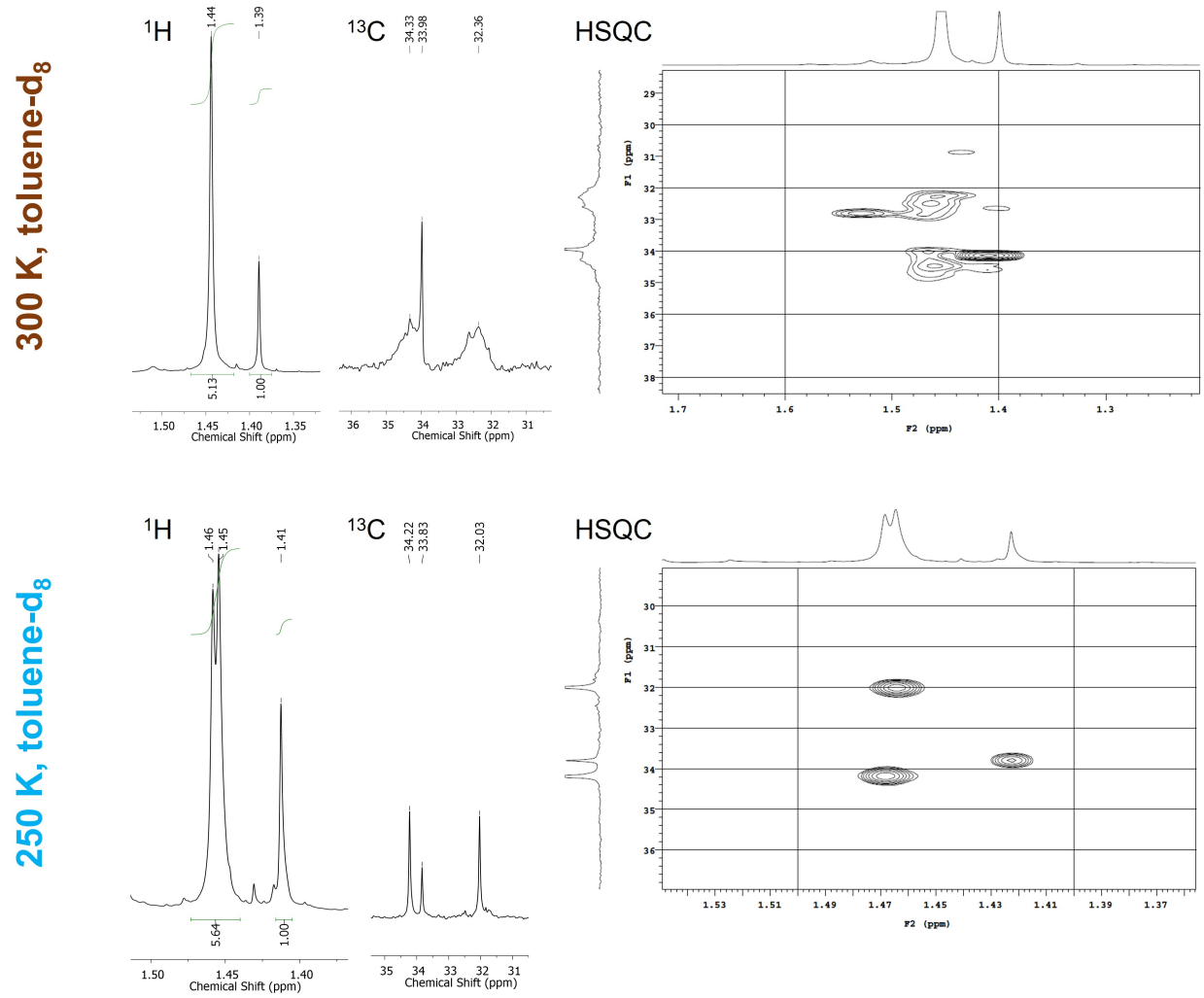

Fig. S5. VT-NMR and HSQC (Heteronuclear Single Quantum Coherence) experiments of $Ge(O^tBu)_2$ in toluene-d_8 were conducted. These experiments were conducted on the same bulk sample as in Figs. S3 and S4 (above in C_6D_6). The broad ^1H singlet identified as the dimer (1.44 ppm) is resolved into two environments (1.45 and 1.46 ppm, due to [^tBuOGe(μ-O^{t}Bu)$_2$GeO^{t}Bu] and [^{t}BuOGe(μ-O^t*Bu*)$_2$GeO^{t}Bu], respectively) at 253 K. These peaks are correlated with HSQC to the broad singlets in the $^{13}C\{^1H\}$ spectrum, which are also more defined at low temperature. The narrow singlet at 1.39 ppm in ^1H spectrum at 300 K is identified as the monomer of the same species; some exchange is noted at low temperatures by the increased relative integration of the dimer-assigned peak. The initial relative integrations between the two species are restored upon return to 300 K.

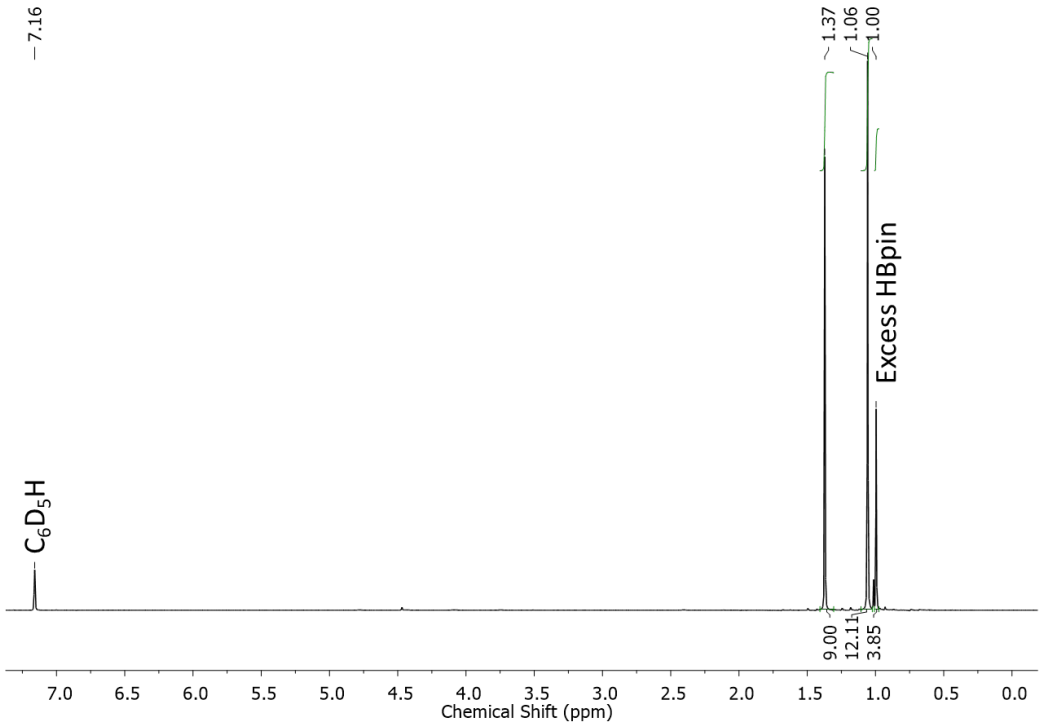

Fig. S6. ^{1}H NMR spectrum of ^{t}BuOBpin in C_6D_6, formed via the reaction of **1** with HBpin at room temperature (formation of **2a**).

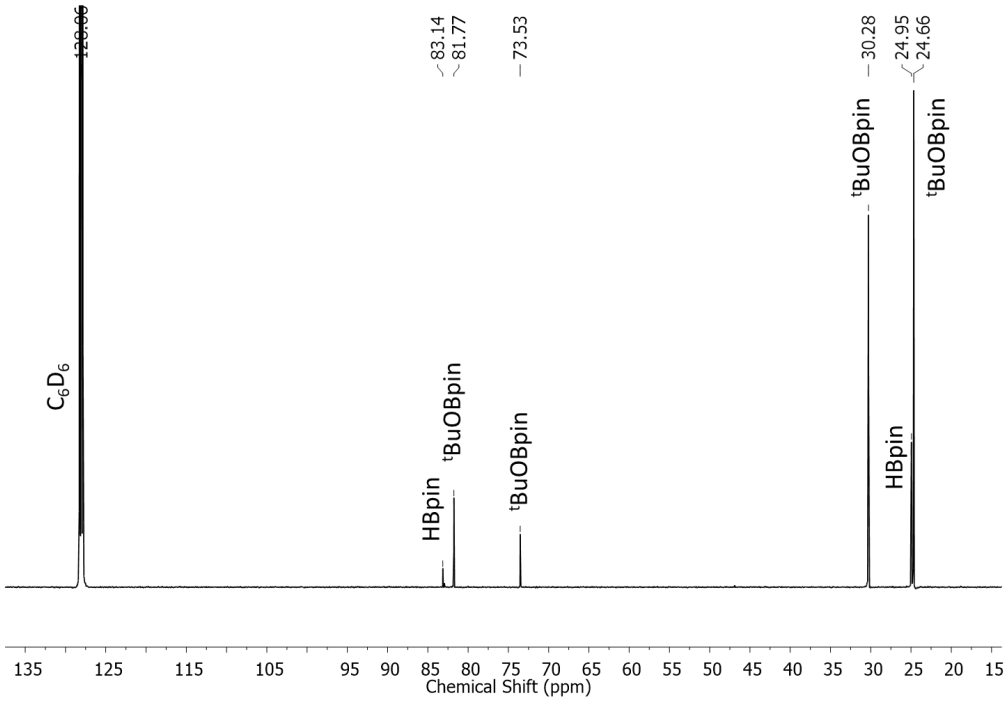

Fig. S7. $^{13}C\{^{1}H\}$ NMR spectrum of ^{t}BuOBpin in C_6D_6, formed via the reaction of **1** with HBpin at room temperature (formation of **2a**).

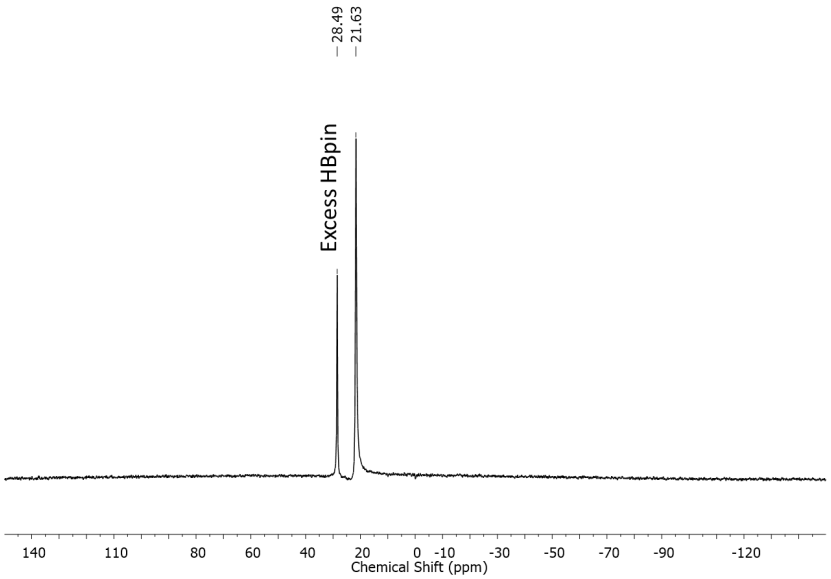

Fig. S8. $^{11}B\{^{1}H\}$ NMR spectrum of ^{t}BuOBpin in C_6D_6, formed via the reaction of **1** with HBpin at room temperature (formation of **2a**).

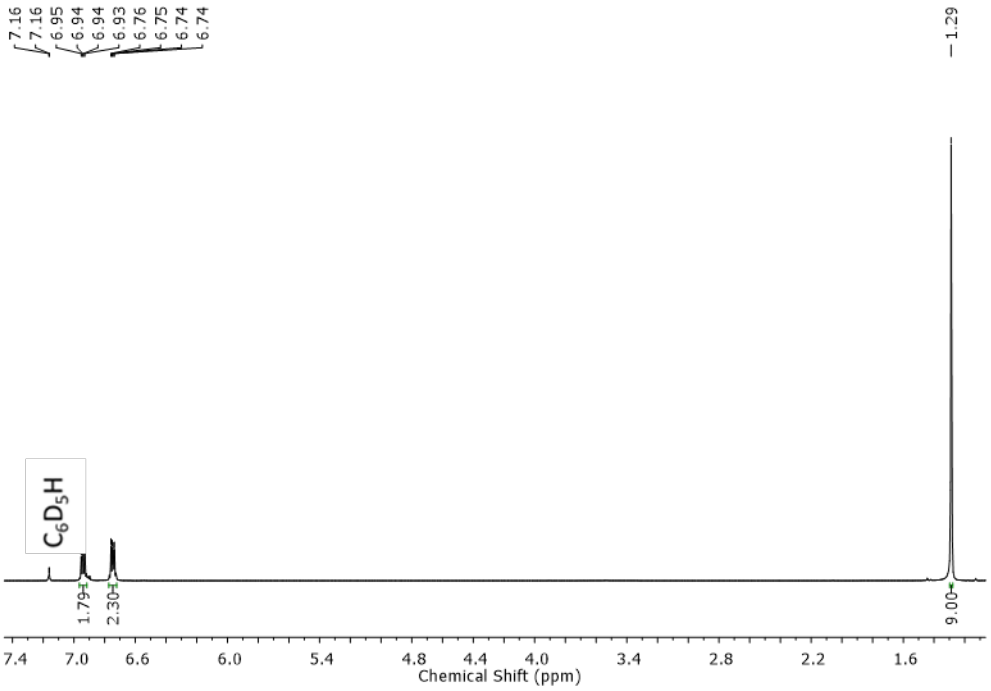

Fig. S9. ^{1}H NMR spectrum of ^{t}BuOBcat in C_6D_6, formed via the reaction of **1** with HBcat at room temperature.

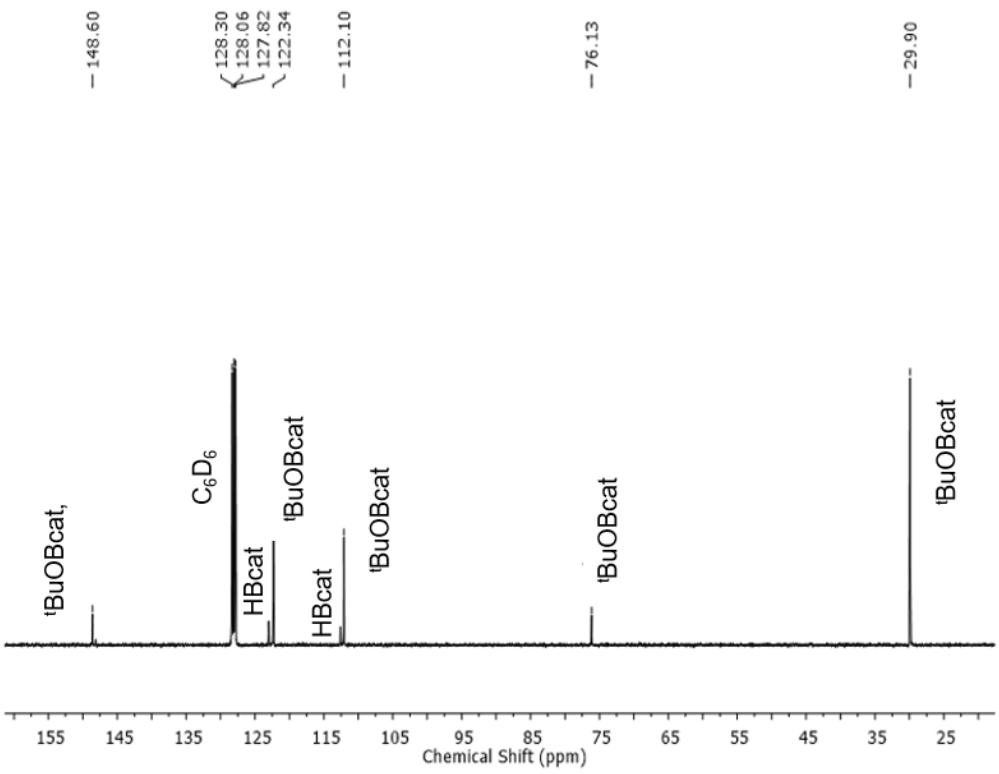

Fig. S10. $^{13}C\{^{1}H\}$ NMR spectrum of ^{t}BuOBcat in C_6D_6, formed via the reaction of **1** with HBcat at room temperature.

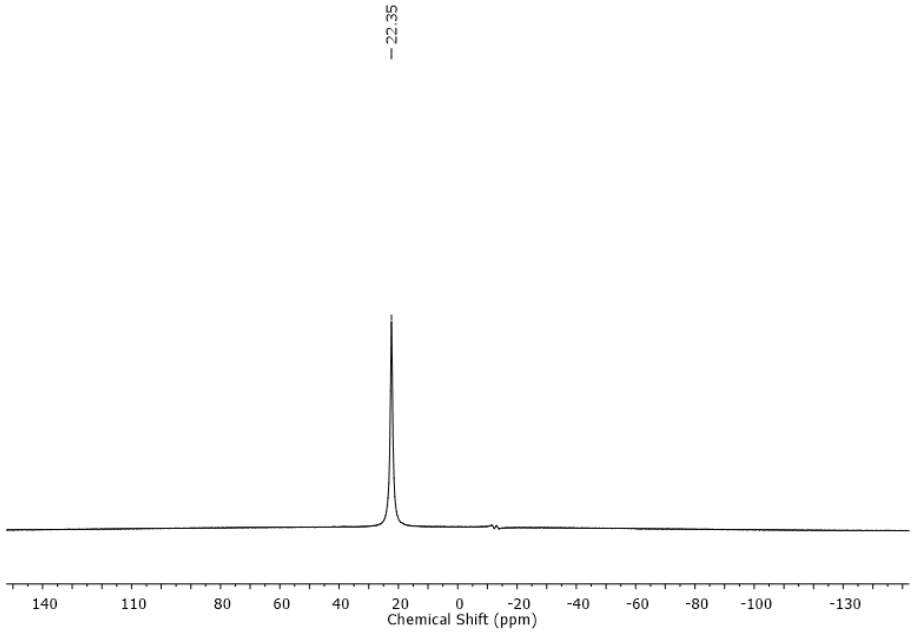

Fig. S11. $^{11}B\{^{1}H\}$ NMR spectrum of ^{t}BuOBcat in C_6D_6, formed via the reaction of **1** with HBcat at room temperature.

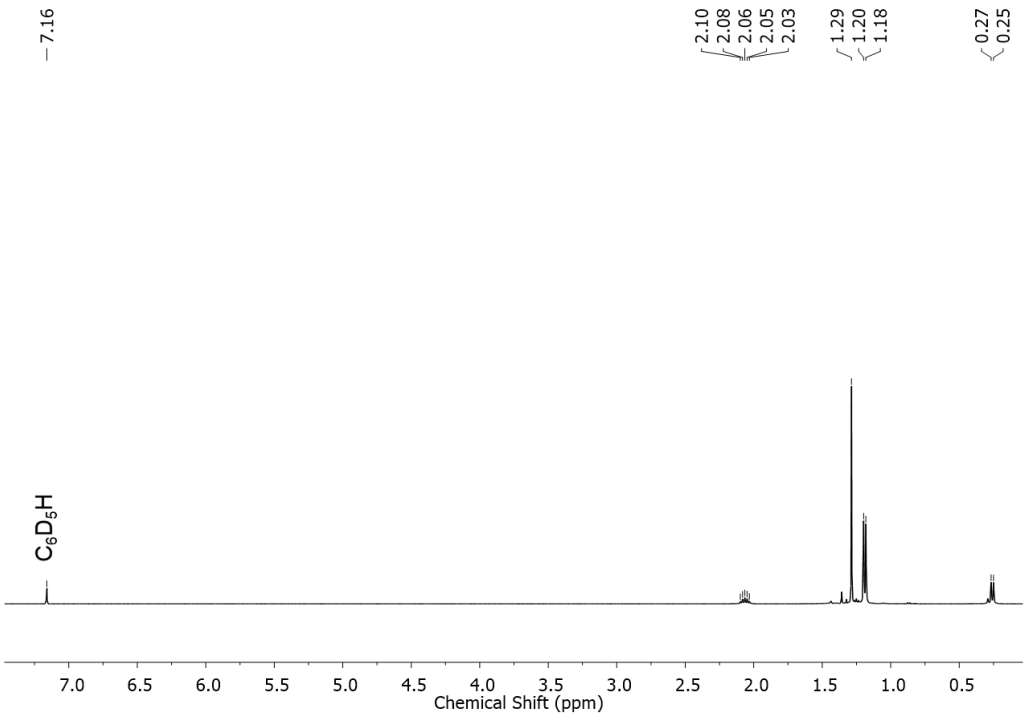

Fig. S12. ^{1}H NMR spectrum of [^{i}Bu$_2$AlO^{t}Bu]$_2$ in C_6D_6, obtained from the reaction of HO^{t}Bu with DIBAL-H at room temperature.

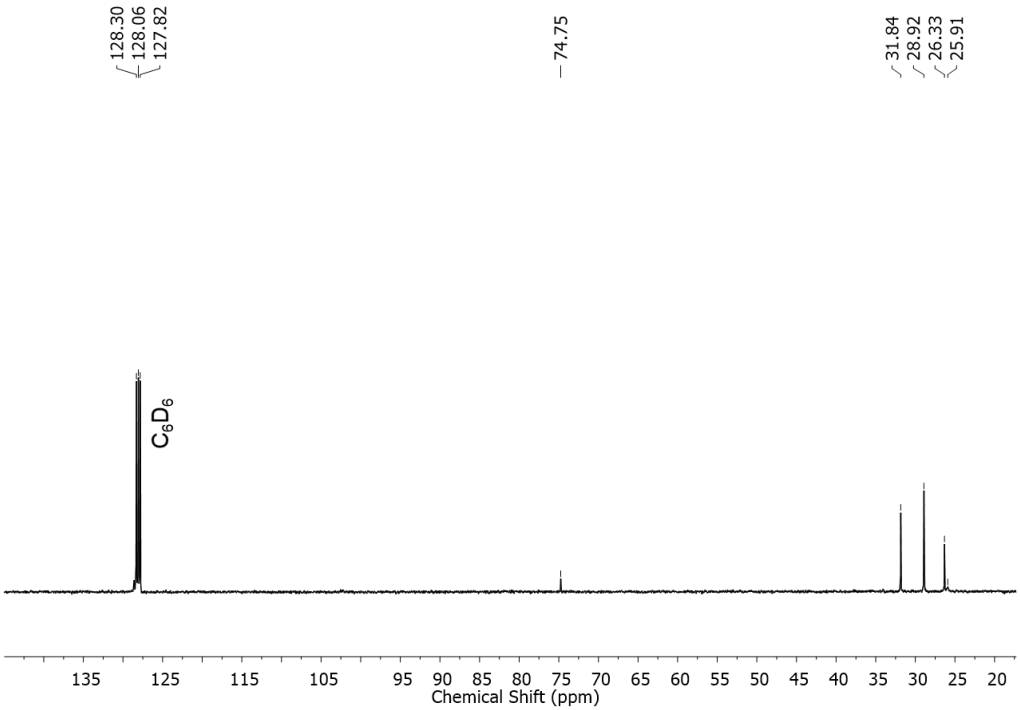

Fig. S13. ^{13}C {^{1}H} NMR spectrum of [^{i}Bu$_2$AlO^{t}Bu]$_2$ in C_6D_6, obtained from the reaction of HO^{t}Bu with DIBAL-H at room temperature.

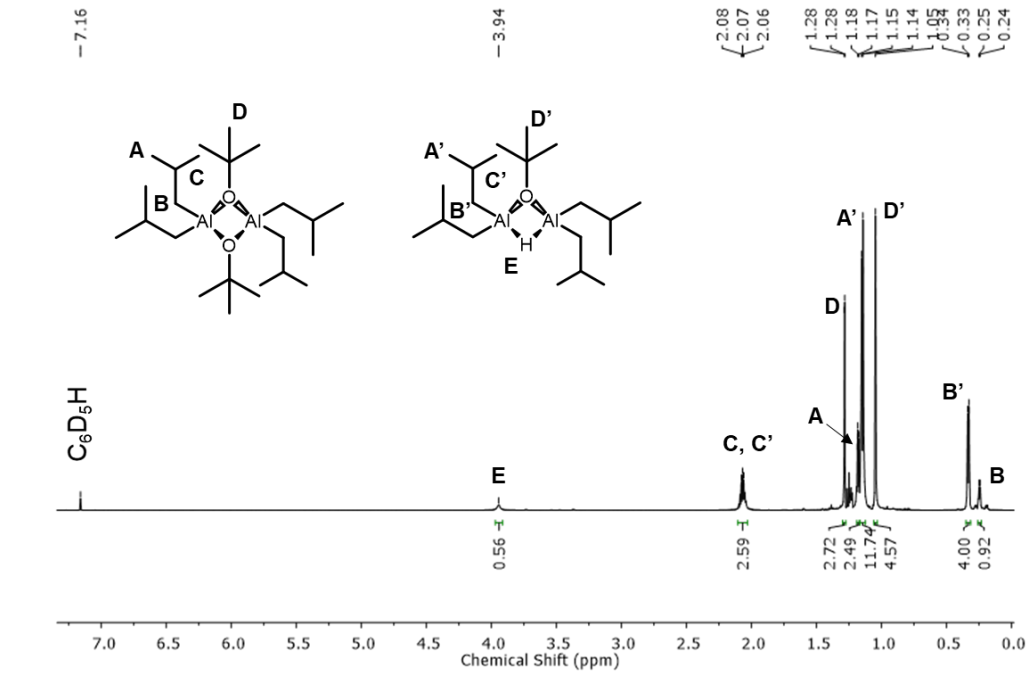

Fig. S14. ^{1}H NMR spectrum of the soluble side products in C_6D_6, obtained from the reaction of **1** with 2.2 equivalents of DIBAL-H at 70 °C.

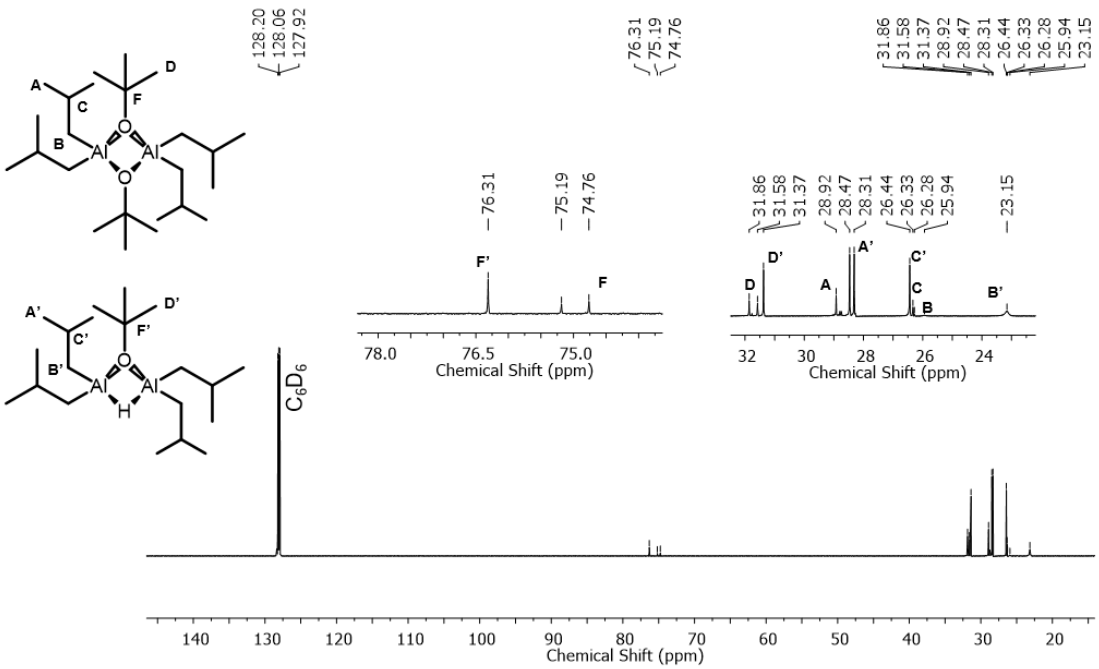

Fig. S15. ^{13}C {^{1}H} NMR spectrum of the soluble side products in C_6D_6, obtained from the reaction of **1** with 2.2 equivalents of DIBAL-H at 70 °C.

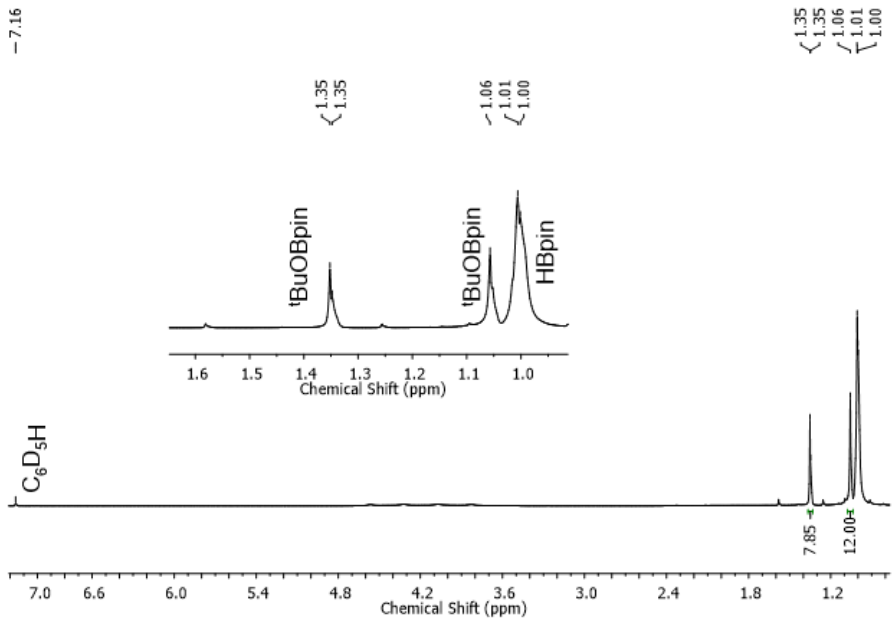

Fig. S16. ^{1}H NMR spectrum of the soluble side products obtained (in C_6D_6) from the reaction of **1** with 10 equivalents of HBpin at 70 °C.

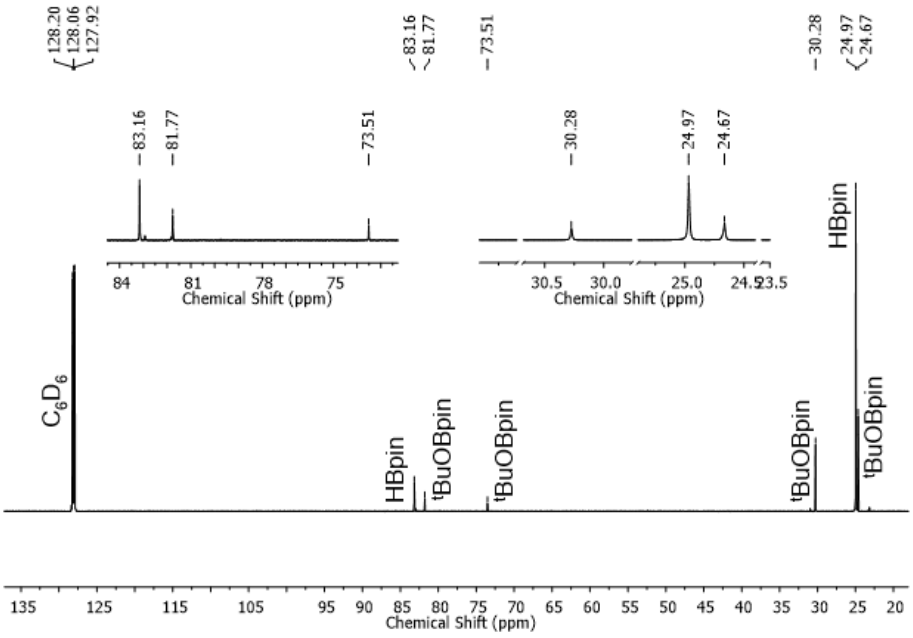

Fig. S17. $^{13}C\{^{1}H\}$ NMR spectrum of the soluble side products obtained (in C_6D_6) from the reaction of **1** with 10 equivalents of HBpin at 70 °C.

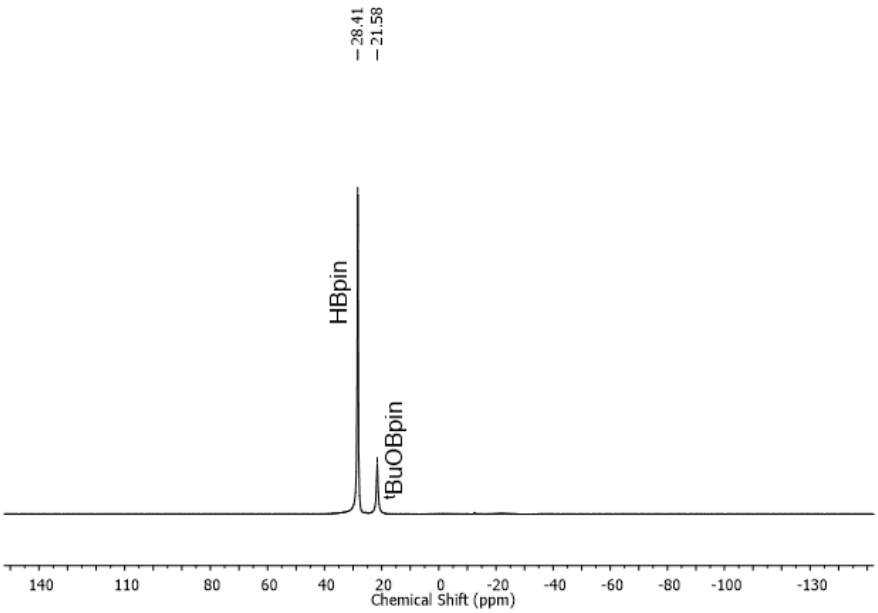

Fig. S18. $^{11}B\{^{1}H\}$ NMR spectrum of the soluble side products obtained (in C_6D_6) from the reaction of **1** with 10 equivalents of HBpin at 70 °C.

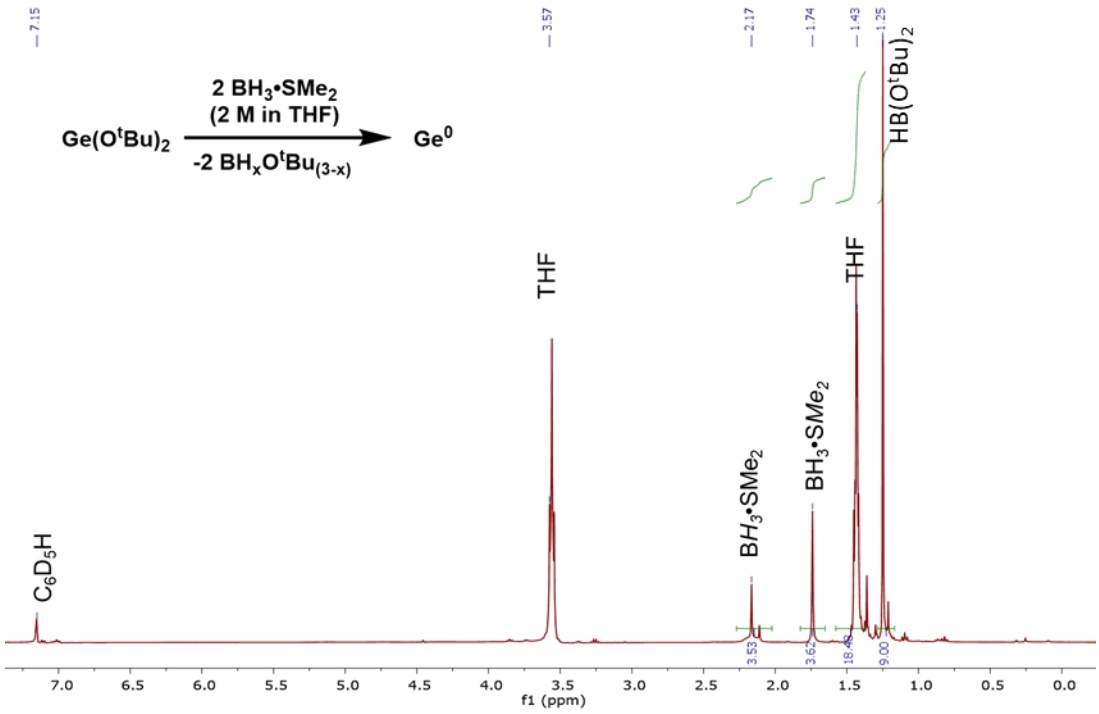

Fig. S19. *In-situ* ^{1}H NMR spectrum of the reaction of $[Ge(O^tBu)_2]$ (**1**) with three equivalents of $H_3B{\bullet}SMe_2$ (2.0 M solution in THF) in C_6D_6 after heating for 2 hrs at 70 °C.

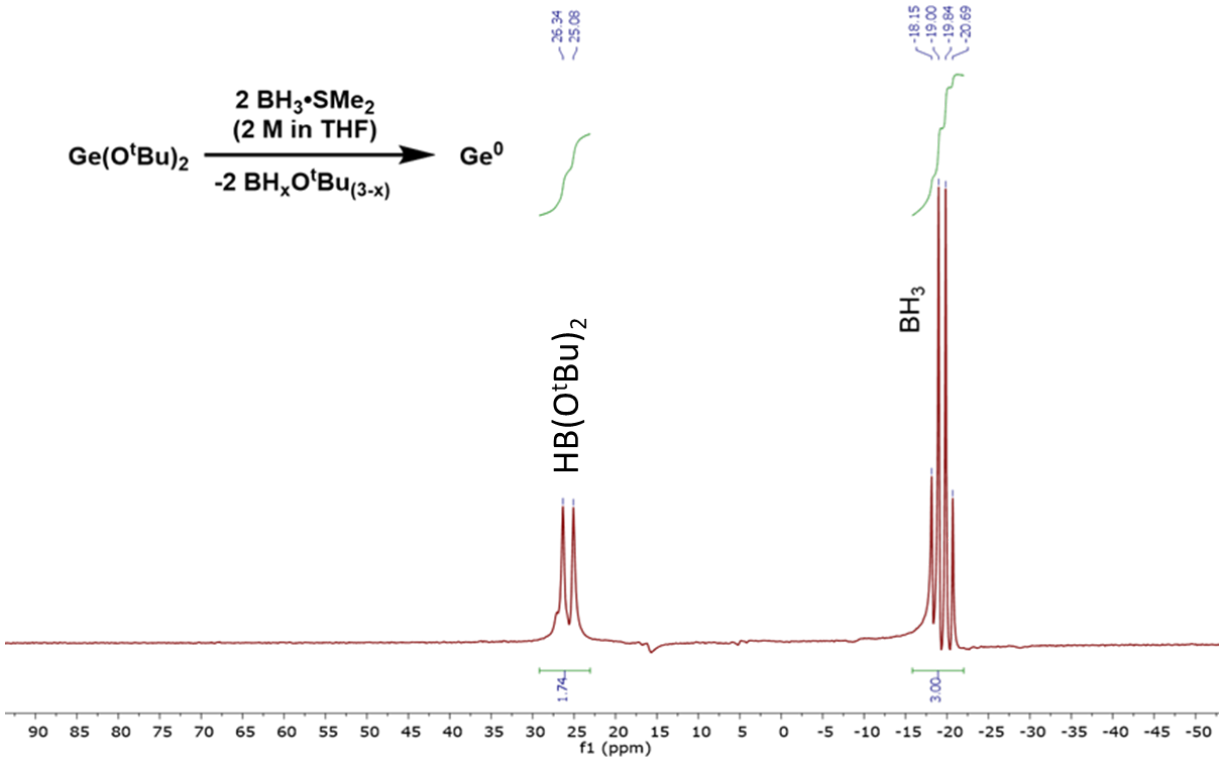

Fig. S20. *In-situ* ^{11}B NMR spectrum of the reaction of [Ge(O^{t}Bu)$_2$] (**1**) with three equivalents of H_3B•SMe_2 (2.0 M solution in THF) in C_6D_6 after heating for 2 hrs at 70 °C.

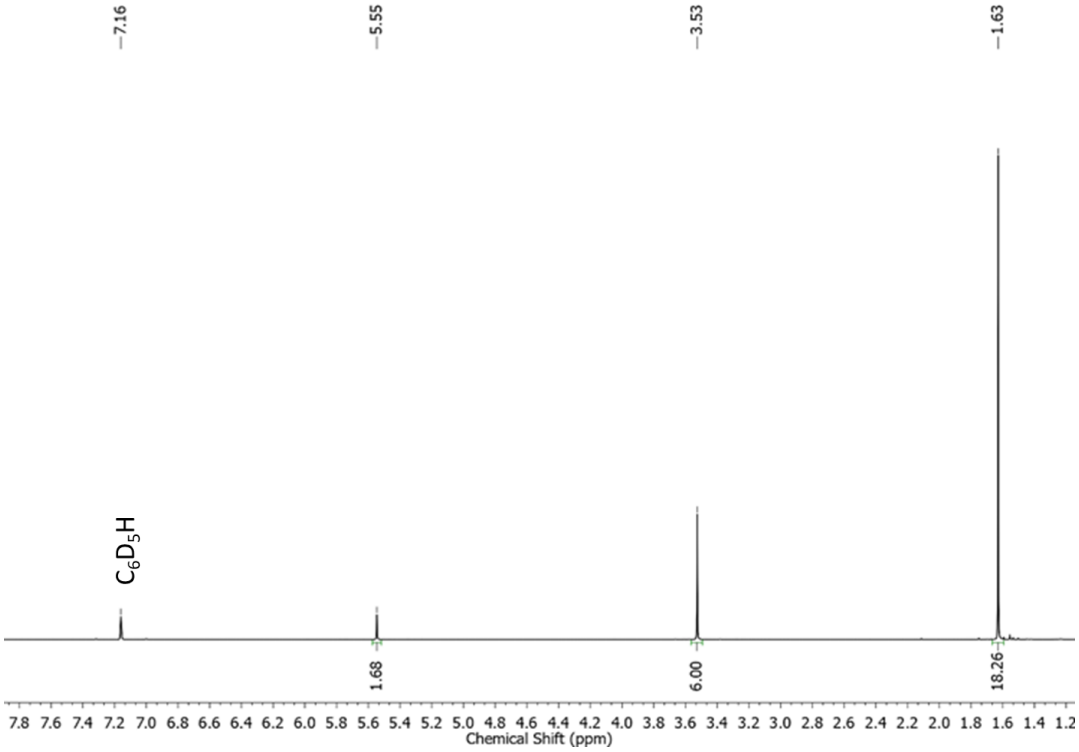

Fig. S21. ^{1}H NMR spectrum of ImMe$_2$•Ge(O^{t}Bu)$_2$ (**3**) in C_6D_6.

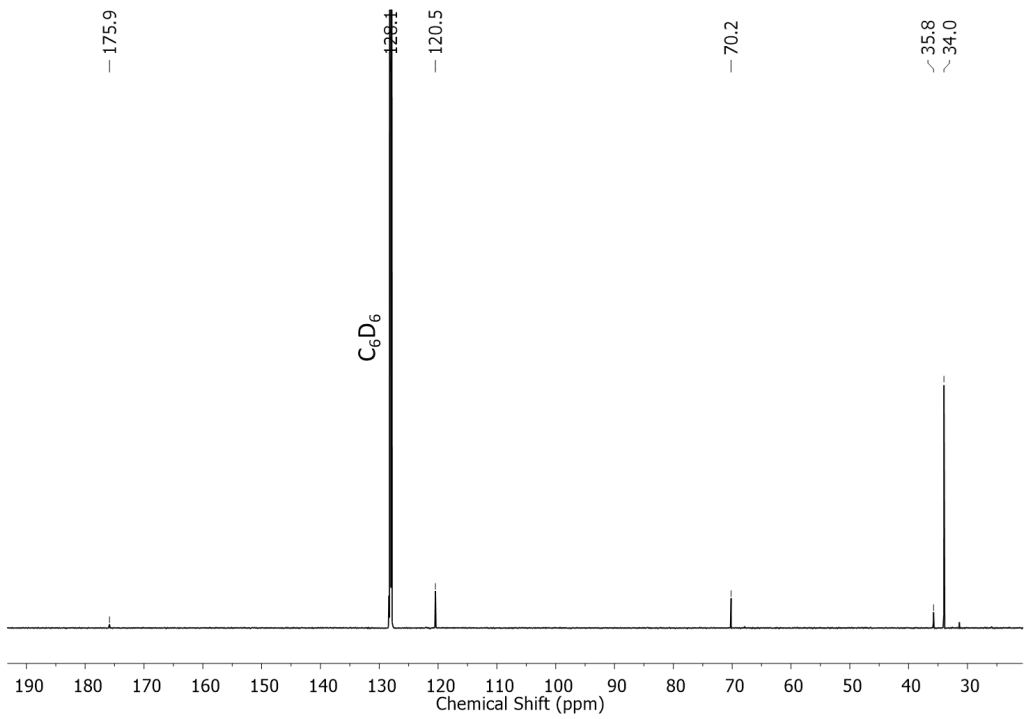

Fig. S22. $^{13}C\{^{1}H\}$ NMR spectrum of $ImMe_2$•$Ge(O^tBu)_2$ (**3**) in C_6D_6.

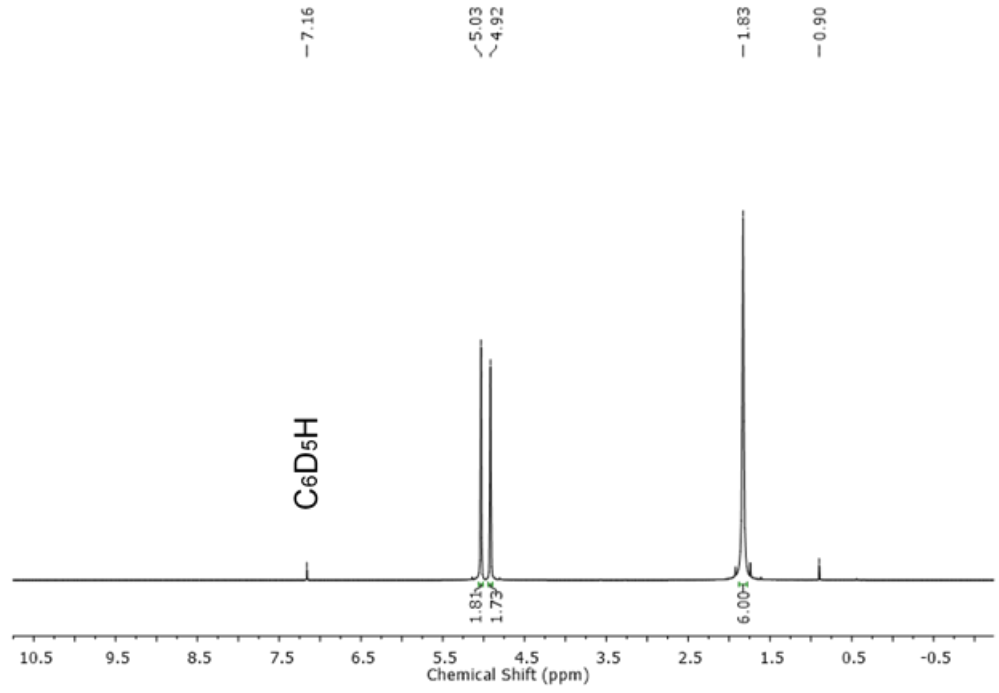

Fig. S23. ^{1}H NMR spectrum of 2,3-dimethyl-1,3-butadiene in C_6D_6.

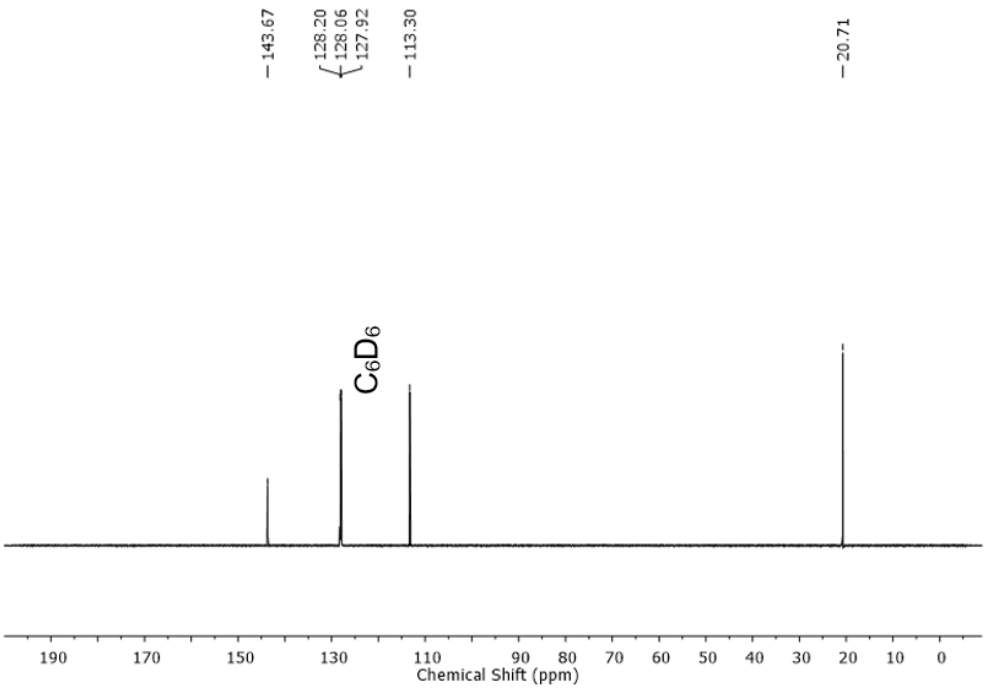

Fig. S24. $^{13}C\{^{1}H\}$ NMR spectrum of 2,3-dimethyl-1,3-butadiene in C_6D_6.

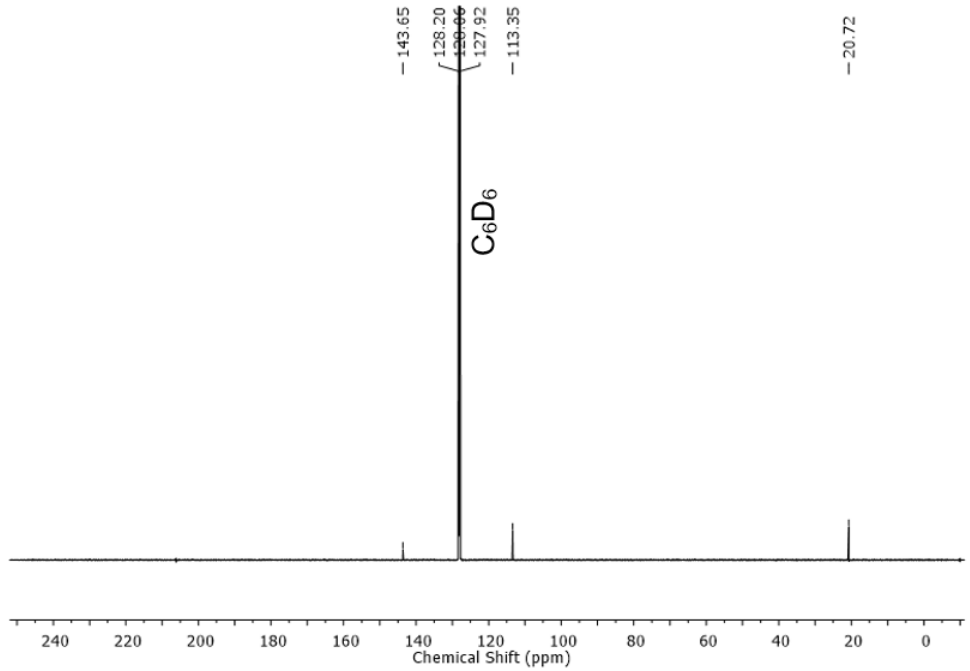

Fig. S25. $^{13}C\{^{1}H\}$ NMR spectrum of reaction mixture containing $[GeH_{1.92}(O^tBu)_{0.08}]_n$ (**2c**) and 2,3-dimethyl-1,3-butadiene after 16 hrs at 60 °C in C_6D_6.

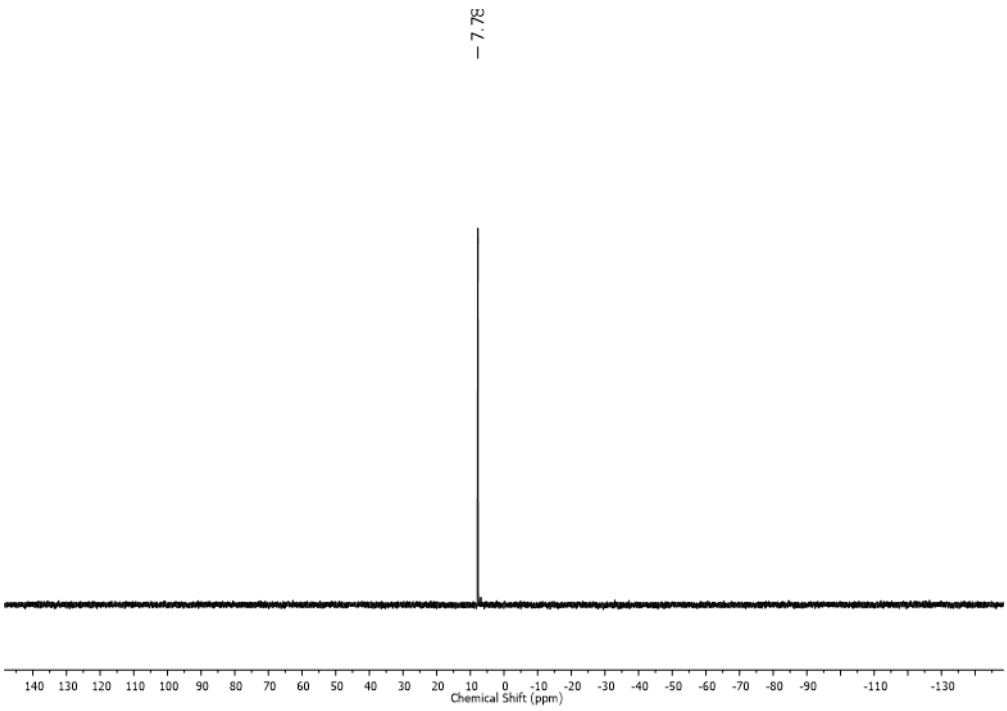

Fig. S26. $^{31}P\{^{1}H\}$ NMR spectrum of 1,2-$^{i}Pr_2P(C_6H_4)BCy_2$ (**PB**) in C_6D_6.

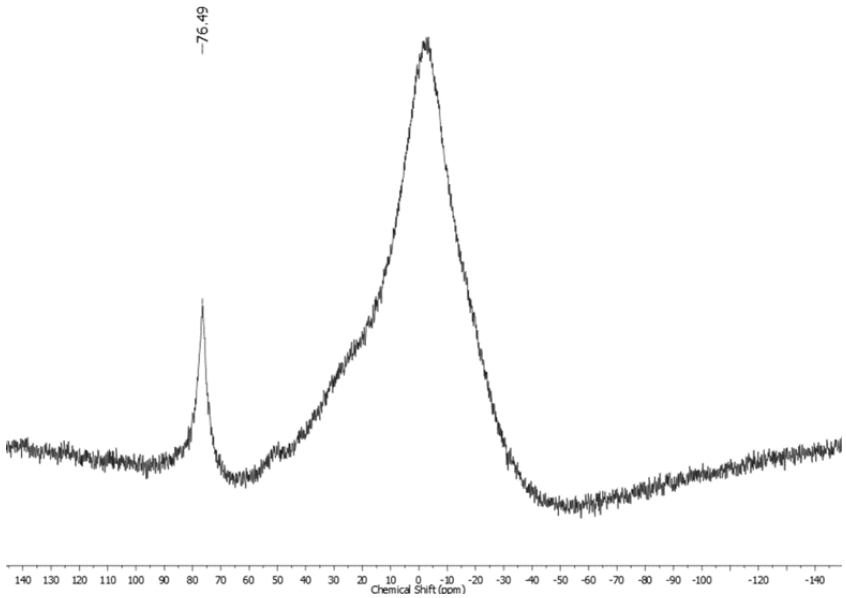

Fig. S27. $^{11}B\{^{1}H\}$ NMR spectrum of 1,2-$^{i}Pr_2P(C_6H_4)BCy_2$ (**PB**) in C_6D_6.

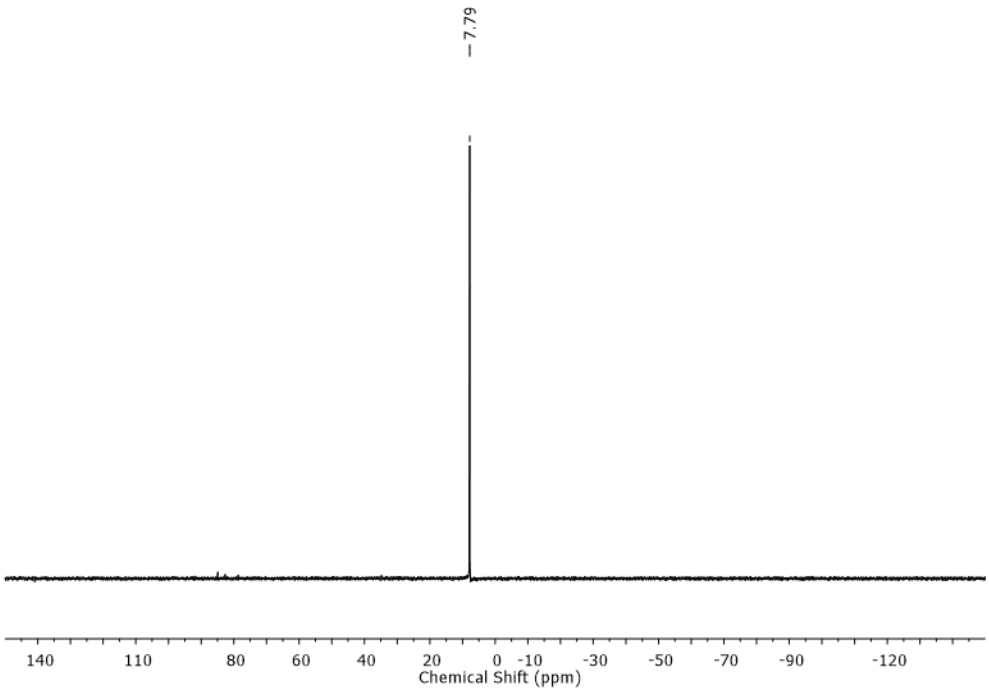

Fig. S28. $^{31}P\{^{1}H\}$ NMR spectrum of reaction mixture containing $[GeH_{1.92}(O^tBu)_{0.08}]_n$ (**2c**) and **PB** after 16 hrs at 60 °C in C_6D_6, showing no change compared to free **PB** (see Fig. S26).

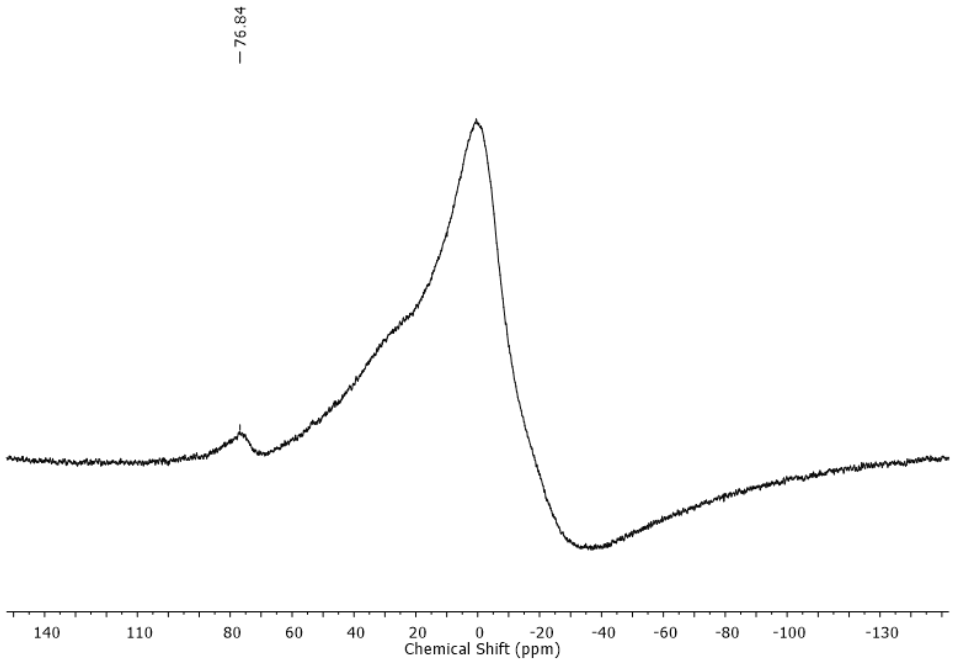

Fig. S29. $^{11}B\{^{1}H\}$ NMR spectrum of the reaction mixture containing $[GeH_{1.92}(O^tBu)_{0.08}]_n$ (**2c**) and **PB** after 16 hrs at 60 °C in C_6D_6, showing no change compared to free **PB** (see Fig. S27).

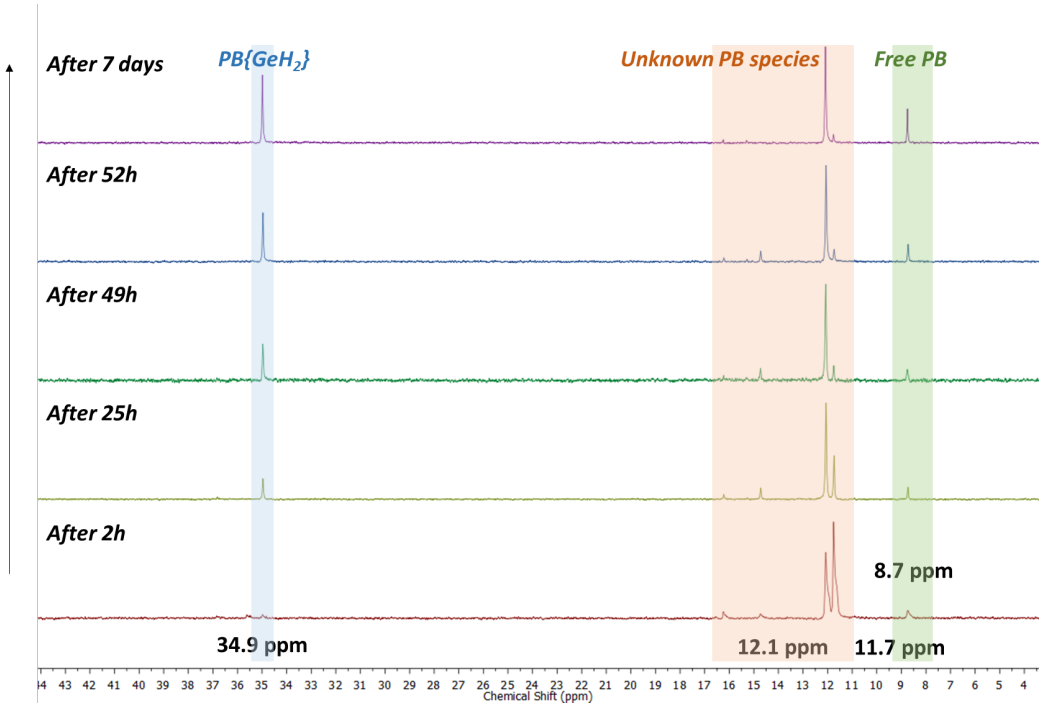

Fig. S30. $^{31}P\{^{1}H\}$ NMR spectrum of the reaction mixture from [Ge(O^{t}Bu)$_2$] (**1**) and 2 equiv. of HBpin in the presence of **PB**, showing the gradual production of **PB{GeH$_2$}** and an unknown **PB**-containing species.

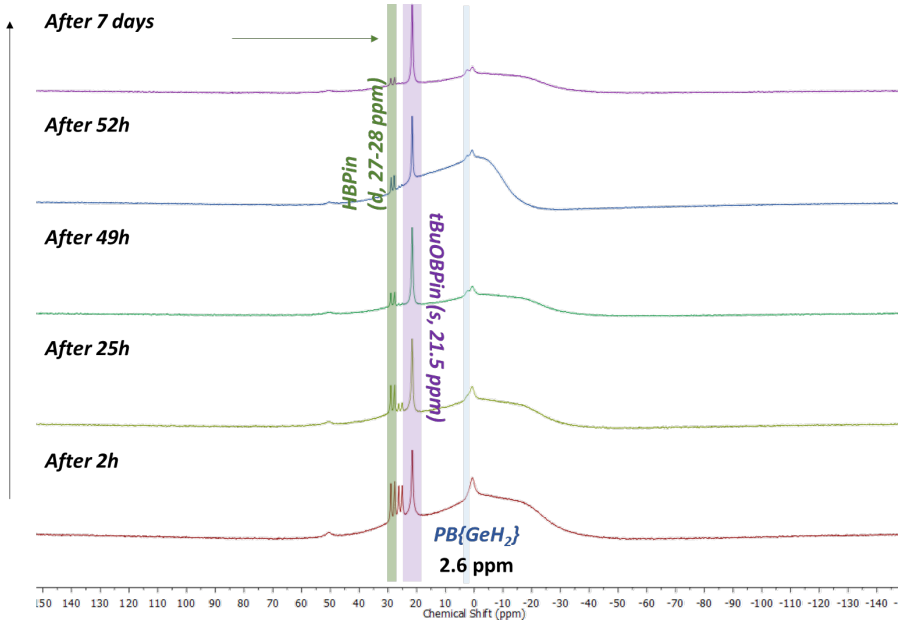

Fig. S31. ^{11}B NMR spectrum of the reaction mixture from [Ge(O^{t}Bu)$_2$] (**1**) and 2 equiv. HBpin in the presence of **PB**, showing the gradual production of **PB{GeH$_2$}** and an unknown **PB**-containing species. The production of ^{t}BuOBpin is also noted at 21.5 ppm.

3. X-ray Crystallographic Information

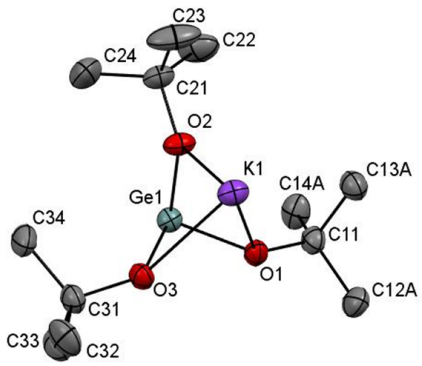

Fig. S32. Molecular structure of K[Ge(O^{t}Bu)$_3$] with thermal ellipsoids presented at a 30 % probability level. All hydrogen atoms have been omitted for clarity. Selected bond lengths [Å] and angles [°]: Ge1-O1 1.883(3), Ge1-O2 1.882(3), Ge1-O3 1.886(3); O1-Ge1-O2 93.54(15), O1-Ge1-O3 84.40(13), O2-Ge1-O3 93.97(14).

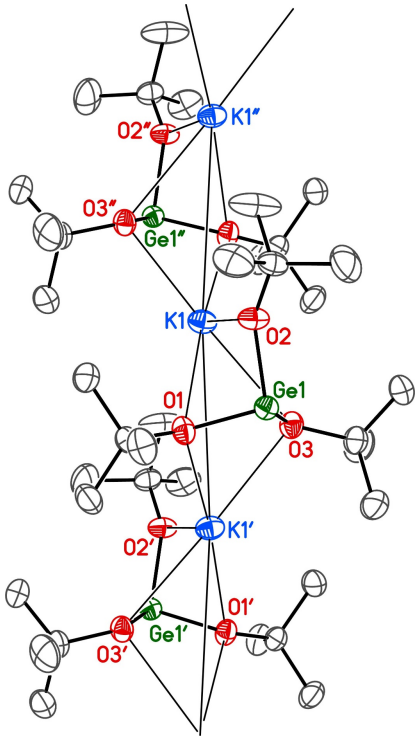

Fig. S33. View showing the one-dimensional polymeric structure of K[Ge(O^{t}Bu)$_3$]. Hydrogen atoms are not shown for clarity. Primed atoms at x+1/2, $\bar{y}$+1/2, $\bar{z}$+1. double-primed atoms at *x–1/2*, *$\bar{y}$+1/2*, *$\bar{z}$+1*. Thermal ellipsoids are presented at a 30 % probability level. Selected bond lengths [Å] and angles [°]: K1-O1 3.082(4), K1-O1″ 2.769(3), K1-O2 2.546(3), K1-O3 3.053(3), K1-O3″ 2.875(3), O1-K1-O1″ 175.07(6), O3-K1-O3″ 176.47(9), O1-K1-O2 57.39(9), O1-K1-O3 48.74(8), O2-K1-O3 58.09(10), Ge1-K1-Ge1″ 169.77.

Table S1. Crystallographic data for K[Ge(O^{t}Bu)$_3$]. CCDC Deposition Number 2094826

A. Crystal Data	
formula	$C_{12}H_{27}GeKO_3$
formula weight	331.02
crystal dimensions (mm)	0.08 × 0.06 × 0.02
crystal system	orthorhombic
space group	$P2_12_12_1$ (No. 19)
unit cell parameters[a]	
a (Å)	8.8817(5)
b (Å)	10.4187(6)
c (Å)	18.1622(10)
V (Å^3)	1680.65(16)
Z	4
ρ_{calcd} (g cm^{-3})	1.308
μ (mm^{-1})	4.664
B. Data Collection and Refinement Conditions	
diffractometer	Bruker D8/APEX II CCD[b]
radiation (λ [Å])	Cu Kα (1.54178) (microfocus source)
temperature (°C)	–100
data collection 2θ limit (deg)	149.20
total data collected	23475 (-11 ≤ h ≤ 10, -12 ≤ k ≤ 12, -22 ≤ l ≤ 22)[c]
independent reflections	3381 (R_{int} = 0.0822)
number of observed reflections (*NO*)	3025 [$F_o^2 \geq 2\sigma(F_o^2)$]
structure solution method	intrinsic phasing (*SHELXT-2014*) [S4]
refinement method	full-matrix least-squares on F^2 (*SHELXL–2018*)[S4]
absorption correction method	Gaussian integration (face-indexed)
range of transmission factors	0.8419--0.6637
data/restraints/parameters	3381 / 18[d] / 182
Flack absolute structure parameter[e]	0.031(14)
final R indices[f]	
R_1 [$F_o^2 \geq 2\sigma(F_o^2)$]	0.0342
wR_2 [all data]	0.0820
largest difference peak and hole	0.272 and –0.400 e Å^{-3}

[a]Obtained from least-squares refinement of 2957 reflections with 9.74° < 2θ < 140.54°. [b]Programs for diffractometer operation, data collection, data reduction and absorption correction were those supplied by Bruker. [c]Data were collected with the detector set at three different positions. Low-angle (detector 2θ = –33º) data frames were collected using a scan time of 5 s, medium-angle (detector 2θ = 75º) frames using a scan time of 15 s, and high-angle (detector 2θ = 117º) frames using a scan time of 45 s. [d]The rigid-bond restraint (**RIGU**) was applied to the anisotropic displacement parameters of the carbon atoms of the minor component of the disordered *tert*-butyoxy group. [e]H. D. Flack, *Acta Crystallogr.*, 1983, **A39**, 876–881; H. D. Flack and G. Bernardinelli, *Acta Crystallogr.*, 1999, **A55**, 908–915; H. D. Flack and G. Bernardinelli, *J. Appl. Cryst.*, 2000, **33**, 1143–1148. The Flack parameter will refine to a value near zero if the structure is in the correct configuration and will refine to a value near one for the inverted configuration. [f]$R_1 = \Sigma||F_o| - |F_c||/\Sigma|F_o|$; $wR_2 = [\Sigma w(F_o^2 - F_c^2)^2/\Sigma w(F_o^4)]^{1/2}$.

Table S2. Crystallographic data for $ImMe_2Ge(O^tBu)_2$ (**3**), CCDC Deposition Number 2094825.

A. Crystal Data	
formula	$C_{13}H_{26}GeN_2O_2$
formula weight	314.95
crystal dimensions (mm)	0.16 × 0.14 × 0.12
crystal system	orthorhombic
space group	*Pbcn* (No. 60)
unit cell parameters[a]	
a (Å)	17.4359(6)
b (Å)	16.6515(6)
c (Å)	24.2090(8)
V (Å^3)	7028.7(4)
Z	16
ρ_{calcd} (g cm^{-3})	1.191
μ (mm^{-1})	2.351
B. Data Collection and Refinement Conditions	
diffractometer	Bruker D8/APEX II CCD[b]
radiation (λ [Å])	Cu Kα (1.54178) (microfocus source)
temperature (°C)	–100
data collection 2θ limit (deg)	140.32
total data collected	70160 (-21 ≤ *h* ≤ 21, -18 ≤ *k* ≤ 20, -29 ≤ *l* ≤ 29)
independent reflections	6690 (R_{int} = 0.0593)
number of observed reflections (*NO*)	5102 [$F_o^2 \geq 2\sigma(F_o^2)$]
structure solution method	intrinsic phasing (*SHELXT-2014*[c])
refinement method	full-matrix least-squares on F^2 (*SHELXL–2018*[d])
absorption correction method	Gaussian integration (face-indexed)
range of transmission factors	0.8921–0.7163
data/restraints/parameters	6690 / 0 / 329
final *R* indices[e]	
$R1$ [$F_o^2 \geq 2\sigma(F_o^2)$]	0.0358
$wR2$ [all data]	0.0992
largest difference peak and hole	0.388 and –0.352 e Å^{-3}

[a]Obtained from least-squares refinement of 9877 reflections with 7.34° < 2θ < 139.64°.
[b]Programs for diffractometer operation, data collection, data reduction and absorption correction were those supplied by Bruker. [c]G. M. Sheldrick, *Acta Crystallogr.*, 2015, **A71**, 3–8. (*SHELXT-2014*). [d]G. M. Sheldrick, *Acta Crystallogr.*, 2015, **C71**, 3–8. (*SHELXL-2018/3*). [e]$R1 = \Sigma||F_o| - |F_c||/\Sigma|F_o|$; $wR2 = [\Sigma w(F_o^2 - F_c^2)^2/\Sigma w(F_o^4)]^{1/2}$.

4. Characterization of the products from the reaction of [Ge(O^{t}Bu)$_2$] (1) with hydride sources

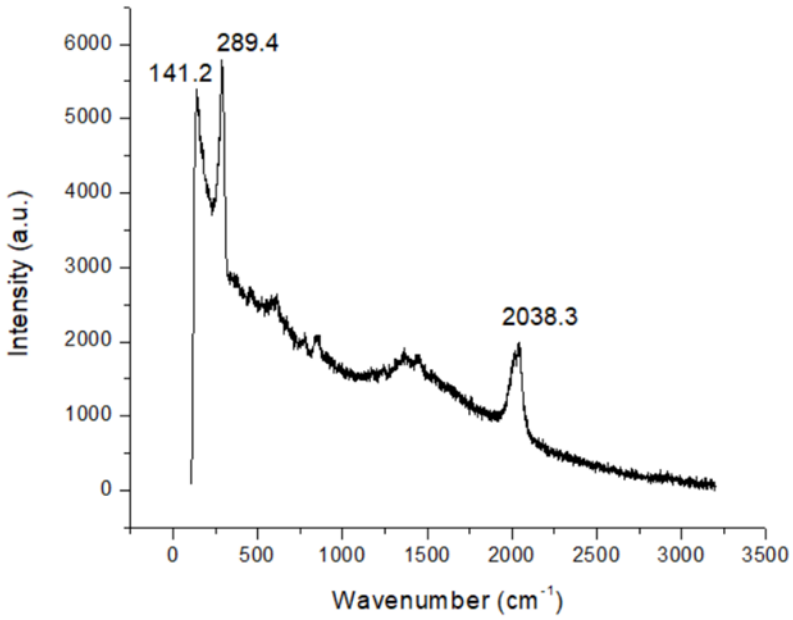

Fig. S34. Raman spectrum of the germanium hydride precipitate **(2a)** formed from [Ge(O^{t}Bu)$_2$] (**1**) and 3 equiv. of HBpin at room temperature; Ge-Ge and Ge-H stretches are present at 289 and 2039 cm^{-1}. Excitation wavelength: 785 nm.

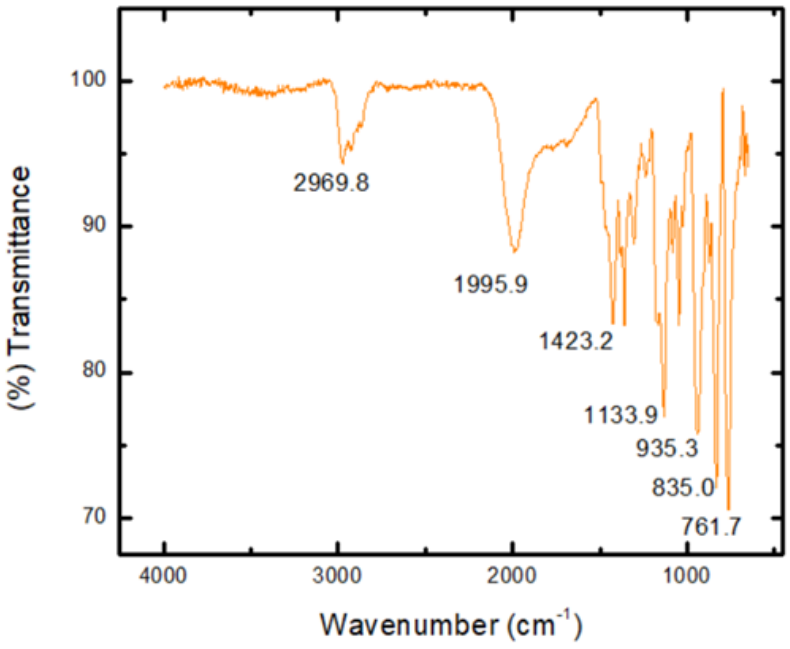

Fig. S35. FT-IR spectrum of the [GeH$_{1.64}$(O^{t}Bu)$_{0.36}$]$_n$ (**2a**) precipitate formed from [Ge(O^{t}Bu)$_2$] (**1**) and 3 equiv. of HBpin at room temperature; a strong Ge-H stretch is observed at 1996 cm^{-1}.[S14]

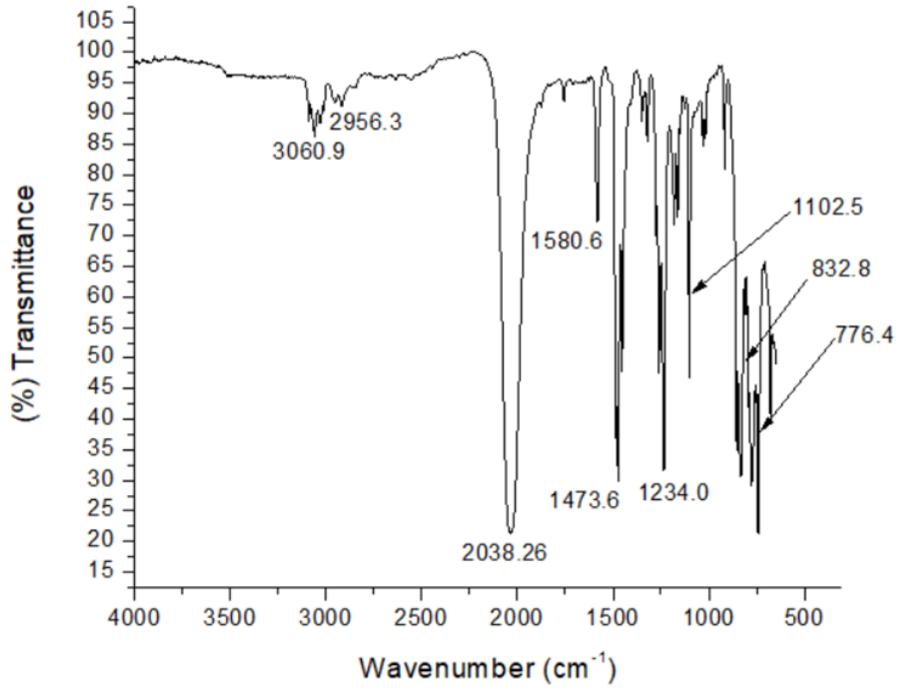

Fig. S36. FT-IR of the germanium hydride precipitate (**2b**) formed from [Ge(O^{t}Bu)$_2$] (**1**) and 2.2 equivalents of HBcat at room temperature; a strong Ge-H stretch is observed at 2038 cm $^{-1}$.[S14]

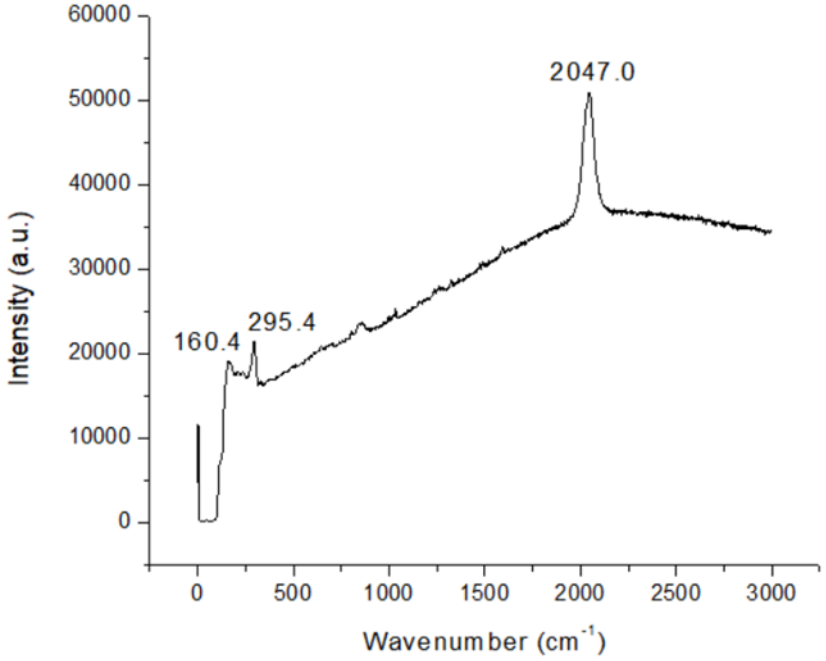

Fig. S37. Raman spectrum of the germanium hydride precipitate (**2b**) formed from [Ge(O^{t}Bu)$_2$] (**1**) and 2.2 equivalents of HBcat at room temperature; Ge-Ge and Ge-H stretches are seen at 295 and 2047 cm^{-1}.[S1, S13] Excitation wavelength: 600 nm.

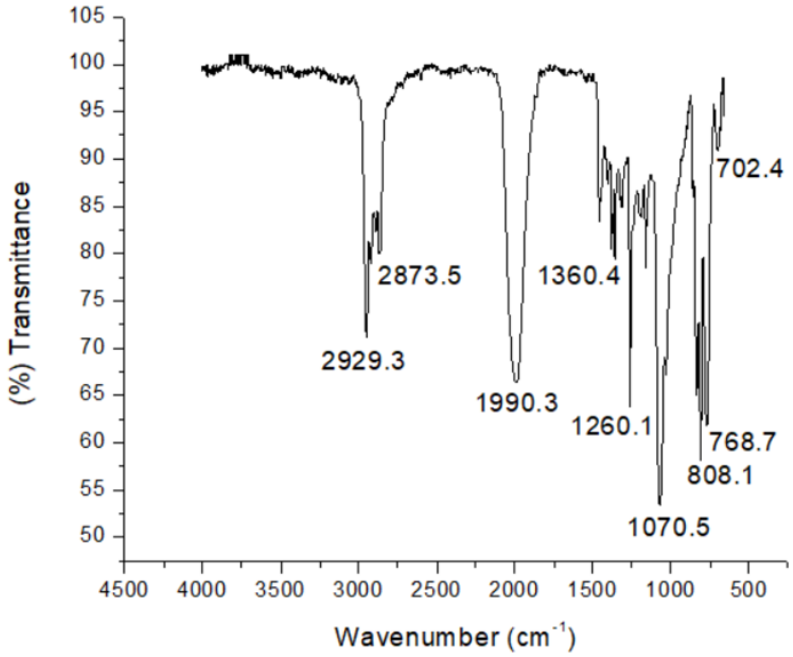

Fig. S38. FT-IR spectrum of the germanium hydride precipitate formed from [Ge(O^{t}Bu)$_2$] (**1**) and 2.2 equivalents of DIBAL-H at 70 °C for 16 hrs; a strong Ge-H stretch is observed at 1990 cm^{-1}.[S14]

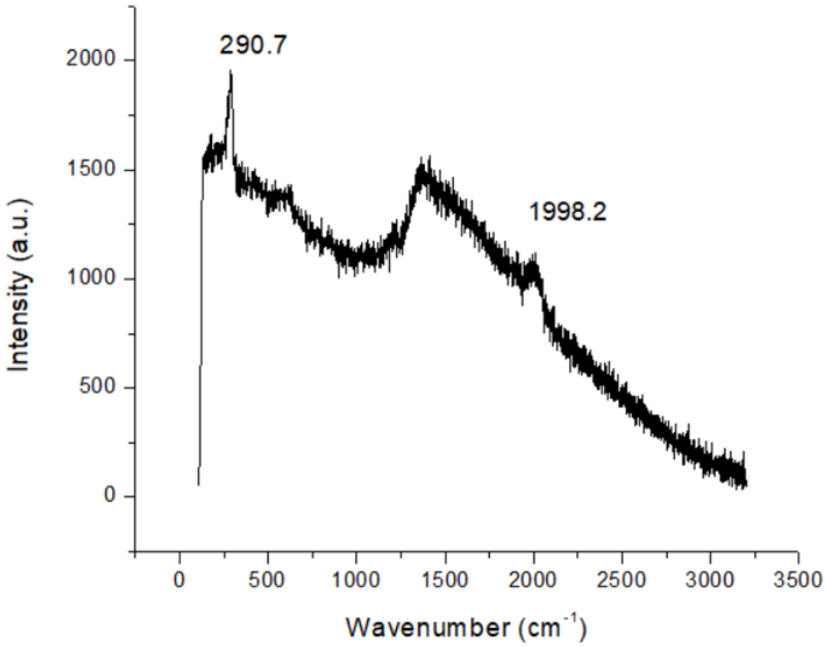

Fig. S39. Raman spectrum of the germanium hydride precipitate formed from [Ge(O^{t}Bu)$_2$] (**1**) and 2.2 equiv. of DIBAL-H at 70 °C for 16 hrs. Excitation wavelength: 785 nm.[S1, S13]

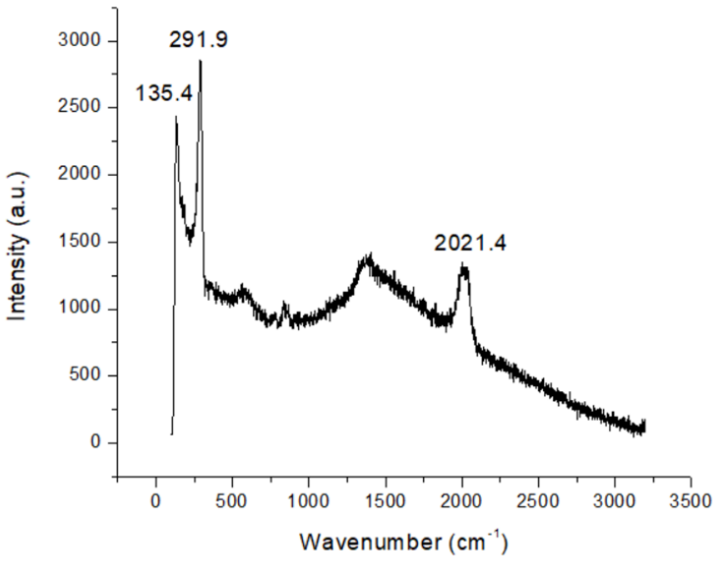

Fig. S40. Raman spectrum of the $[GeH_{1.92}(O^tBu)_{0.08}]_n$ (**2c**) precipitate formed from $[Ge(O^tBu)_2]$ (**1**) and 10 equiv. of HBpin at 70 °C for 16 h; Ge-Ge and Ge-H stretches are found at 292 and 2021 cm^{-1}, respectively. Excitation wavelength: 785 nm.[S1, 13]

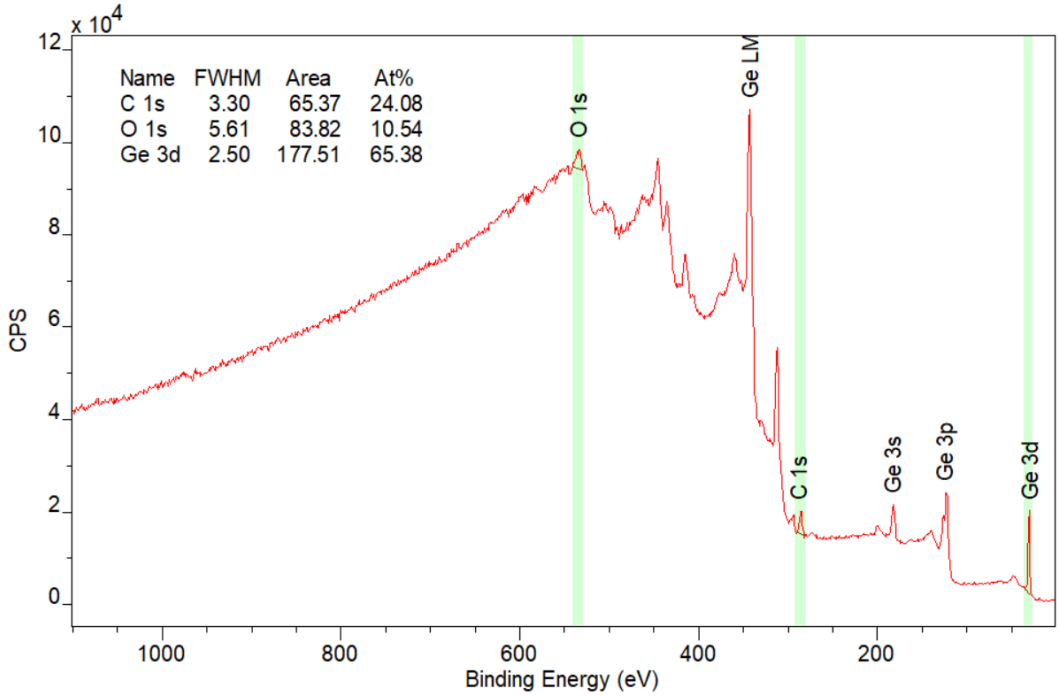

Fig. S41. Survey XP spectrum of **2c**, referenced to adventitious C 1s (284.8 eV). A strong shoulder next to the Ge 3s peak would be expected if B is present - B 1s energy (Binding energy = 188 eV) overlaps with the edge of the Ge 3s peak (BE = 181 eV). No prominent shoulder is noted, indicating low to no boron incorporation.

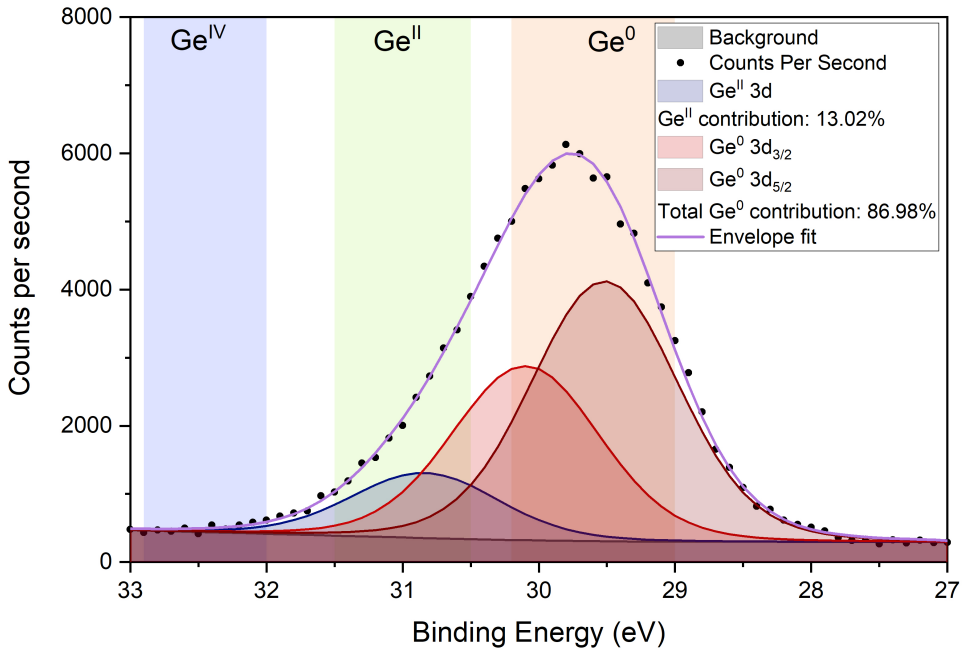

Fig. S42. High resolution XP spectrum of the Ge 3d region.

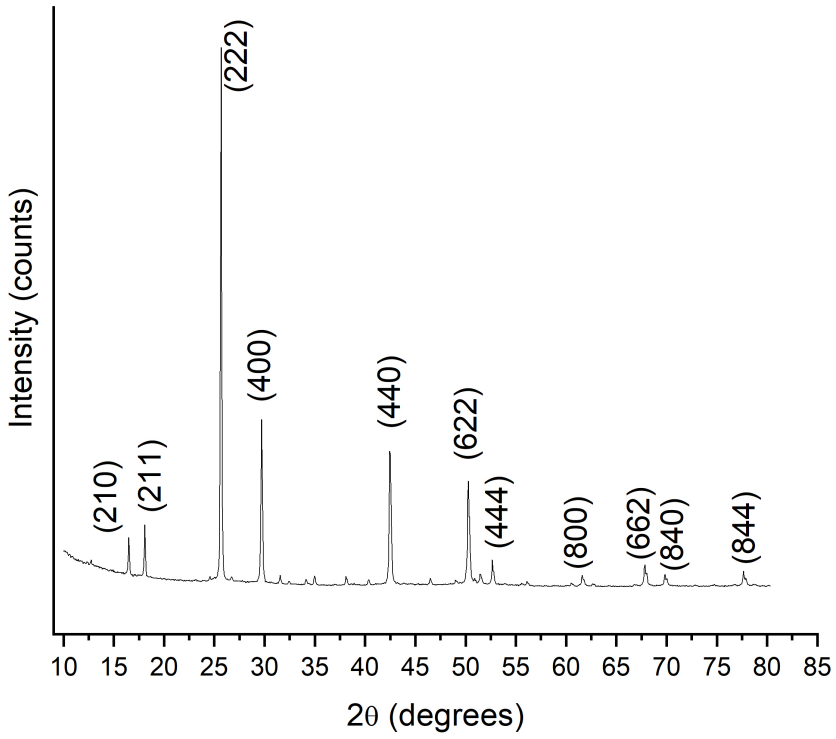

Fig. S43. pXRD of the GeI_4 isolated from the reaction of **2c** with excess I_2. Reflections are indexed to the literature.[S15]

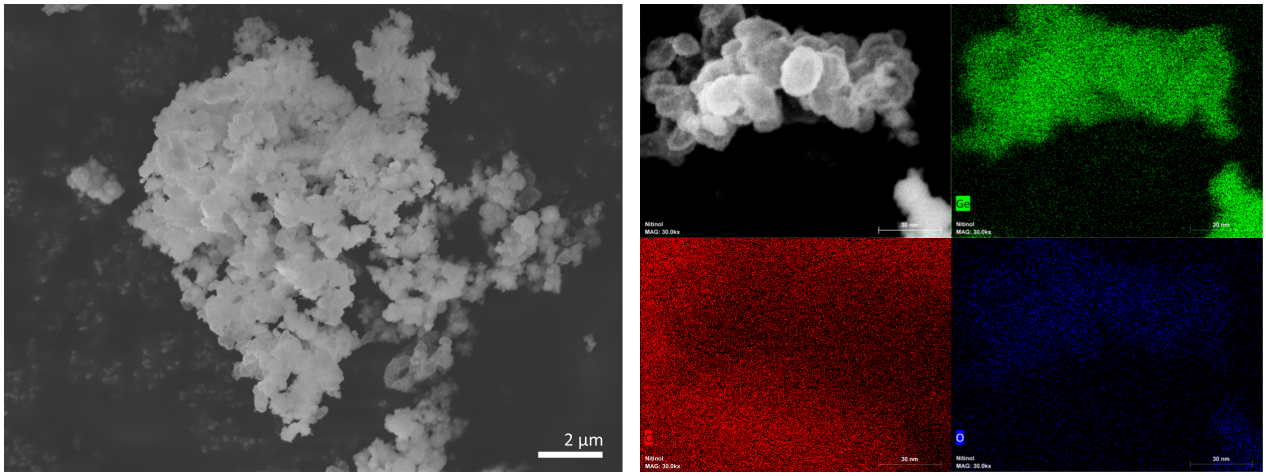

Fig. S44. SEM secondary electron capture of **2c** deposited on carbon tape (left) and EDX mapping of the same (right: Ge – green, C – red, O – blue). Collected at 10 kV.

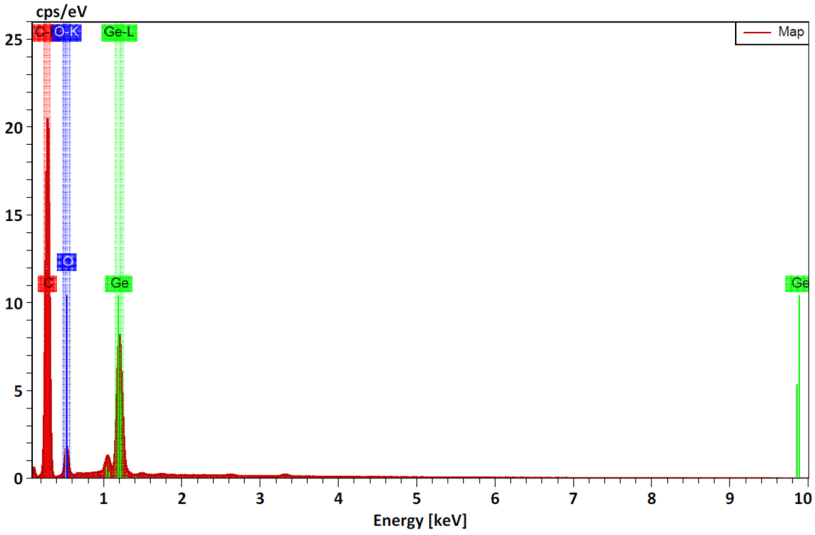

Element	Line	Mass %	Norm. Mass%	Atom %	Abs. Error (%), σ
Carbon	K-Series	71.8	68.9	87.5	7.8
Germanium	L-Series	24.1	23.1	4.9	1.3
Oxygen	K-Series	8.4	8.0	7.7	1.1

Fig. S45. EDX summary for the element mapping shown in Fig. S44, above.

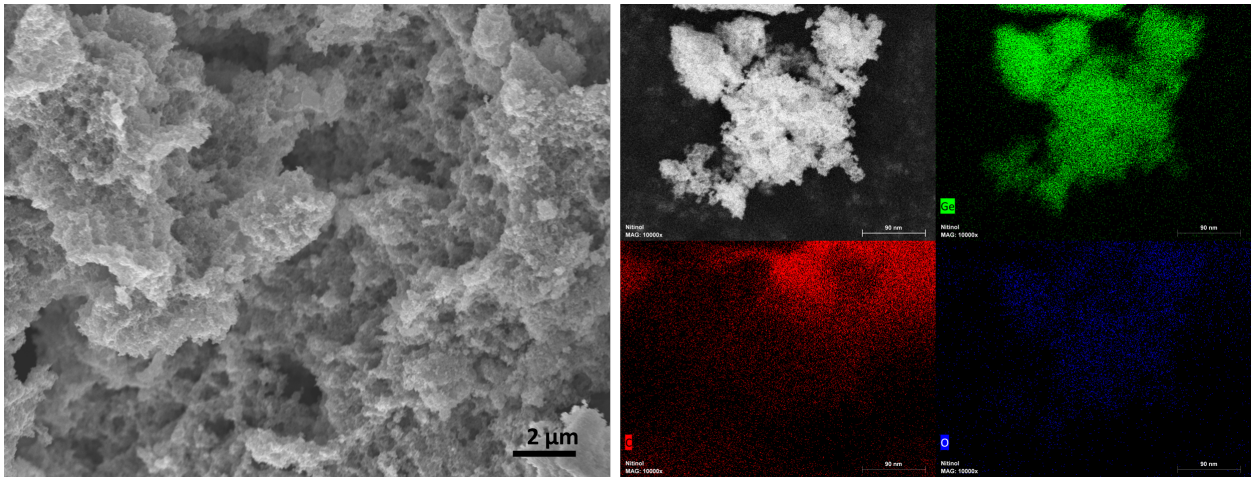

Fig. S46. SEM secondary electron capture of **2c**, heated to 200 °C for two hours under N_2 and deposited on carbon tape (left) and EDX mapping of the same (right: Ge – green, C – red, O – blue). Collected at 10 kV.

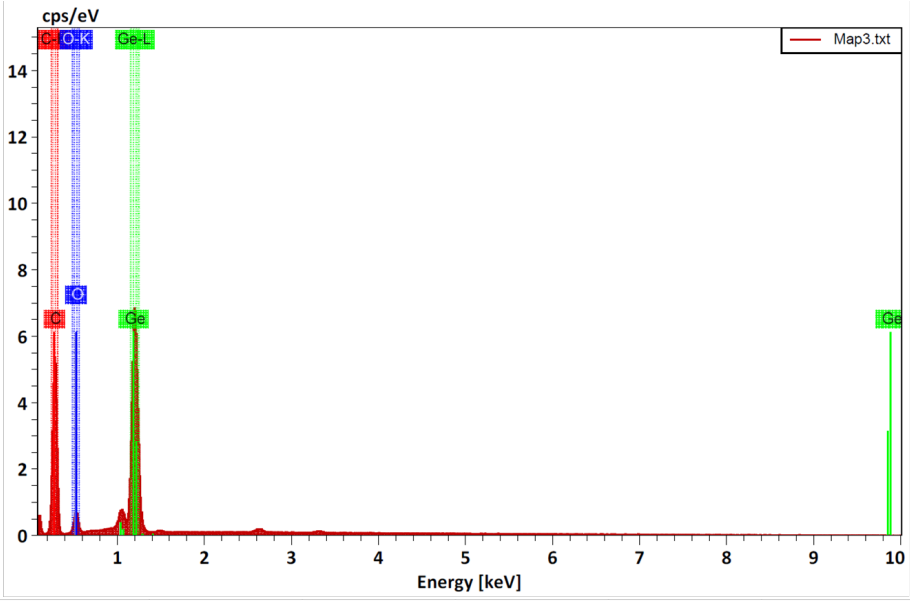

Element	Line	Mass %	Norm. Mass%	Atom %	Abs. Error (%), σ
Carbon	K-Series	49.5	52.7	82.4	5.7
Germanium	L-Series	38.9	41.4	10.7	2.1
Oxygen	K-Series	5.5	5.9	6.9	0.8

Fig. S47. EDX summary for the element mapping shown in Fig. S46, above.

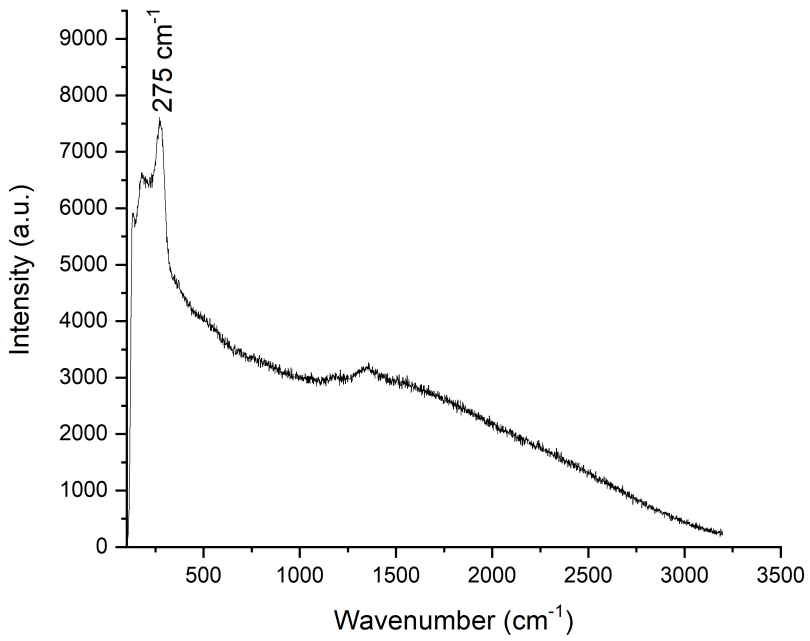

Fig. S48. Raman spectroscopy of **2c**, after undergoing annealing at 200 °C under N_2 for 2 hours. The Ge-Ge stretching frequency at ~280 cm^{-1} is retained from the starting material (in **Fig. S40**), but the Ge-H resonance is lost.

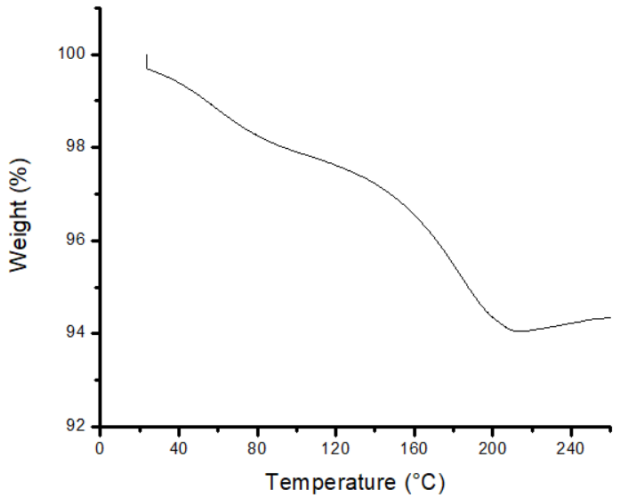

Fig. S49. Thermogravimetric analysis (TGA) plot of the $[GeH_{1.92}(O^tBu)_{0.08}]_n$ (**2c**) precipitate formed from $[Ge(O^tBu)_2]$ (**1**) and 10 equiv. of HBpin at 70 °C for 16 h. Scan rate = 10 °C/min under Ar.

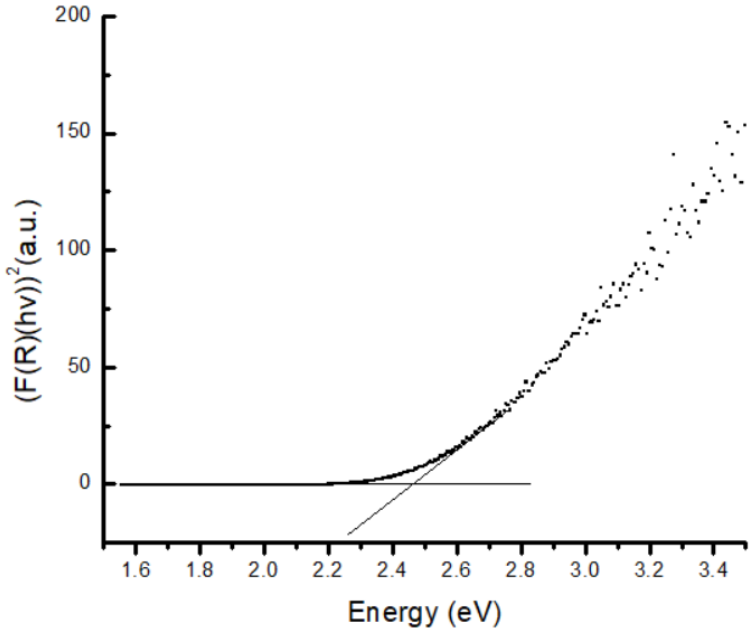

Fig. S50. Diffuse reflectance analysis of $[GeH_{1.92}(O^tBu)_{0.08}]_n$ (**2c**). Line fitting indicates a band gap of 2.50 eV.[S15]

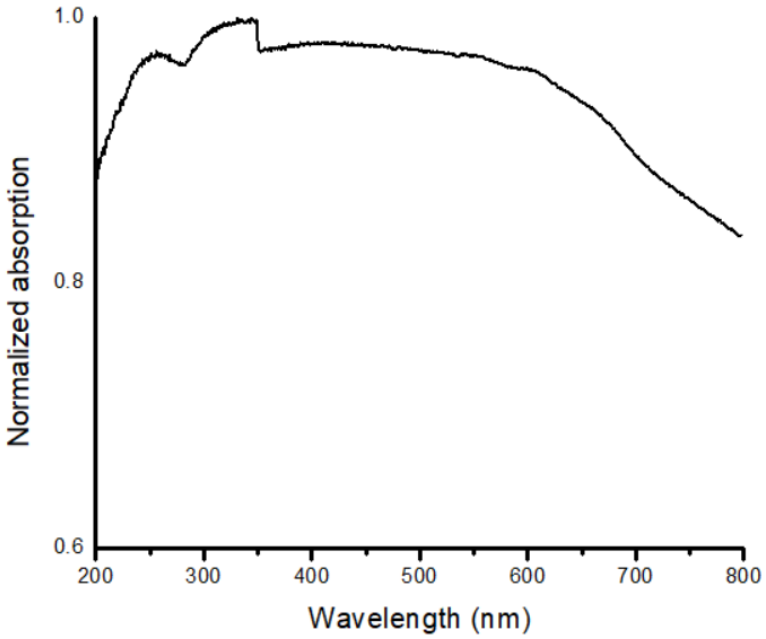

Fig. S51. UV-Vis spectrum of $[GeH_{1.92}(O^tBu)_{0.08}]_n$ (**2c**) heated for 2 hrs at 200 °C.

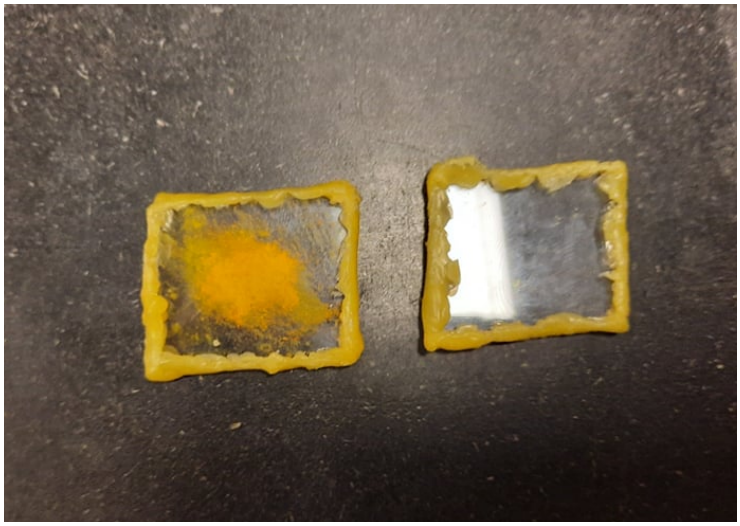

Fig. S52. Photograph of the air-sensitive system (Candelilla wax-sealed plates) employed for the diffuse reflectance absorption (DRA) experiment involving **2c** (the yellow-orange powder at the right).

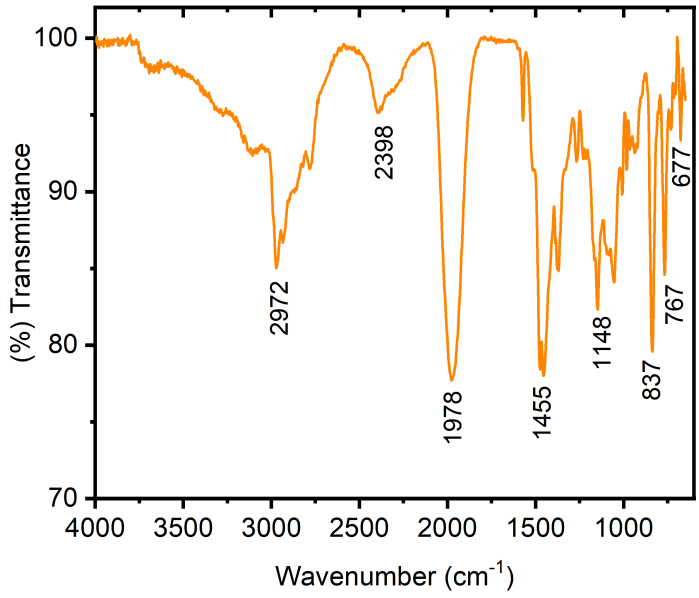

Fig. S53. Infrared Spectrum of precipitate from 10:1 HBpin:$ImMe_2$•$Ge(O^tBu)_2$ reaction after heating in benzene at 70 °C for 16 hrs. Strong Ge-H stretching at 1978 cm^{-1}.[S14]

5. Ge Thin Film Characterization

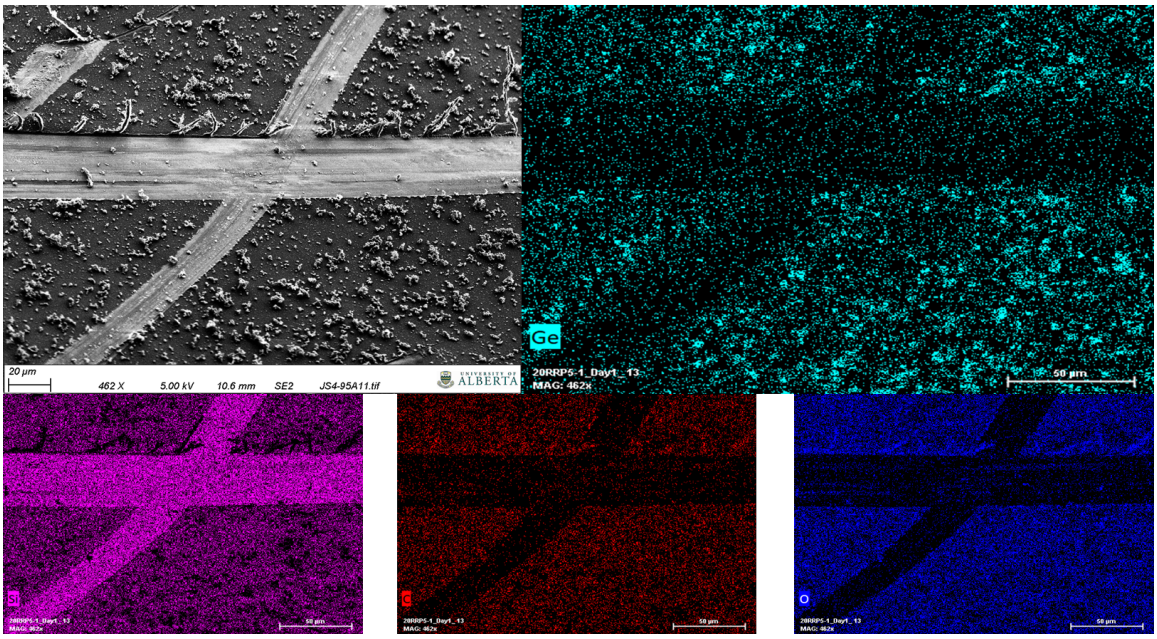

Fig. S54. SEM backscatter electron image and EDX element mapping for the Ge film deposited on a Si wafer from combining five equivalents of $H_3B{\bullet}SMe_2$ (2.0 M solution in THF) with a 0.021 M solution of $[Ge(O^tBu)_2]$ (**1**) (1.5 mL) (heated to 70 °C for 3 hrs), producing 112 ± 13 nm thick layers of Ge. SEM collected at 5 kV. The solution of $[Ge(O^tBu)_2]$ (**1**) was deemed to be too concentrated to produce consistent layers of Ge.

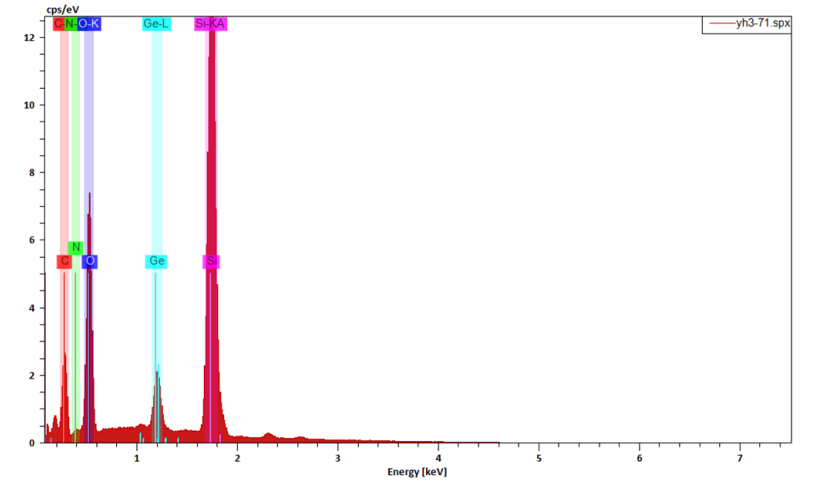

Element	Line	Mass%	Norm Mass%	Atom%	Abs Error (%), σ
Silicon	K-Series	83	66.6	53.5	3.9
Oxygen	K-Series	22.6	18.2	25.6	2.6
Carbon	K-Series	12.1	9.7	18.2	1.5
Germanium	L-Series	5.9	4.7	1.5	0.3
Nitrogen	K-Series	0.9	0.8	1.2	0.2

Fig. S55. Energy dispersive X-ray (EDX) spectrum for the element mapping shown in Fig. S54, above.

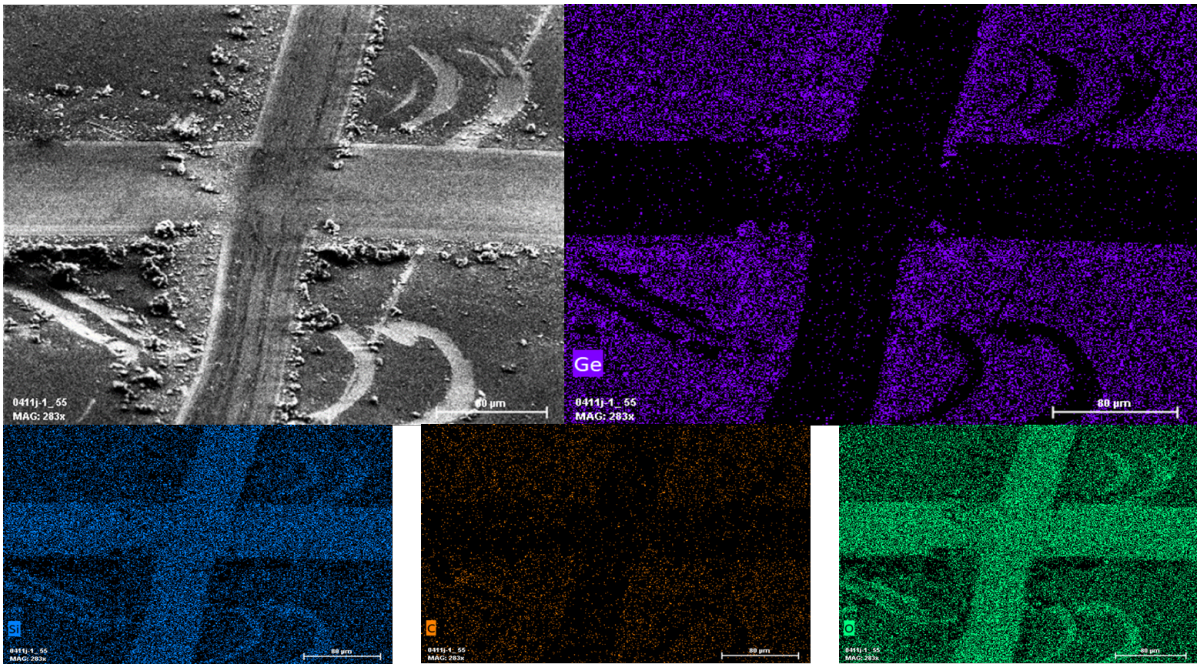

Fig. S56. SEM backscatter electron image and EDX element mapping for the Ge film deposited on a Si wafer from combining three equivalents of $H_3B{\bullet}SMe_2$ (2.0 M solution in THF) with a 0.014 M solution of $[Ge(O^tBu)_2]$ (**1**) in 1.5 mL of toluene (heated to 70 °C for 1 hr), producing 33 ± 5 nm thick layers of Ge. SEM collected at 5 kV.

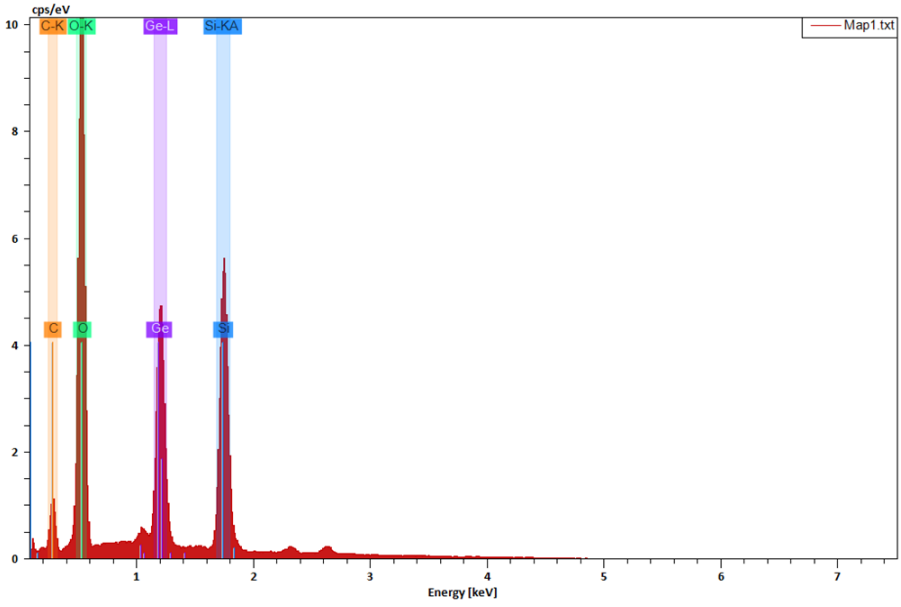

Element	Line	Mass%	Norm Mass%	Atom%	Abs Error (%), σ
Silicon	K-Series	47.2	39.3	32.2	3.9
Oxygen	K-Series	44.2	36.8	53	2.6
Carbon	K-Series	5.4	8.7	0.8	0.8
Germanium	L-Series	23.3	19.4	6.1	1.5

Fig. S57. EDX summary for the element mapping shown in Fig. S56, above.

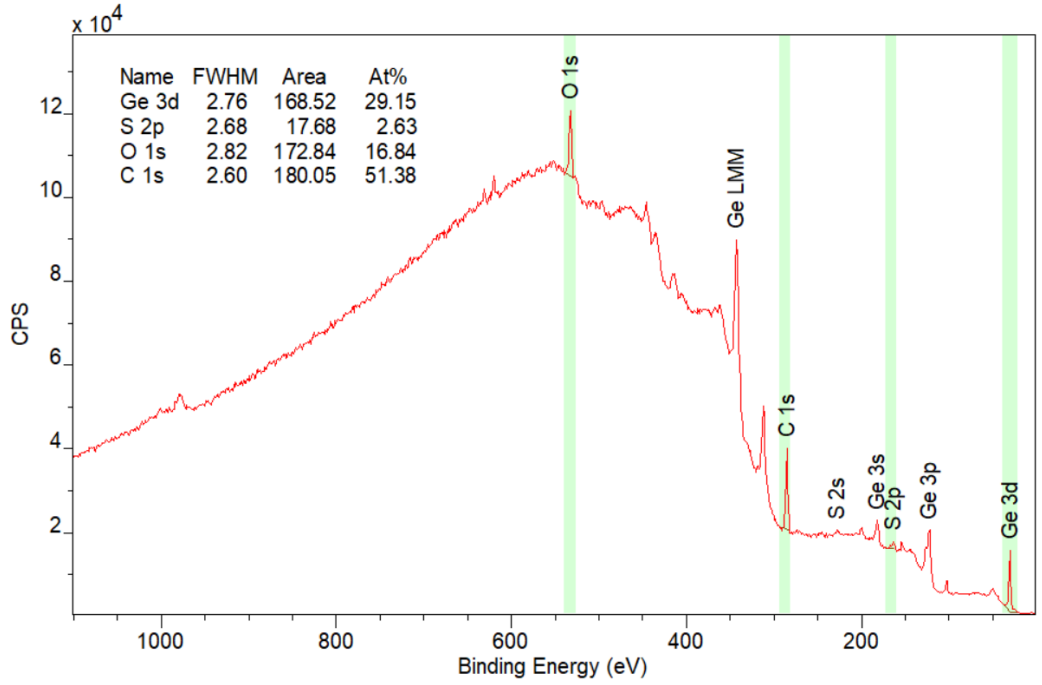

Fig. S58. Survey XP spectrum of precipitate collected from the reaction described in Fig. S56, referenced to adventitious C 1s (284.8 eV). A small quantity of sulfur is detected.

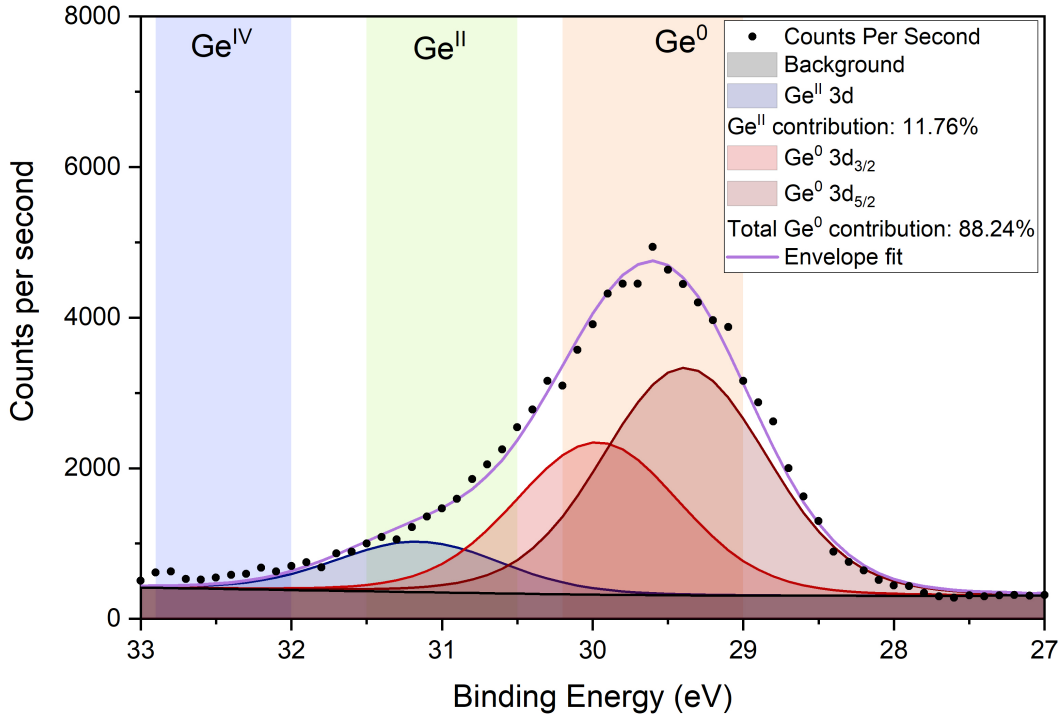

Fig. S59. High resolution XP spectrum of the Ge 3d region of precipitate collected from the reaction described in Fig. S56,

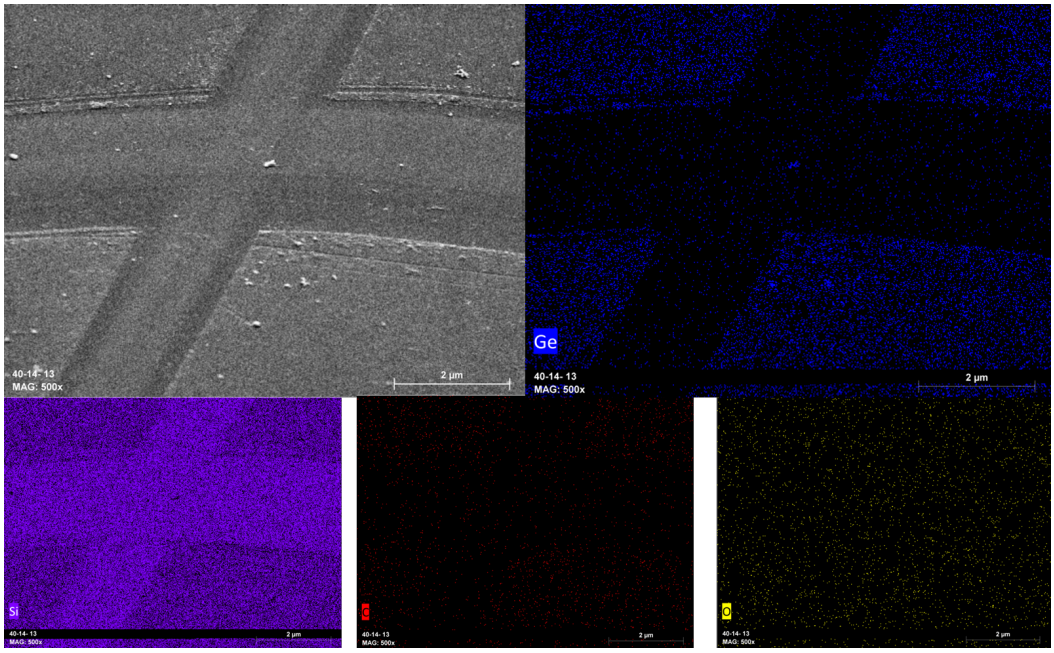

Fig. S60. SEM backscatter electron image and EDX element mapping for the Ge film deposited on a Si wafer from combining three equivalents of $H_3B{\bullet}SMe_2$ (2.0 M solution in THF) with a 0.014 M solution of [Ge(O^{t}Bu)$_2$] (**1**) in 1.5 mL of toluene (heated to 70 °C for 3 hrs), producing 62 ± 18 nm thick layers of Ge. Data collected at 5 kV.

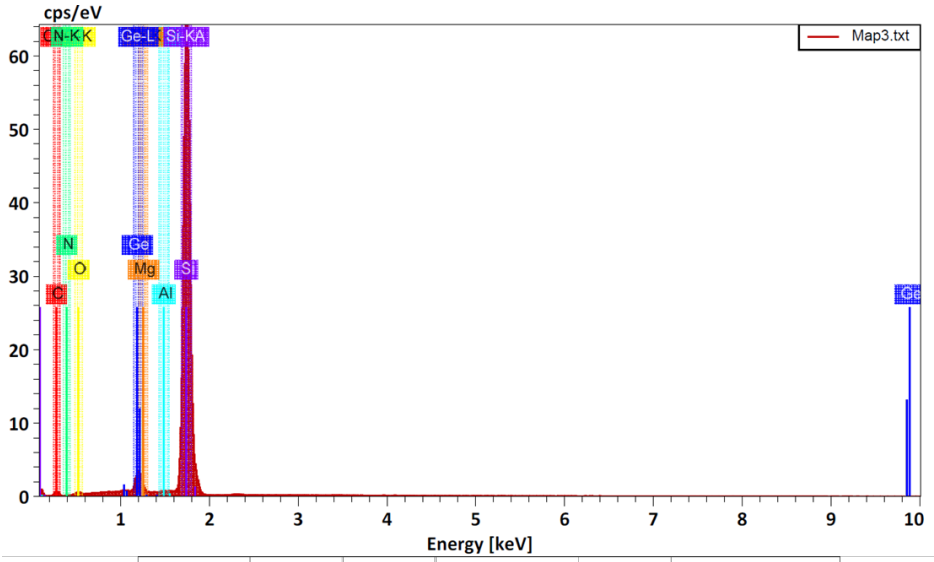

Element	Line	Mass%	Norm Mass%	Atom%	Abs Error (%), σ
Silicon	K-Series	123.5	89.6	84	5
Oxygen	K-Series	1.1	0.8	1.3	0.3
Carbon	K-Series	8.1	5.8	12.8	1.5
Germanium	L-Series	4.5	3.3	1.2	0.3
Nitrogen	K-Series	0.2	0.2	0.3	0.1

Fig. S61. EDX summary for the element mapping shown in Fig. S60, above.

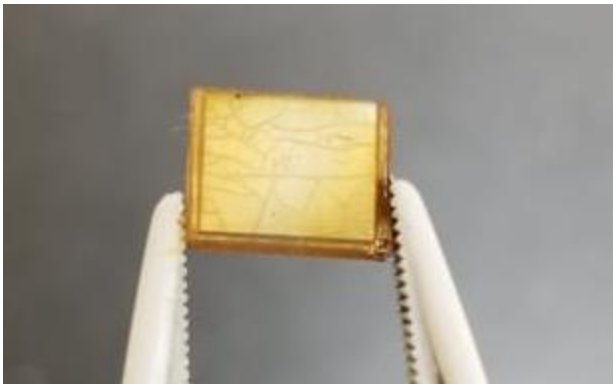

Fig. S62. Photograph of a golden-colored Ge thin film deposited on a polyethylene terephthalate (PET) substrate (0.7 × 0.8 mm, initially transparent and colorless). Deposition conditions: three equivalents of $H_3B{\bullet}SMe_2$ (2.0 M solution in THF) were combined with a 0.014 M solution of $[Ge(O^tBu)_2]$ (**1**) in 1.5 mL of toluene with heating to 70 °C for 1 hr.

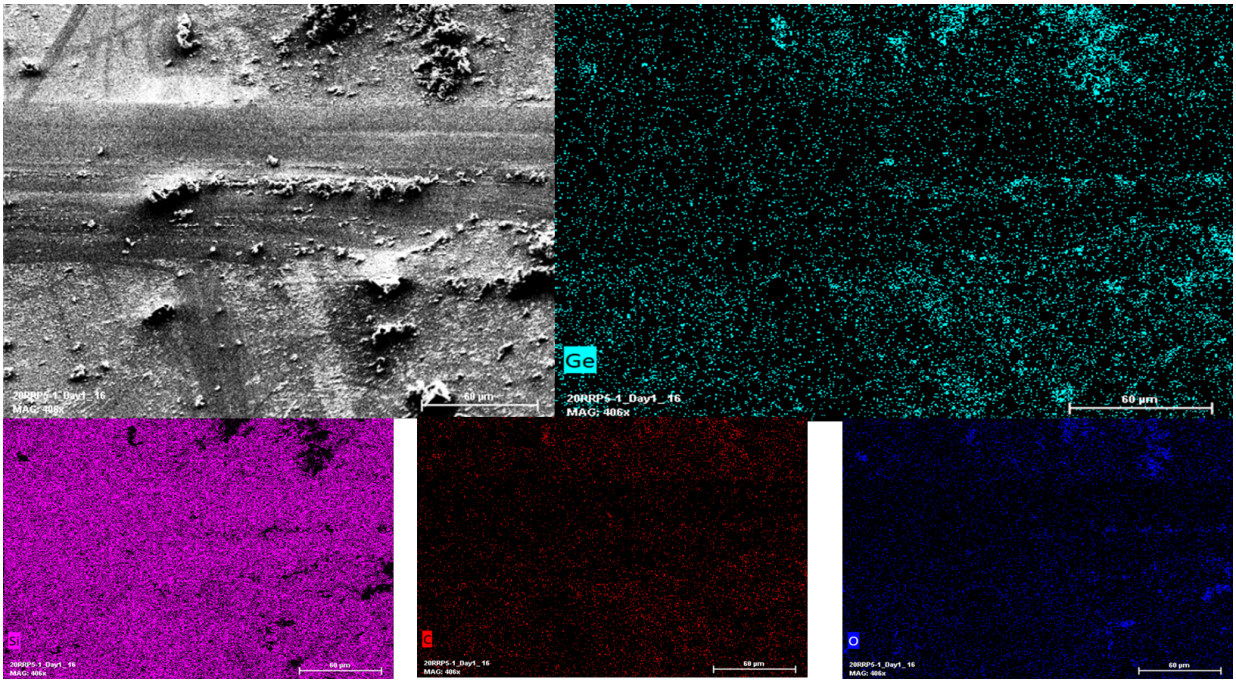

Fig. S63. SEM backscatter electron image and EDX element mapping for the Ge film deposited from combining three equivalents of $H_3B{\bullet}SMe_2$ (2.0 M solution in THF) with a 0.021 M solution of $Ge(OMes^*)_2$ in 1.5 mL of toluene, producing inconsistent surface coverage. Data collected at 5 kV.

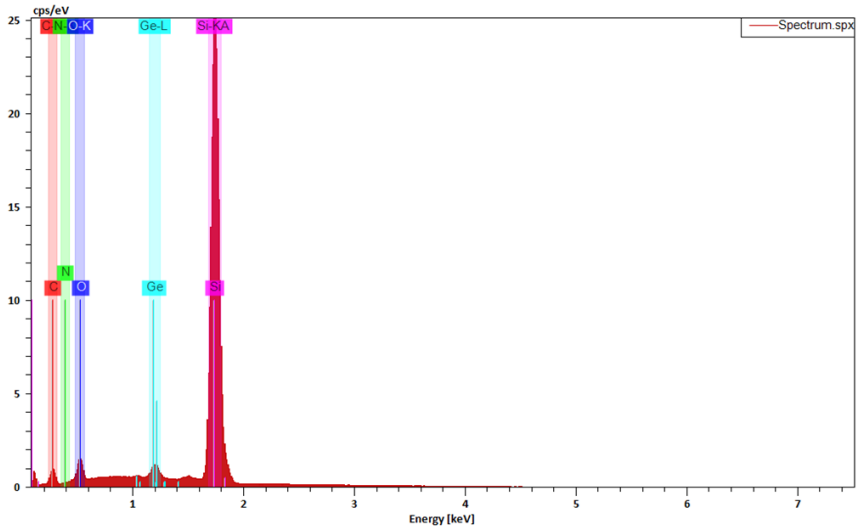

Element	Line	Mass%	Norm Mass%	Atom%	Abs Error (%), σ
Silicon	K-Series	143.8	92.6	87.8	6.7
Oxygen	K-Series	4.0	2.6	4.3	0.6
Carbon	K-Series	5.1	3.3	7.3	0.8
Germanium	L-Series	2.3	1.5	0.5	0.1
Nitrogen	K-Series	0.0	0.0	0.0	0.0

Fig. S64. EDX summary for the element mapping shown Fig. S63, above.

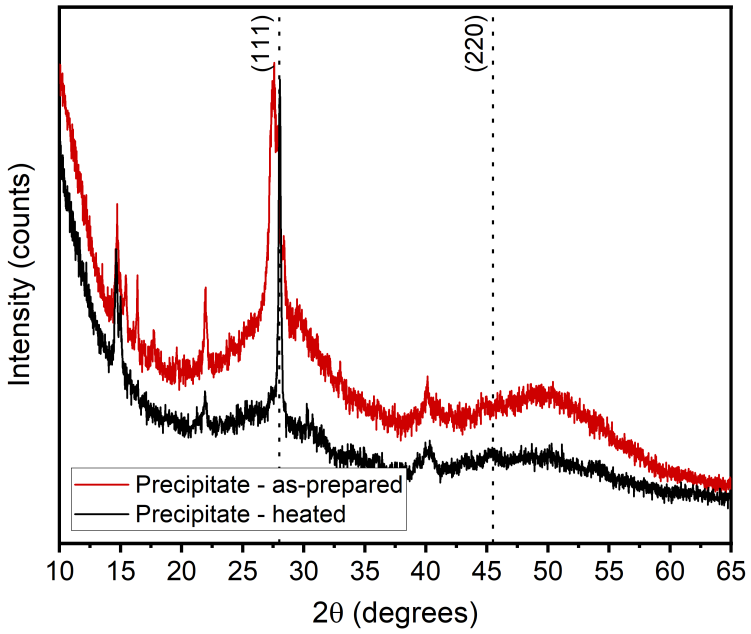

Fig. S65. Powder XRD of the deposited Ge precipitate (same conditions as described for Fig. S48) and the same precipitate after being heated for 2 hrs at 200 °C under N_2 to yield semi-crystalline Ge (black).

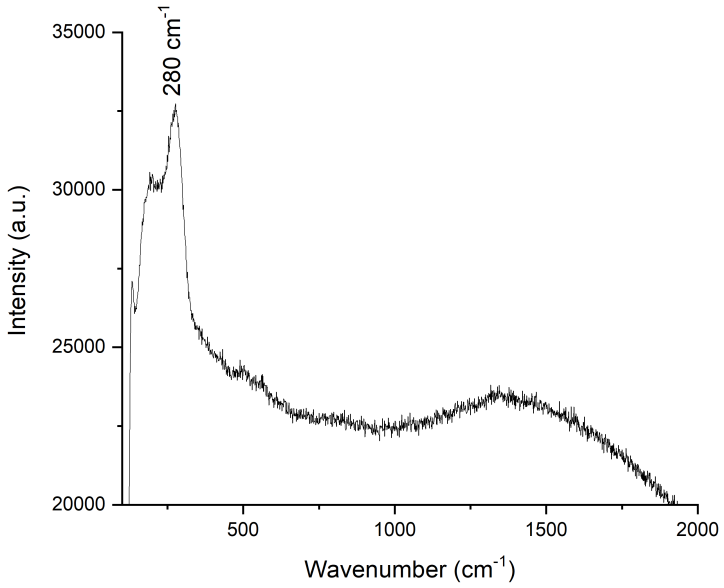

Fig. S66. Raman spectroscopy of the deposited Ge precipitate (same conditions as described for Fig. S48) showing the amorphous Ge-Ge stretching frequency at 280 cm^{-1}.

6. Computational details

General Methods

Computations were performed with the Gaussian16[S17] software. For the computational determination of reaction coordinates for the reaction of $Ge(O^tBu)_2$ with HBpin and for relative energies of the $ImMe_2$•$Ge(OR)_2$ analogues geometry optimizations, using default convergence criteria, were performed using density functional theory (DFT) with the M06-2X functional[S18] and the cc-pVTZ basis set[S18] was used. Harmonic vibrational analyses were performed at the same level of theory for all optimized stationary points to determine their character (minimum or first-order saddle point) and to acquire the thermochemical data (at 298.15 K).

In keeping with recent computational studies of long-chain Ge species,[S19] the geometry optimizations of the oligomerized isomers of $[GeH_2]_n$ (n = 1-5) and the linear H-$(GeH_2)_{10}$-H and branched H-$[Ge(H)(GeH_3)]_5$-H isomers were performed using density functional theory (DFT) with the PBE functional,[S21] the cc-pVTZ basis set,[S19] and an empirical dispersion correction GD3BJ.[S22] Harmonic vibrational analyses were performed at the same level of theory for all optimized stationary points to determine their character (minimum or first-order saddle point) and to acquire the thermochemical data (at 298.15 K).

Time-dependent density function theory (TD-DFT) computations were carried out on the linear H-$(GeH_2)_{10}$-H and branched H-$[Ge(H)(GeH_3)]_5$-H isomers using the B3LYP functional[S23] and the cc-pVTZ basis set,[S19] with five triplet and 5 singlet excitations resolved. IR and Raman frequency calculations were carried out using density functional theory (DFT) with the B3LYP[S23] functional and cc-pVDZ basis set. [S19]

All input (.gjf) and output (.log and .fchk, where applicable) are available online at: 10.6084/m9.figshare.15132588

Table S3. Relative energies and HOMO/LUMO level tabulations for computed isomers of $[GeH_2]_n$, n = 1-5 (PBE0/cc-pVTZ). See Figs. S89-S93 for ball and stick models of optimized geometries.

Formula	Free energy relative to chain conformer (kJ mol^{-1})	HOMO (eV)	LUMO (eV)	HOMO/LUMO gap (eV)
n = 1				
GeH_2 (singlet)	0	-6.91	-3.07	3.84
n = 2				
$H_2Ge{=}GeH_2$ planar	0	-5.82	-1.73	4.09
$H_2Ge{=}GeH_2$ *trans*-bent	-10.89	-6.20	-2.46	3.73
$HGe\text{-}GeH_3$	-11.17	-6.65	-3.30	3.34
n=3				
$[GeH_2]_3$ chain	0.00	-5.90	-2.23	3.68
$[GeH_2]_3$ ring	-55.09	-6.74	-0.39	6.34
$H_3Ge\text{-}GeH_2\text{-}GeH$ *	-35.50	-6.30	1.54	7.84
n=4				
$[GeH_2]_4$ chain	0.00	-5.71	-2.86	2.85
$[GeH_2]_4$ ring	-196.74	-7.29	-0.69	6.60
$H_2Ge{=}Ge(GeH_3)_2$ *trans bent*	-93.70	-6.66	-3.27	3.38
$H_3GeGe(H){=}Ge(H)GeH_3$ *cis*	-80.50	-5.76	-1.91	3.84
$H_3GeGe(H){=}Ge(H)GeH_3$ *trans*	-90.30	-6.04	-2.46	3.58
$H_3Ge\text{-}(GeH_2)_2\text{-}GeH$ *	-97.75	-6.18	-2.06	4.13
$H_3Ge\text{-}Ge\text{-}GeH_2\text{-}GeH_3$ *	-99.10	-6.37	1.70	8.07
$H_3Ge(H)Ge[cyclo\text{-}GeH_2\text{-}GeH_2]$	-119.80	-6.59	-0.68	5.92
n=5				
$[GeH_2]_5$ chain	0.00	-5.35	-3.62	1.73
$[GeH_2]_5$ ring	-284.49	-7.47	-0.66	6.81
$H_3Ge\text{-}GeH_2\text{-}Ge(GeH_3){=}GeH_2$	-135.81	-6.06	-2.56	3.50
$H_2Ge{=}GeH\text{-}GeH(GeH_3)_2$	-128.10	-6.10	-2.54	3.56
$H_3Ge\text{-}GeH{=}Ge(GeH_3)_2$	-140.39	-6.01	-2.47	3.54
$H_3Ge\text{-}(GeH_2)_3\text{-}GeH$	-136.43	-6.18	-1.57	4.61
$[cyclo\text{-}GeH(GeH_3)GeH_2\text{-}GeH(GeH)_3]$	-167.10	-6.53	-0.84	5.69
$[cyclo\text{-}GeH_2GeH_2GeH_2\text{-}GeH(GeH_3)]$	-243.92	-7.25	-0.82	6.43

* Indicates bridging H in optimized structures,

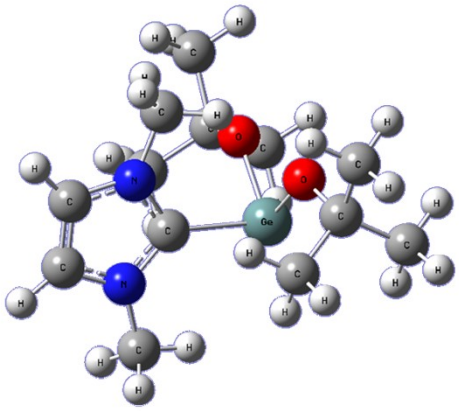

Fig. S67. Optimized structure of $ImMe_2$•$Ge(O^tBu)_2$ (**3**). Geometry determined at the M06-2X/cc-pVDZ level of theory.

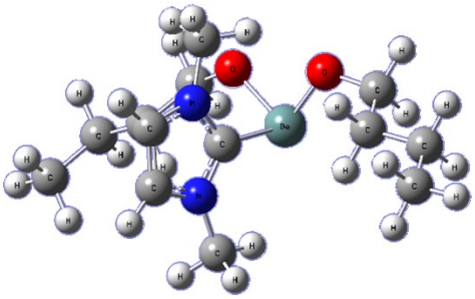

Fig. S68. Optimized structure of $ImMe_2$•$Ge(O^nBu)_2$. Geometry determined at the M06-2X/cc-pVDZ level of theory.

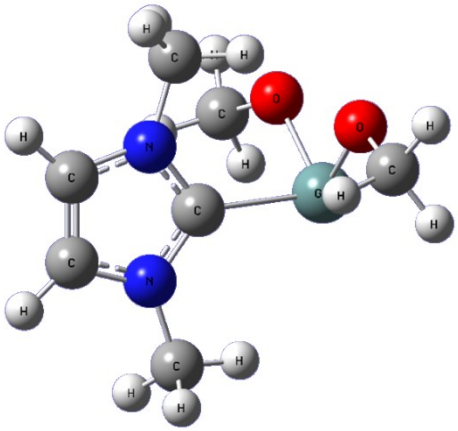

Fig. S69. Optimized structure of $ImMe_2$•$Ge(OMe)_2$. Geometry determined at the M06-2X/cc-pVDZ level of theory.

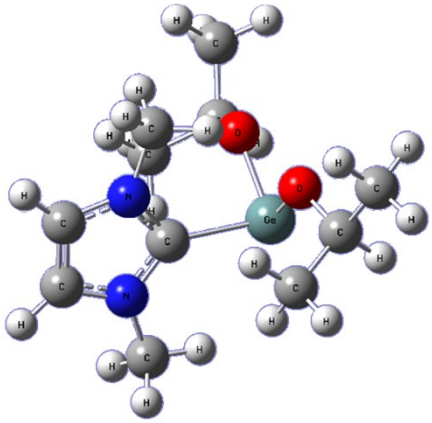

Fig. S70. Optimized structure of $ImMe_2$•$Ge(O^iPr)_2$. Geometry determined at the M06-2X/cc-pVDZ level of theory.

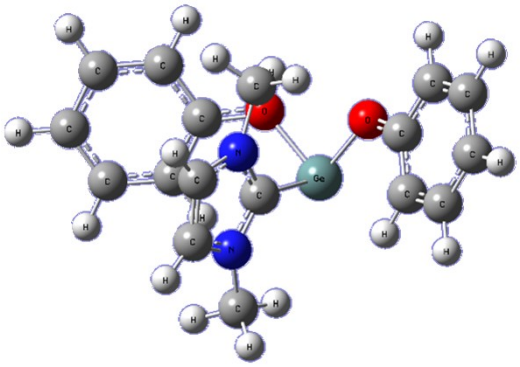

Fig. S71. Optimized structure of $ImMe_2$•$Ge(OPh)_2$. Geometry determined at the M06-2X/cc-pVDZ level of theory.

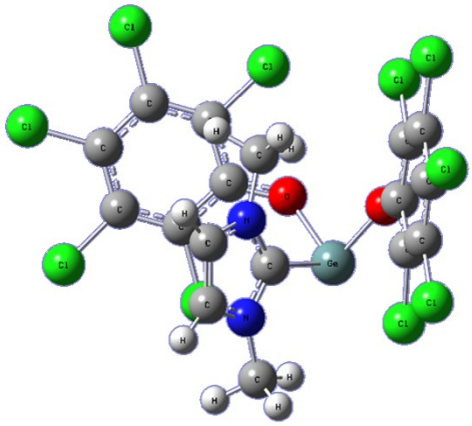

Fig. S72. Optimized structure of $ImMe_2$•$Ge(OC_6Cl_5)_2$. Geometry determined at the M06-2X/cc-pVDZ level of theory.

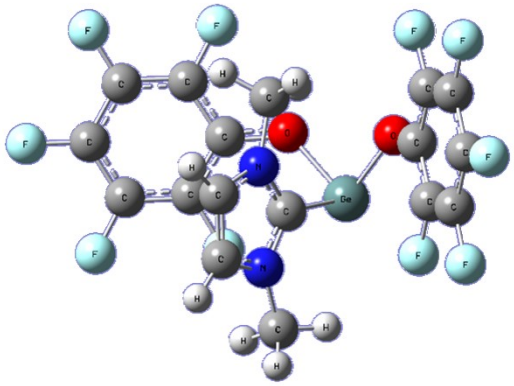

Fig. S73. Optimized structure of $ImMe_2$•$Ge(OC_6F_5)_2$. Geometry determined at the M06-2X/cc-pVDZ level of theory.

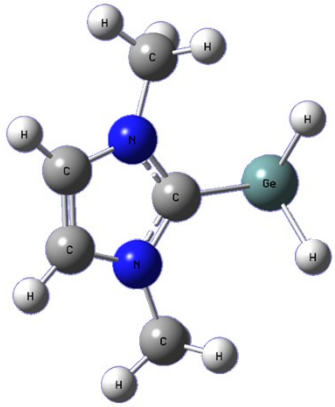

Fig. S74. Optimized structure of $ImMe_2$•GeH_2. Geometry determined at the M06-2X/cc-pVDZ level of theory.

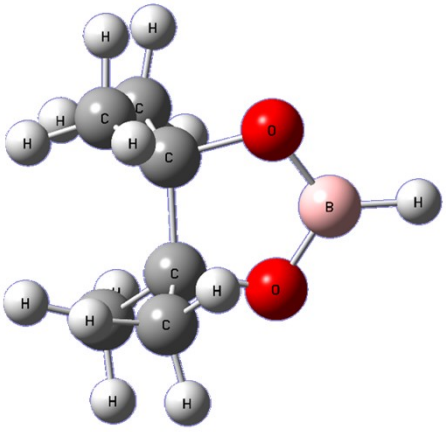

Fig. S75. Optimized structure of HBpin. Geometry determined at the M06-2X/cc-pVDZ level of theory.

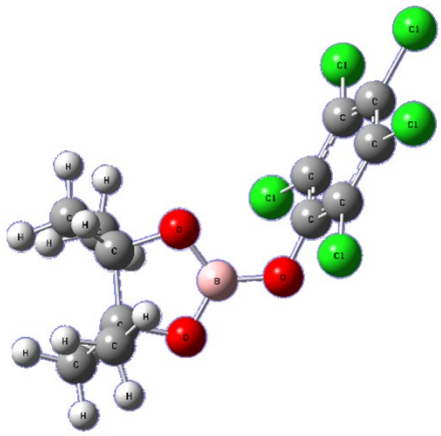

Fig. S76. Optimized structure of pinBO(C_6Cl_5). Geometry determined at the M06-2X/cc-pVDZ level of theory.

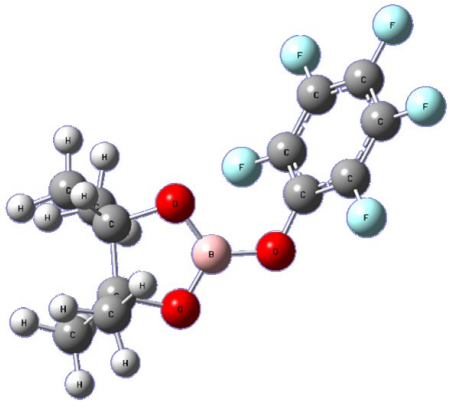

Fig. S77. Optimized structure of pinBO(C_6F_5). Geometry determined at the M06-2X/cc-pVDZ level of theory.

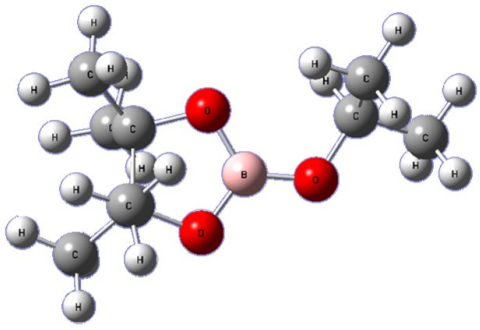

Fig. S78. Optimized structure of pinBO^{i}Pr. Geometry determined at the M06-2X/cc-pVDZ level of theory.

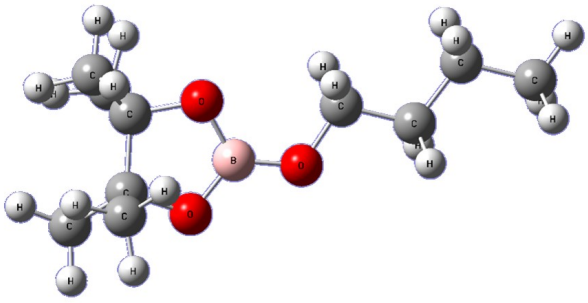

Fig. S79. Optimized structure of pinBOMe. Geometry determined at the M06-2X/cc-pVDZ level of theory.

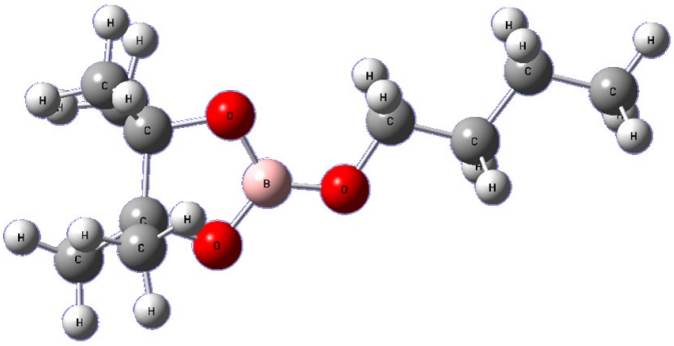

Fig. S80. Optimized structure of pinBO^{n}Bu. Geometry determined at the M06-2X/cc-pVDZ level of theory.

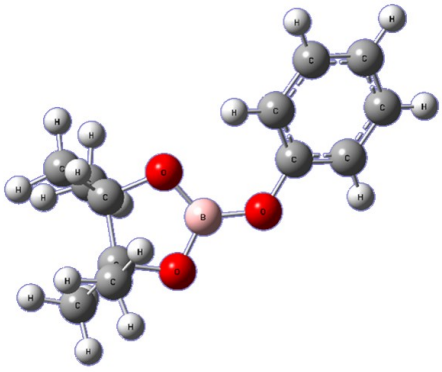

Fig. S81. Optimized structure of pinBOPh. Geometry determined at the M06-2X/cc-pVDZ level of theory.

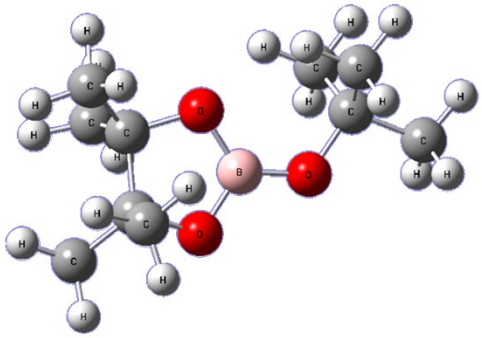

Fig. S82. Optimized structure of pinBO^{t}Bu. Geometry determined at the M06-2X/cc-pVDZ level of theory.

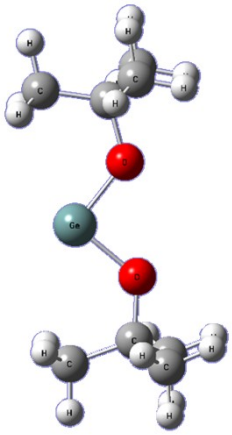

Fig. S83. Optimized structure of monomeric Ge(O^{t}Bu)$_2$. Geometry determined at the M06-2X/cc-pVDZ level of theory.

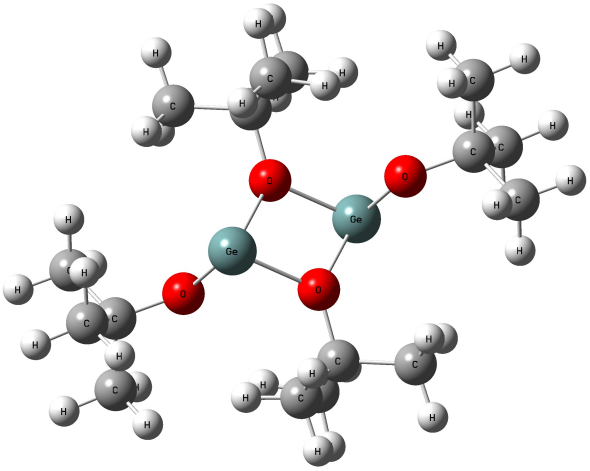

Fig. S84. Optimized structure of dimeric [Ge(O^{t}Bu)$_2$]$_2$. Geometry determined at the M06-2X/cc-pVDZ level of theory.

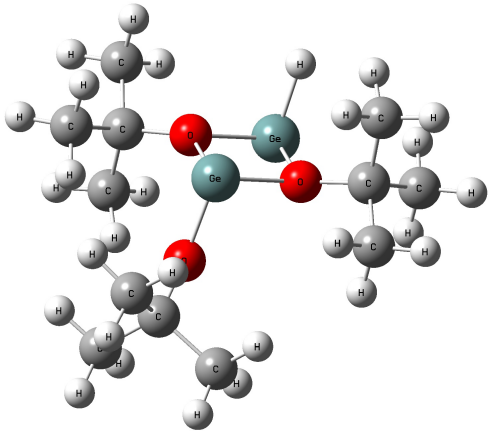

Fig. S85. Optimized structure of [(H)Ge(μ-O^{t}Bu)$_2$Ge(O^{t}Bu)] . Geometry determined at the M06-2X/cc-pVDZ level of theory.

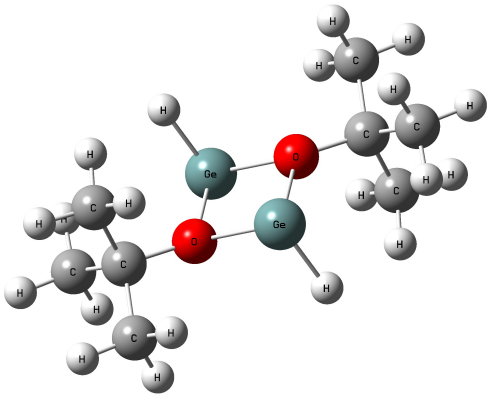

Fig. S86. Optimized structure of [(H)Ge(μ-O^{t}Bu)$_2$Ge(H)]. Geometry determined at the M06-2X/cc-pVDZ level of theory.

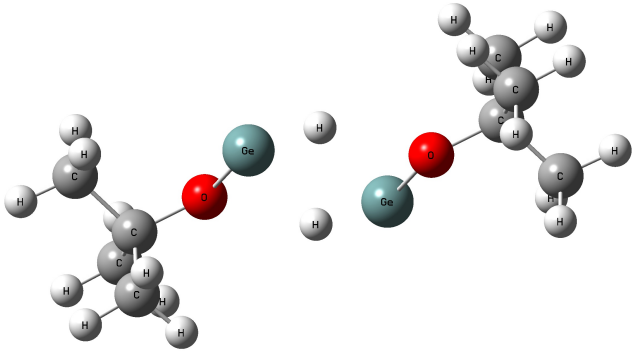

Fig. S87. Optimized structure of [(O^{t}Bu)Ge(μ-H)$_2$Ge(O^{t}Bu)]. Geometry determined at the M06-2X/cc-pVDZ level of theory. The free energy of the H-bridged dimer is 42 kJ mol^{-1} higher than the O^{t}Bu-bridged isomer (seen in Fig. S86).

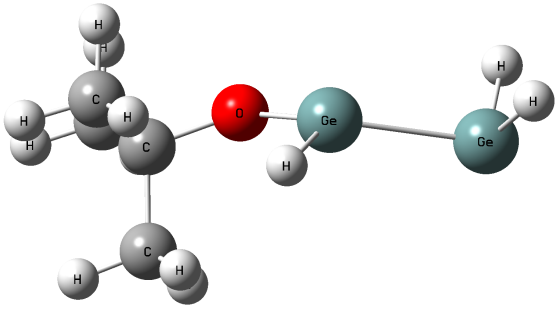

Fig. S88. Optimized structure of $H_2Ge{=}GeH(O^tBu)$. Geometry determined at the M06-2X/cc-pVDZ level of theory.

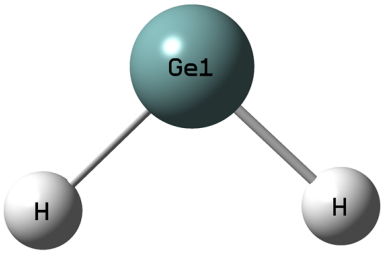

Fig. S89. Optimized structure for the computed geometry of GeH_2 (singlet). Geometry determined at the PBE0 /cc-pVTZ level of theory.

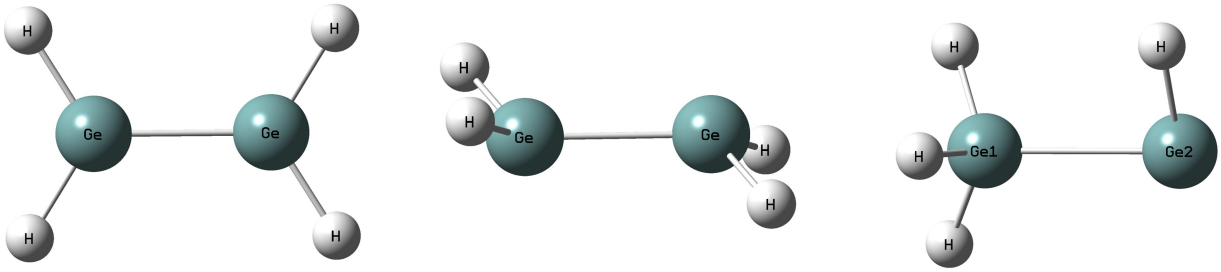

$[GeH_2]_2$ planar

$[GeH_2]_2$ bent

H_3Ge-GeH

Fig. S90. Optimized structures for the computed geometries for $[GeH_2]_2$ isomers. Geometries determined at the PBE0 /cc-pVTZ level of theory.

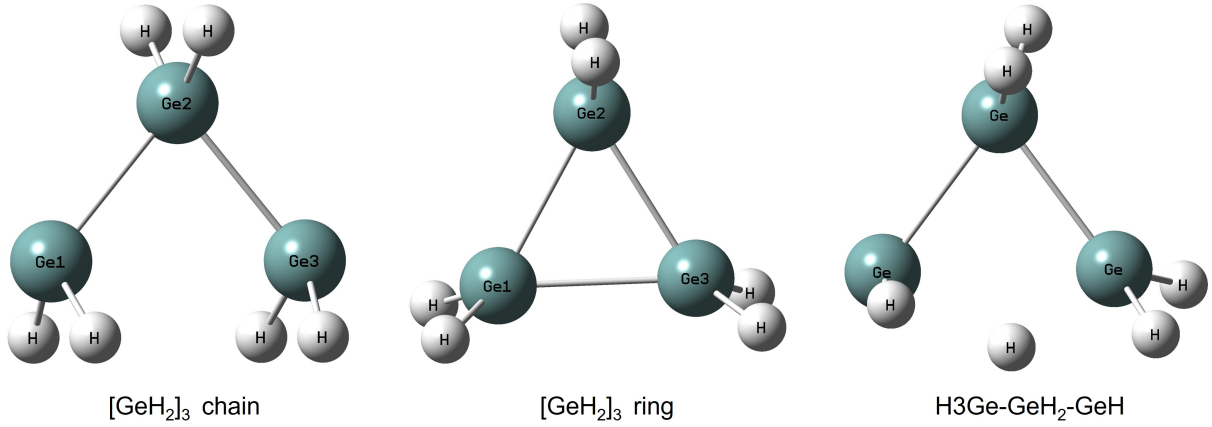

Fig. S91. Optimized structures for the computed geometries for $[GeH_2]_3$ isomers. Geometries determined at the PBE0 /cc-pVTZ level of theory.

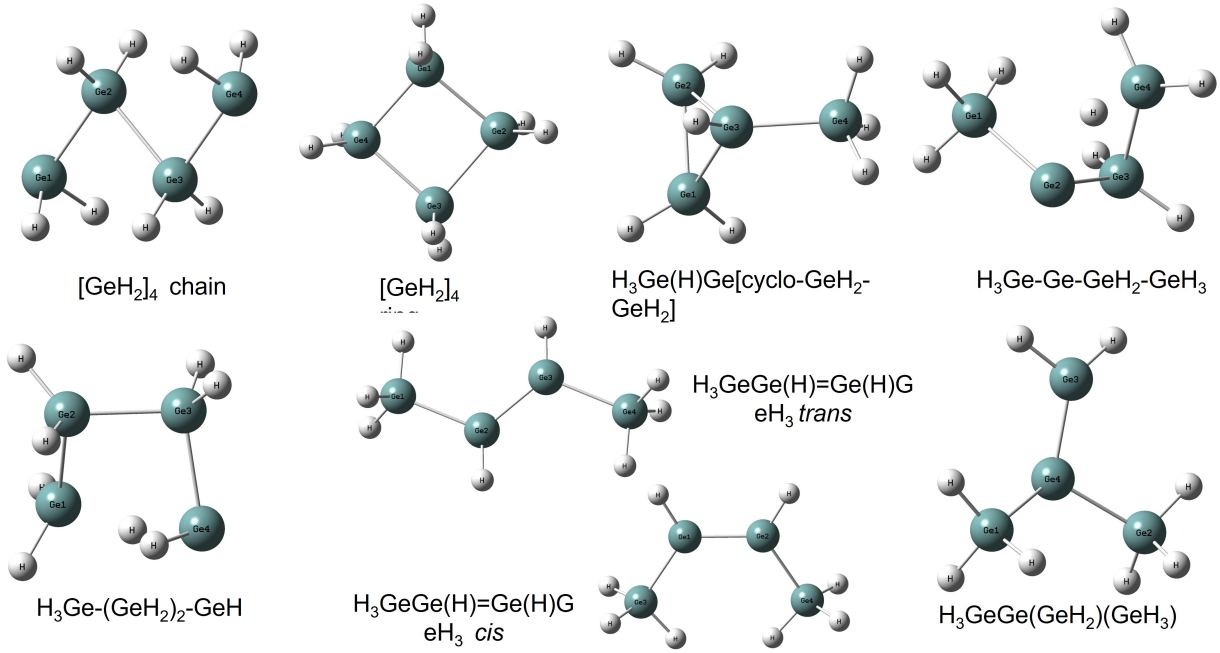

Fig. S92. Optimized structures for the computed geometries for $[GeH_2]_4$ isomers. Geometries determined at the PBE0 /cc-pVTZ level of theory.

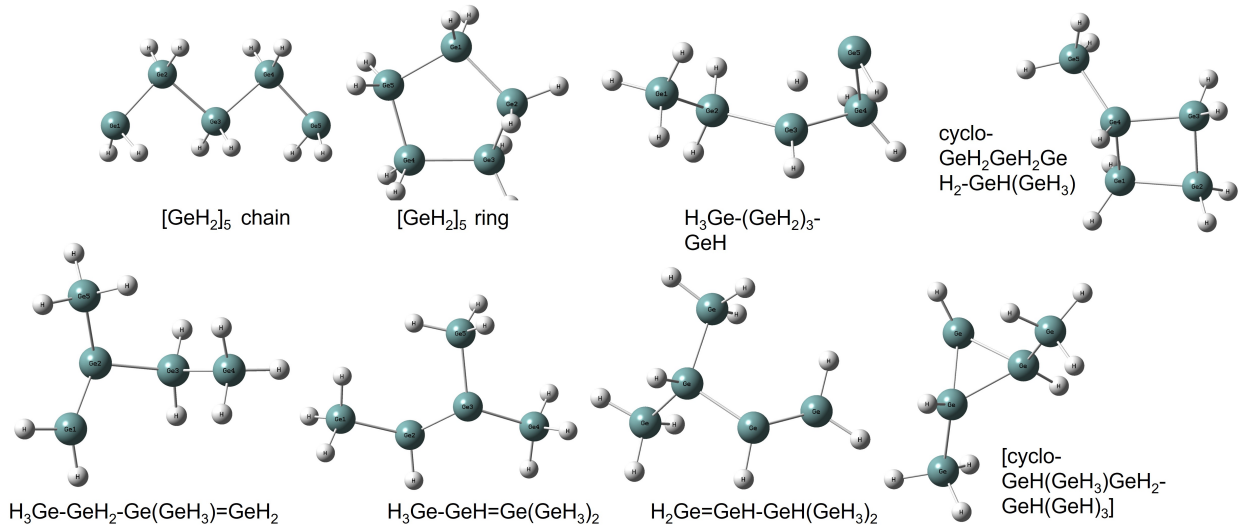

Fig. S93. Optimized structures for the computed geometries for $[GeH_2]_5$ isomers. Geometries determined at the PBE0 /cc-pVTZ level of theory.

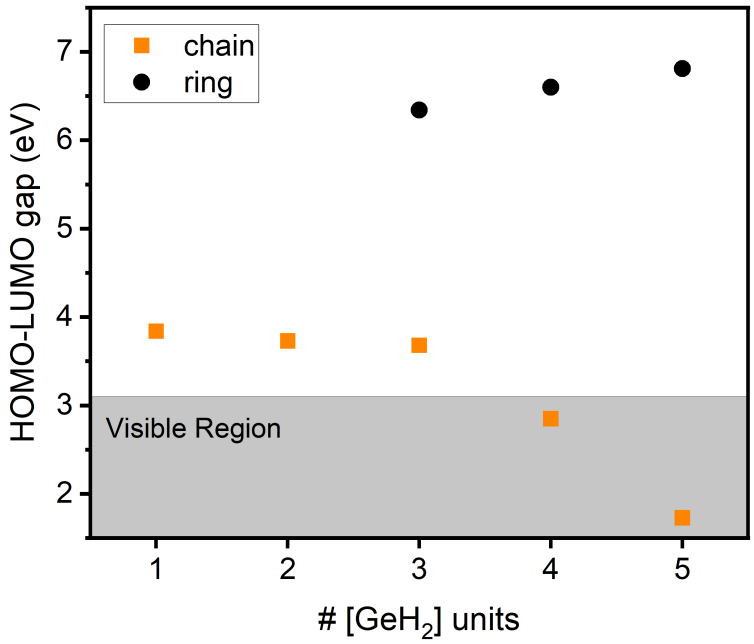

Fig. S94. Band gaps of the chain and ring conformers of $[GeH_2]_n$, where n = 1-5. Determined at the PBE0 /cc-pVTZ level of theory.

Table S4. Computed IR frequencies and assignments for the H-[GeH_2]$_{10}$-H and H-[Ge(H)(GeH_3)]$_5$-H oligomers. Unique frequencies (within 5 cm^{-1}) are highlighted in green. Determined at the PBE0 /cc-pVTZ level of theory.

Oligomer	IR Frequency (cm^{-1})	Molecular motion
H-[GeH_2]$_{10}$-H	2147-2143	terminal GeH_3 asym. stretch
	2132-2118	central GeH_2 asym. stretch
	2117-2112	central GeH_2 sym. stretch
	882, 881	terminal GeH_3 scissor
	862-858	central GeH_2 scissor
	791	terminal GeH_3 wag
H-[Ge(H)(GeH_3)]$_5$-H	2148-2133	terminal GeH_3 asym. stretch
	2132-2101	GeH_3 sym. stretch
	2094-2089	Ge-Ge(*H*)-Ge stretch
	874-883	terminal GeH_3 scissor
	801, 785-775	GeH_3 scissor
	692, 697	Ge-Ge(*H*)-Ge wag

Table S5. UV-Vis absorption transitions of the Ge_{10} oligomers, as computed by TD-DFT (B3LYP/cc-pVTZ, structures optimized at the PBE0 /cc-pVTZ level of theory)

Oligomer	#	Contribution	Weight of Contribution	Energy (eV)	Energy (nm)	Oscillator Strength
H-[GeH_2]$_{10}$-H	1	HOMO → LUMO	0.69967	4.6768	265.1	3.3421
H-[Ge(H)(GeH_3)]$_5$-H	1	HOMO → LUMO	0.66941	5.2801	234.81	0.4825
	2	HOMO-1 → LUMO	0.67578	5.3407	232.15	0.0946
	3	HOMO → LUMO+2	0.59827	5.5199	224.61	0.1215
		HOMO-1 → LUMO+2	0.26643			
	4	HOMO-1 → LUMO +2	0.51666	5.7229	216.65	0.1583
		HOMO → LUMO+4	0.2948			
		HOMO-2 → LUMO	0.25739			

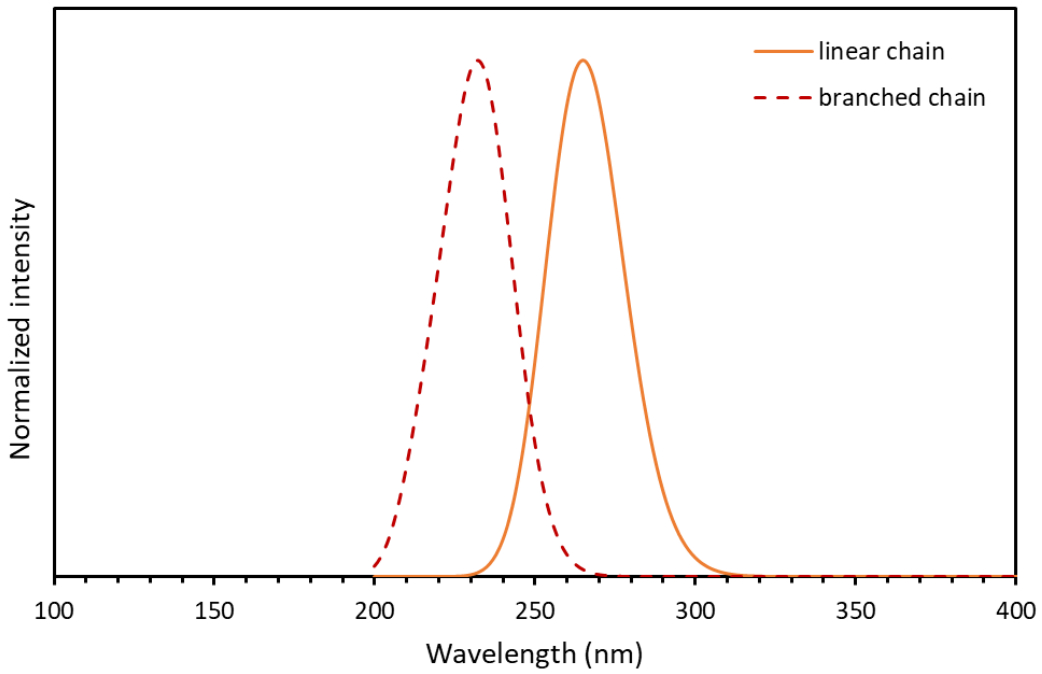

Fig. S95. Computed UV-Vis absorption spectra of the linear (H-[GeH_2]$_{10}$-H) and branched (H-[Ge(H)(GeH_3)]$_5$-H) oligomers. Plotted from the data in Table 5.[S24]

7. Catalysis Studies

Summary and discussion of results:
In a pioneering 2014 study,[S25] the Jones group showed that bulky low-coordinate Ge^{II} hydrides, such as L(H)Ge: (L = [N(C_6H_2{C(H)Ph_2}$_2$$Pr^i$-2,6,4)($SiPr^i_3$)]) could be used to promote the very rapid hydroboration of ketones and aldehydes.[S25] As a result, we were interested in seeing if the abovementioned Ge^{II} species [Ge(O^tBu)$_2$] (**1**), [$GeH_{1.92}$($OtBu$)$_{0.08}$]$_n$ (**2c**) and $ImMe_2$•Ge(O^tBu)$_2$ (**3**) could exhibit similar catalytic hydroboration chemistry (Scheme S1). To begin, a stoichiometric quantity of [Ge(O^tBu)$_2$] (**1**) was added to a solutions various alkene and alkyne substrates and HBpin (1:1:2 molar ratio) in C_6D_6 at room temperature; however, no reaction was found after 48 hrs of stirring. Fortunately, **1** was able to act as a hydroboration catalyst towards ketones and aldehydes, with the best result when 10 mol % of [Ge(O^tBu)$_2$] (**1**) was combined with 4-dimethylaminobenzaldehyde and HBpin (two equiv.) at 25 °C in C_6D_6, leading to a conversion of 75 % after 48 hrs (80 % after 20 hrs at 70 °C), relative to 4,4′-difluorobiphenyl as an ^{1}H NMR internal standard. For comparison, a related pre-catalyst [IPr•GeO^tBu]$^+$ (IPr = [(HCNDipp)$_2$C: ; Dipp = 2,6-^{i}Pr$_2$$C_6H_3$ achieved the quantitative hydroborylation of 4-dimethylaminobenzaldehyde under 6 hrs.[25d] Similar conversions (80 % borylation of 4-dimethylaminobenzaldehyde after 48 hrs at 25 °C) were found using 10 mol % $ImMe_2$•Ge(O^tBu)$_2$ (3) as a pre-catalyst. Notably, mixing the aldehyde with HBpin for 48 hrs at 25 °C in C_6D_6 only gave a trace amount (<3 %) of hydroboration product.To our surprise, the insoluble hydride [$GeH_{1.92}$(O^tBu)$_{0.08}$]$_n$ (**2c**) also catalyzed (at 10 mol % loadings) the hydroboration of 4-$Me_2NC_6H_4C(O)H$, with 22 % conversion noted after 48 hrs at 25 °C. This represents a rare example of a main group element-based heterogeneous catalysis (TON=2.2) under mild conditions.[S26]

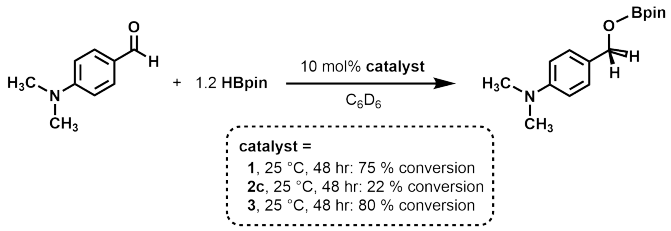

Scheme S1. Summary of borylation catalysis promoted by compounds **1**, **2c**, and **3**.

Stoichiometric hydroboration of carbonyl compounds:
In a nitrogen-filled glove box, a mixture of [Ge(O^tBu)$_2$] (**1**) (0.0219 g, 0.100 mmol) and the carbonyl substrate (0.100 mmol) in C_6D_6 (0.7 mL) was added HBpin (0.0256 g 0.200 mmol), and reacted at room temperature for 8 hrs. For screening reactions, the reaction mixture was monitored by ^{1}H NMR spectroscopy with yield calculated by relative integration to starting materials.

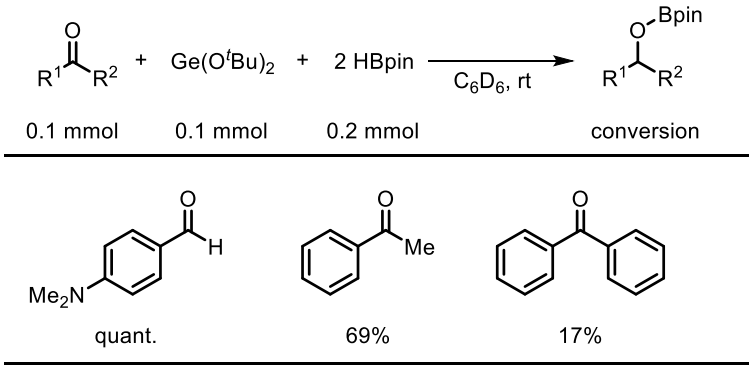

Scheme S2. Substrates and reaction conditions for the stoichiometric hydroboration of carbonyl compounds.

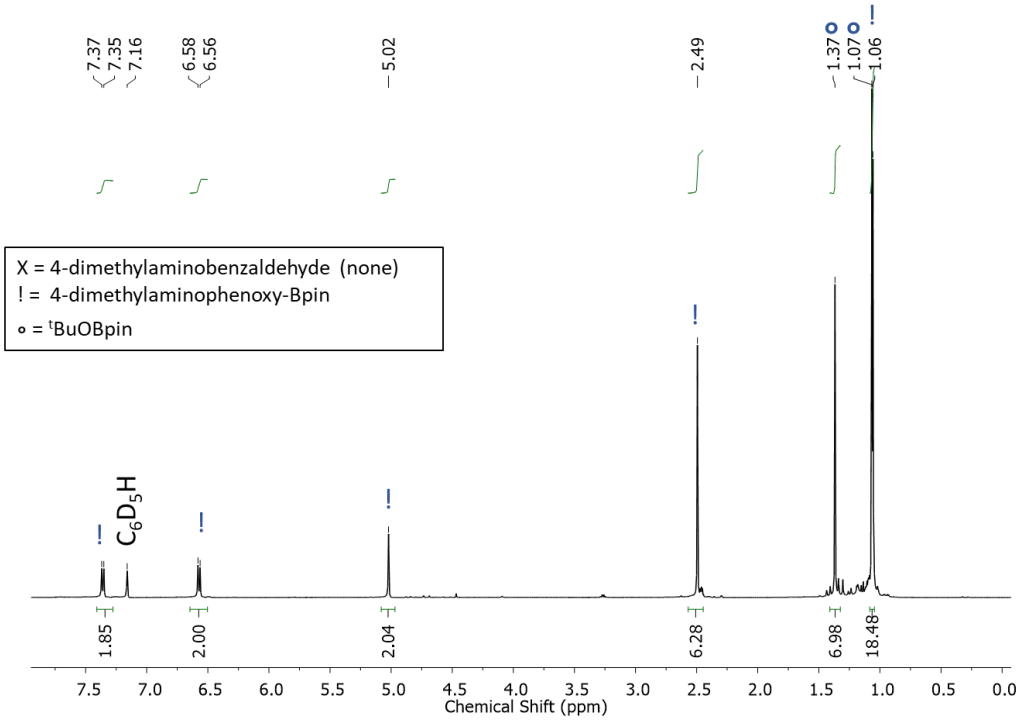

Fig. S96. ^{1}H NMR spectrum (C_6D_6) of the stoichiometric hydroboration of 4-dimethylaminobenzaldehyde as per Scheme 1 with [Ge(O^{t}Bu)$_2$] (**1**) (100 mol %) after 8 hrs. No starting material is observed, indicating quantitative conversion.[S27]

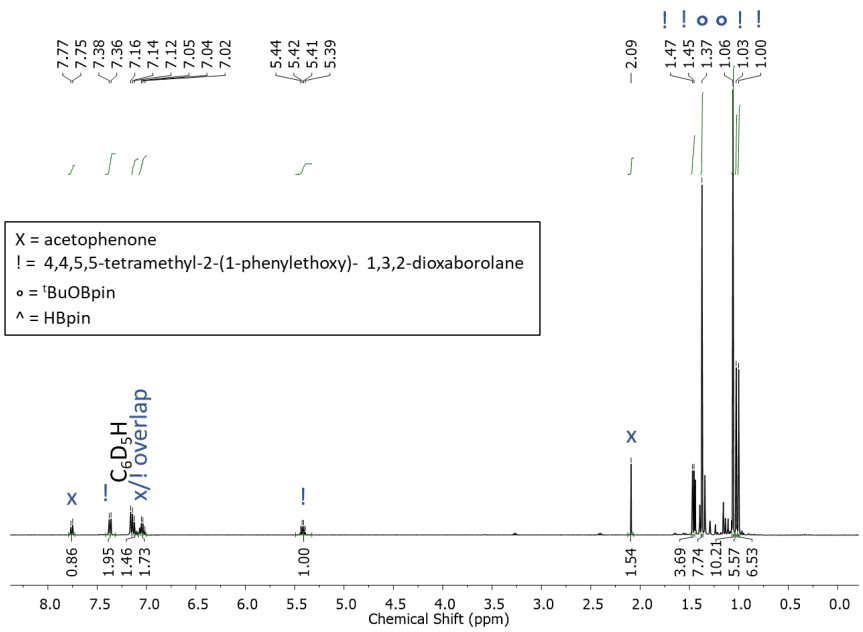

Fig. S97. ^{1}H NMR spectrum (C_6D_6) of the stoichiometric hydroboration of acetophenone as per Scheme 1 with [Ge(O^{t}Bu)$_2$] (**1**) (100 mol %) after 8 hrs. Relative integration in the aryl region (7.76 ppm vs. 7.37 ppm) indicates 69% conversion. [S27]

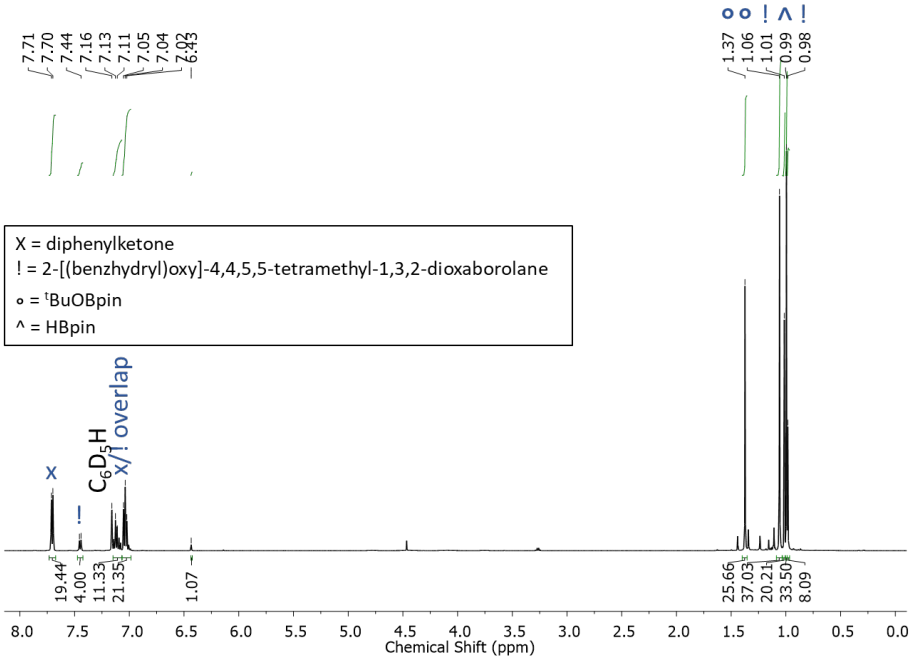

Fig. S98. ^{1}H NMR spectrum (C_6D_6) of the stoichiometric hydroboration of diphenylketone as per Scheme 1 with [Ge(O^{t}Bu)$_2$] (**1**) (100 mol %) after 8 hrs. Relative integration in the aryl region (7.70 ppm vs. 7.44 ppm) indicates 17% conversion. [S27]

The catalytic hydroboration of carbonyl compounds:

Uncatalyzed hydroboration of 4-dimethylaminobenzaldehyde: In a nitrogen-filled glove box, to a mixture of 4-dimethylaminobenzaldehyde (0.0121 g, 0.0811 mmol) in C_6D_6 (0.600 mL) was added HBpin (0.0125 g, 0.0973 mmol). The reaction mixture was monitored by ^{1}H NMR spectroscopy, with integration relative to an internal standard of 4,4′-difluorobiphenyl (2.0 mg, 0.011 mmol), and the formation of a corresponding hydroborylated product was observed in a 3 % yield after 48 hrs.

Catalytic hydroboration of 4-dimethylaminobenzaldehyde promoted by [Ge(O^{t}Bu)$_2$] (1): In a nitrogen-filled glove box, to a mixture of [Ge(O^{t}Bu)$_2$] (**1**) (0.0021 g, 0.010 mmol) and 4-dimethylaminobenzaldehyde (0.0149 g, 0.100 mmol) in C_6D_6 (0.600 mL) was added HBpin (0.0154 g, 0.120 mmol). The reaction mixture was monitored by ^{1}H NMR spectroscopy, with integration relative to an internal standard of 4,4′-difluorobiphenyl (2.9 mg, 0.015 mmol), and the formation of a corresponding hydroborylated product was observed in a 75 % yield after 48 hrs.

Catalytic hydroboration of 4-dimethylaminobenzaldehyde promoted by 2c: In a nitrogen-filled glove box, to a mixture of **2c** (0.7 mg, 0.01 mmol) and 4-dimethylaminobenzaldehyde (0.0157 g, 0.100 mmol) in C_6D_6 (0.600 mL) was added HBpin (0.0162 g, 0.126 mmol). 4,4′-Difluorobiphenyl was added as an internal standard (2.1 mg, 0.011 mmol) The reaction mixture was monitored by ^{1}H NMR spectroscopy, with integration relative to an internal standard of 4,4′-difluorobiphenyl (2.1 mg, 0.011 mmol), and formation of the corresponding organoboron hydroborylated product was observed in a 22 % yield after 48 hrs.

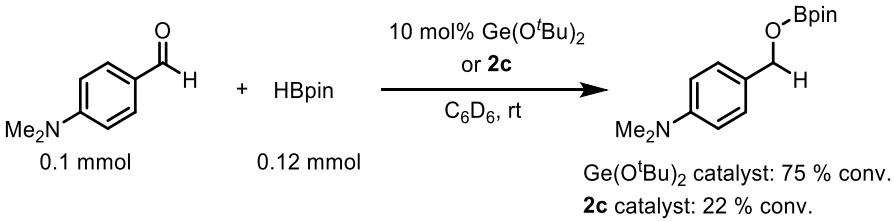

Scheme S3. The catalytic hydroboration of 4-dimethylaminobenzaldehyde with either [Ge(O^{t}Bu)$_2$] (**1**) or **2c** as pre-catalysts.

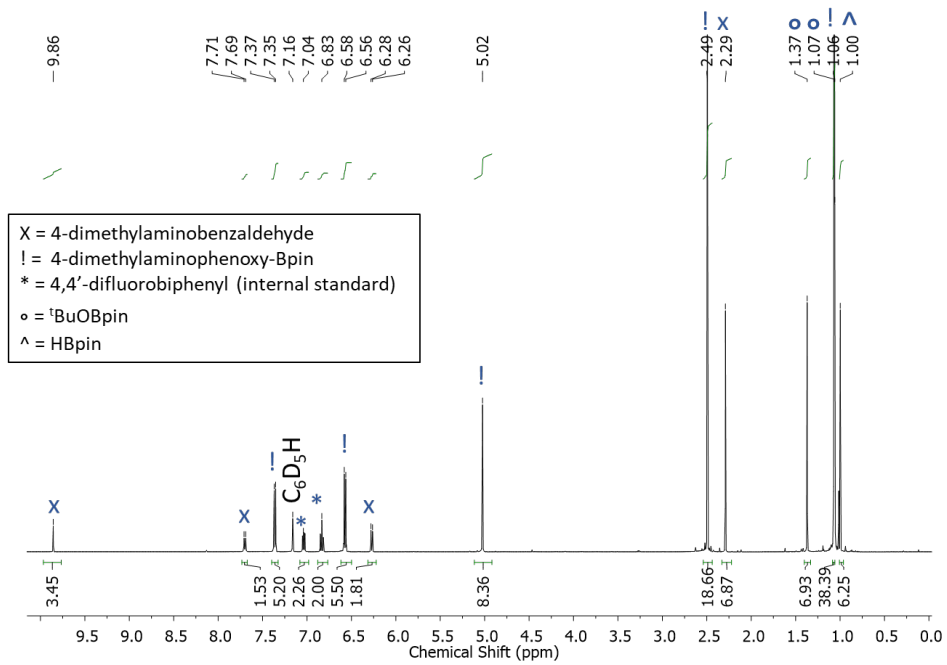

Fig. S99. ^{1}H NMR spectrum (C_6D_6) of the catalytic hydroboration of 4-dimethylaminobenzaldehyde as per Scheme 2 with [Ge(O^{t}Bu)$_2$] (**1**) (10 mol %) after 48 hrs. Integration in the aryl region *vs.* an internal standard shows 75% conversion. [S27]

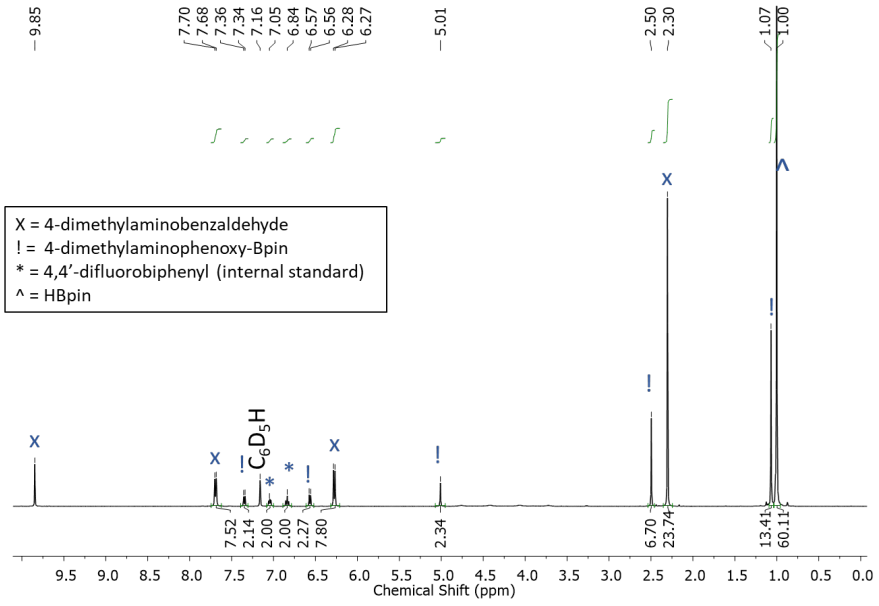

Fig. S100. ^{1}H NMR spectrum (in C_6D_6) of the catalytic hydroboration of 4-dimethylaminobenzaldehyde as per Scheme 2 with 10 mol % of **2c**, after 48 hrs. Integration in the aryl region vs. an internal standard shows 22 % conversion. [S27]

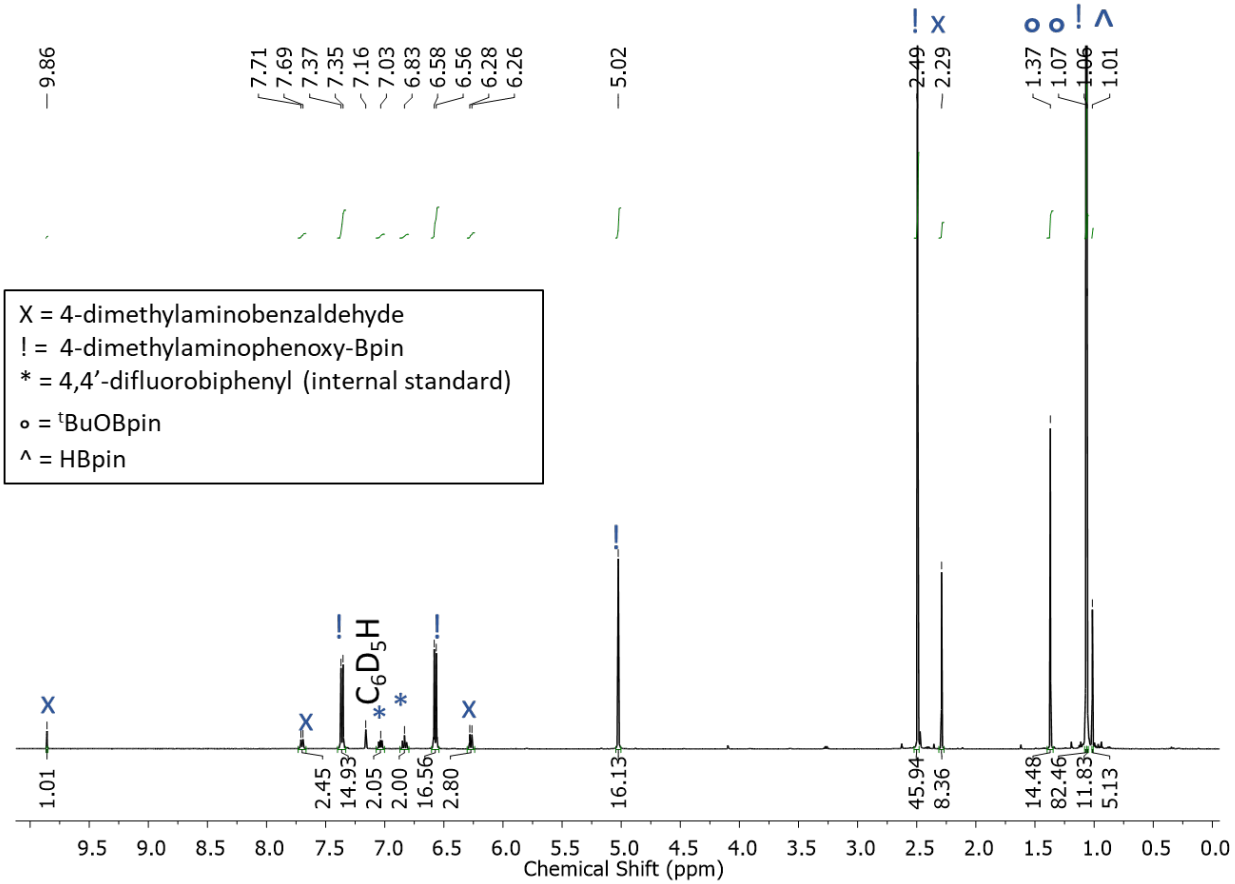

Fig. S101. ^{1}H NMR spectrum (in C_6D_6) of the catalytic hydroboration of 4-dimethylaminobenzaldehyde as per Scheme 2 with 10 mol % of **1**, after 20 hrs at 70 °C. Integration in the aryl region vs. an internal standard shows 86 % conversion.[S27]

Attempted stoichiometric hydroboration of alkynes:
In a nitrogen-filled glove box, to a mixture of [Ge(O^{t}Bu)$_2$] (**1**) (0.0219 g, 0.100 mmol) and alkyne (0.100 mmol) in C_6D_6 (0.7 mL) was added HBpin (0.0256 g 0.200 mmol). The reaction mixture was monitored by ^{1}H NMR spectroscopy, and the formation of a corresponding organoboron compound was NOT observed after 48 hrs.

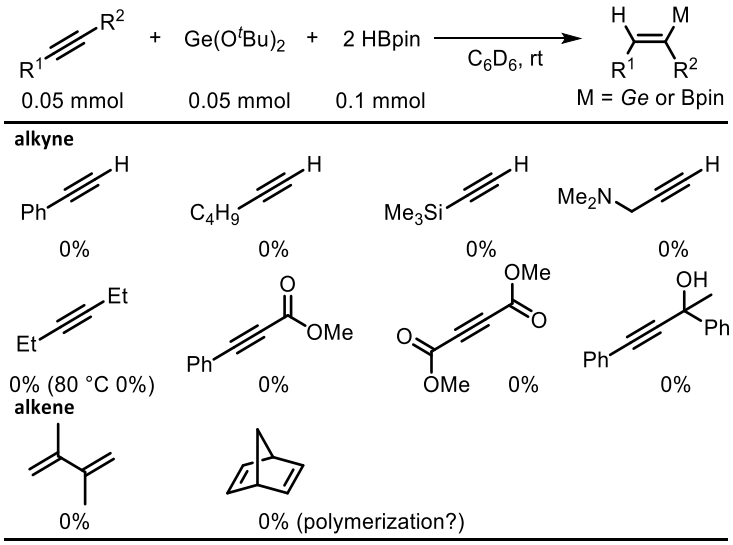

Scheme S4. Substrates and reaction conditions for the tested hydroboration of alkynes with [Ge(O^{t}Bu)$_2$] (**1**) as a pre-catalyst.

Attempted catalytic hydroboration of alkynes with ImMe$_2$•Ge(O^{t}Bu)$_2$ (3):
In a nitrogen-filled glove box, a of ImMe$_2$•Ge(O^{t}Bu)$_2$ (0.0016 g, 0.0051 mmol) and alkyne (0.0500 mmol) in C_6D_6 (0.70 mL) was added HBpin (0.0128 g 0.100 mmol). The reaction mixture was monitored by ^{1}H NMR spectroscopy, and the formation of a corresponding organoboron compound was NOT observed after 48 hrs at room temperature.

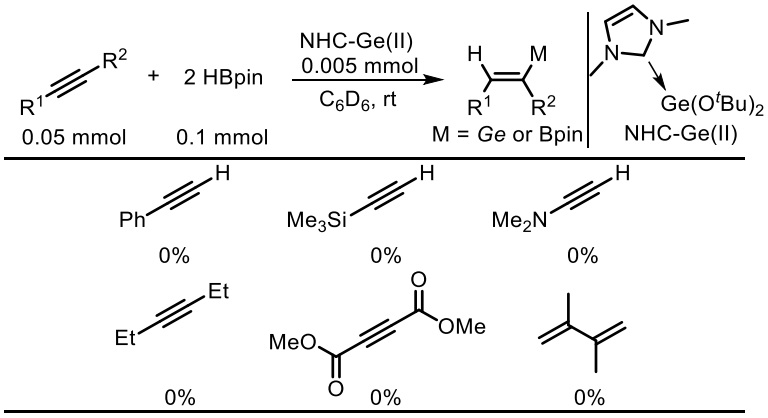

Scheme S5. Attempted hydroboration of alkynes with ImMe$_2$•Ge(O^{t}Bu)$_2$ (**3**) as a pre-catalyst.

References

(S1) J. Sinclair, G. Dai, R. McDonald, M. J. Ferguson, A. Brown and E. Rivard, *Inorg. Chem.*, 2020, **59**, 10996.

(S2) A. Meller and C.-P. Gräbe, *Chem. Ber.*, 1985, **118**, 2020.

(S3) A. A. Omaña, R. K. Green, R. Kobayashi, Y. He, E. R. Antoniuk, M. J. Ferguson, Y. Zhou, J. G. C. Veinot, T. Iwamoto, A. Brown and E. Rivard, *Angew. Chem. Int. Ed.*, 2021, **60**, 228.

(S4) (*a*) Sheldrick, G. M. *Acta Cryst.*, 2015, **A71**, 3-8; (*b*) Sheldrick, G. M. *Acta Cryst.*, 2015, **C71**, 3.

(S5) M. D. Pelta, G. A. Morris, M. J. Stchedroff and S. J. Hammond, *Magn. Reson. Chem.*, 2002, **40**, S147.

(S6) A. Botana, J. A. Aguilar, M. Nilsson, G. A. Morris, *J. Magn. Reson.*, 2011, **208**, 270.

(S7) M. A. Connell, P. J. Bowyer, P. A. Bone, A. L. Davis, A. G. Swanson, M. Nilsson and G. A. Morris, *J. Magn. Reson.*, 2009, **198**, 121.

(S8) (*a*) S. Matsuo and T. Makita, *Int. J. Thermophys.* 1993, **14**, 67; (*b*) P. Groves, *Polym. Chem.*, 2017, **8**, 6700.

(S9) A. Laubengayer and P. Brandt, *J. Am. Chem. Soc.*, 1932, **54**, 621.

(S10) T. Lui, J. He and Y. Zhang, *Org. Chem. Front.*, 2019, **6**, 2749.

(S11) W. Drescher and C. Kleeberg, *Inorg. Chem*., 2019, **58**, 8215.

(S12) I. P. Query, P. A. Squier, E. M. Larson, N. A. Isley and T. B. Clark *J. Org. Chem.,* 2011, **76**, 6452.

(S13) (*a*) S. Foster, K. Leung, K. Mackay and R. Thompson, *Aust. J. Chem.*, 1986, **39**, 1089; (*b*) J. Jensen, *J. Mol. Struct.*, 2005, **714**, 21; (*c*) H. Yildirimyan and G. Gattow, *Z. Anorg. Allg. Chem.*, 1985, **521**, 135.

(S14) H. Yu, C. Ni, A. N. Thiessen, A. Li and J. G. C. Veinot, *ACS Nano*, 2021, **15**, 9368.

(S15) R. Heinemann and P. Schmidt, *Cryst. Growth Des.*, 2020, **20**, 5986.

(S16) P. Makula, M. Pacia and W. Macyk, *J. Phys. Chem. Lett.*, 2018, **9**, 6814.

(S17) M. J. Frisch, G. W. Trucks, H. B. Schlegel, G. E. Scuseria, M. A. Robb, J. R. Cheeseman, G. Scalmani, V. Barone, G. A. Petersson, H. Nakatsuji, X. Li, M. Caricato, A. V. Marenich, J. Bloino, B. G. Janesko, R. Gomperts, B. Mennucci, H. P. Hratchian, J.V. Ortiz, A. F. Izmaylov, J. L. Sonnenberg, D. Williams-Young, F. Ding, F. Lipparini, F. Egidi, J. Goings, B. Peng, A. Petrone, T. Henderson, D. Ranasinghe, V. G. Zakrzewski, J. Gao, N. Rega, G. Zheng, W. Liang, M. Hada, M. Ehara, K. Toyota, R. Fukuda, J. Hasegawa, M. Ishida, T. Nakajima, Y. Honda, O. Kitao, H. Nakai, T. Vreven, K. Throssell, J. A. J. Montgomery, J. E. Peralta, F. Ogliaro, M. J. Bearpark,

J. J. Heyd, E. N. Brothers, K. N. Kudin, V. N. Staroverov, T. A. Keith, R. Kobayashi, J. Normand, K. Raghavachari, A. P. Rendell, J. C. Burant, S. S. Iyengar, J. Tomasi, M. Cossi, J. M. Millam, M. Klene, C. Adamo, R. Cammi, J. W. Ochterski, R. L.Martin, K. Morokuma, O. Farkas, J. B. Foresman and D. J. Fox, Gaussian 16, Revision B.01, Gaussian, Inc., Wallingford CT.

(S18) Y. Zhao and D. Truhlar, *Theor. Chem. Acc.*, 2008, **120**, 215.

(S19) (*a*) T. H. Dunning Jr., *J. Chem. Phys.* 1989, **90**, 1007; (*b*) A. K. Wilson, D. E. Woon, K. A. Peterson and T. H. Dunning Jr., *J. Chem. Phys.,* 1999, **110**, 7667.

(S20) (*a*) S. Harrypersad, L. Liao, A. Khan, R. S. Wylie and D. A. Foucher, *J. Inorg. Organomet. Polym*., 2015, **25**, 515; (*b*) W. Fa, X. C. Zeng, *Chem. Commun.*, 2014, **50**, 9126.

(S21) J. P. Perdew, K. Burke and M. Ernzerhof, *Phys. Rev. Lett.*, 1996, **77**, 3865.

(S22) E. R. Johnson and A. D. Becke, A. D. *J. Chem. Phys.,* 2006, **124**, 174104.

(S23) (*a*) A. D. Becke, *J. Chem. Phys.*, 1993, **98**, 5648; (*b*) C. Lee, W. Yang and R. G. Parr, *Phys. Rev. B*, 1988, **37**, 785; (*c*) S. H. Vosko, L. Wilk and M. Nusair, *Can. J. Phys.*, 1980, **58**, 1200; (*d*) P. J. Stephens, F. J. Devlin, C. F. Chabalowski and M. J. Frisch, *J. Phys. Chem.*, 1994, **98**, 11623.

(S24) A line broadening (σ) of 0.000241967 nm^{-1} was applied, according to the method presented on: Creating UV/Visible Plots from the Results of Excited States Calculations. http://gaussian.com/uvvisplot/ [Accessed June 25, 2021].

(S25) (a) T. J. Hadlington, M. Driess and C. Jones, *Chem. Soc. Rev.*, 2018, **47**, 4176; (b) M. M. D. Roy, S. Fujimori, M. J. Ferguson, R. McDonald, N. Tokitoh and E. Rivard, *Chem. Eur. J.*, 2018, 24, 14392; (c) R. Jambor and A. Lycka, Eur. *J. Inorg. Chem.*, 2017, 4887; (d) T. J. Hadlington, C. E. Kefalidis, L. Maron and C. Jones, *ACS Catal.*, 2017, **7**, 1853.

(S26) As is the case with many heterogenous catalysts, it is difficult to entirely rule out participation from by small amounts of soluble species released during catalysis.

(S27) Characteristic ^{1}H NMR of products can be found in: S. Anga, J. Acharya and V. Chandrasekhar, *J. Org. Chem.*, 2021, **86**, 2224.